DEVELOPMENT OF AN EFFICIENT DESIGN METHOD FOR NON-SYNCHRONOUS VIBRATIONS

by

Meredith Anne Spiker

Department of Mechanical Engineering and Materials Science
Duke University

Date: _____

Approved:

_____
Robert E. Kielb, Ph.D., Supervisor

_____
Kenneth C. Hall, Ph.D.

_____
Earl H. Dowell, Ph.D.

_____
Donald B. Bliss, Ph.D.

_____
Anita T. Layton, Ph.D.

Dissertation submitted in partial fulfillment of the
requirements for the degree of Doctor of Philosophy
in the Department of Mechanical Engineering and Materials Science
in the Graduate School of
Duke University

2008

ABSTRACT

DEVELOPMENT OF AN EFFICIENT DESIGN METHOD FOR NON-SYNCHRONOUS VIBRATIONS

by

Meredith Anne Spiker

Department of Mechanical Engineering and Materials Science
Duke University

Date: _____

Approved:

_____
Robert E. Kielb, Ph.D., Supervisor

_____
Kenneth C. Hall, Ph.D.

_____
Earl H. Dowell, Ph.D.

_____
Donald B. Bliss, Ph.D.

_____
Anita T. Layton, Ph.D.

An abstract of a dissertation submitted in partial
fulfillment of the requirements for the degree
of Doctor of Philosophy in the Department of
Mechanical Engineering and Materials Science in the Graduate School of
Duke University

2008

Abstract

This research presents a detailed study of non-synchronous vibration (NSV) and the development of an efficient design method for NSV. NSV occurs as a result of the complex interaction of an aerodynamic instability with blade vibrations. Two NSV design methods are considered and applied to three test cases: 2-D circular cylinder, 2-D airfoil cascade tip section of a modern compressor, and 3-D high pressure compressor cascade that encountered NSV in rig testing. The current industry analysis method is to search directly for the frequency of the instability using CFD analysis and then compare it with a fundamental blade mode frequency computed from a structural analysis code. The main disadvantage of this method is that the blades' motion is not considered and therefore, the maximum response is assumed to be when the blade natural frequency and fluid frequency are coincident. An alternate approach, the enforced motion method, is also presented. In this case, enforced blade motion is used to promote lock-in of the blade frequency to the fluid natural frequency at a specified critical amplitude for a range of interblade phase angles (IBPAs). For the IBPAs that are locked-on, the unsteady modal forces are determined. This mode is acceptable if the equivalent damping is greater than zero for all IBPAs. A method for blade re-design is also proposed to determine the maximum blade response by finding the limit cycle oscillation (LCO) amplitude. It is assumed that outside of the lock-in region is an off-resonant, low amplitude condition. A significant result of this research is that for all cases studied herein, the maximum blade response is not at the natural fluid frequency as is assumed by the direct frequency search approach. This has significant implications for NSV design analysis because it demonstrates the requirement to include blade motion. Hence, an enforced motion design method is recommended for industry and the current approach is of little value.

Contents

List of Tables

List of Figures

Nomenclature

Symbols

a_{ref}	:	Freestream total acoustic velocity defined as $a_{ref} = \sqrt{\gamma R_{gas} T_{ref}}$
A_0	:	Mean Fourier coefficient
A_n	:	Fourier cosine coefficients of flow variables
B_n	:	Fourier sine coefficients of flow variables
c	:	Airfoil chord
c_v	:	Specific heat at constant volume
c_p	:	Specific heat at constant pressure
C_L	:	Unsteady lift coefficient
C_{D_0}	:	Mean drag coefficient
d	:	Damping coefficient
dA	:	Elemental control surface
dV	:	Elemental control volume
D	:	(1) Pseudospectral operator
	:	(2) Diameter of cylinder
e	:	Total internal energy
E	:	Discrete Fourier transform operator
E^{-1}	:	Inverse discrete Fourier transform operator
F	:	Flux Vector in the x direction
f	:	(1) X component of the displacement of the control volume

	:	(2) Dimensional frequency
f_N	:	Natural vortex shedding frequency
g	:	Y component of the displacement of the control volume
G	:	Flux vector in the y direction
h	:	(1) Z component of the displacement of the control volume
	:	(2) Cylinder plunge coordinate
h_1'	:	Non-dimensional cylinder plunge coordinate
h_e	:	Total enthalpy
H	:	Flux vector in the z direction
k	:	Cylinder spring stiffness
L	:	Vector of unknowns, Re and St
L_{ref}	:	User-defined constant length scale
M	:	Mach number
m	:	Mass of the cylinder
N_H	:	Number of harmonics
N	:	(1) Iteration number
	:	(2) Nonlinear matrix operating on the flow solution
Pr_L	:	Laminar Prandtl number
p	:	Static pressure
p_{ref}	:	User-defined total pressure
p'	:	Non-dimensional static pressure
p_{exit}	:	Exit pressure
$p_{exit_{CAFD}}$	:	Exit pressure for which NSV encountered in experiment
Q	:	(1) Modal force
	:	(2) HB flow solution vector

q_x	:	Heat flux component in x direction
q_y	:	Heat flux component in y direction
q_z	:	Heat flux component in z direction
R	:	Radial distance from x-axis
$R(L)$	:	Nominal residual
Re	:	Reynolds number
R_{gas}	:	Universal gas constant
S	:	Source vector
s	:	Cylinder span
St	:	Strouhal number
St_N	:	Natural shedding Strouhal number
T	:	Temperature
T_{ref}	:	User-defined total temperature
T'	:	Non-dimensional temperature
U	:	Vector of conservation variables
$\tilde{U}$	:	Vector of Fourier coefficients for each conservation variable
U^*	:	Vector of conservation variables evaluated at $2N_H + 1$ points
U_∞	:	Freestream velocity of fluid
u	:	Velocity component in the x direction
u'	:	Non-dimensional velocity component in the x direction
v	:	Velocity component in the y direction
V_{ref}	:	Reference velocity defined as $V_{ref} = a_{ref}/\sqrt{\gamma}$
v'	:	Non-dimensional velocity component in the y direction
w	:	Velocity component in the z direction
w'	:	Non-dimensional velocity component in the z direction

x'	:	Non-dimensional coordinate in the x direction
y'	:	Non-dimensional coordinate in the y direction
z'	:	Non-dimensional coordinate in the z direction
α	:	Angle of attack
β	:	Enforced pitch amplitude about elastic axis
ϵ	:	Small perturbation value
γ	:	Heat capacity ratio, $\gamma = c_p/c_v$
κ	:	Ratio of fluid frequency to structural frequency
μ	:	Dynamic molecular viscosity
μ_{ref}	:	Reference viscosity defined as $\mu_{ref} = \rho_{ref} V_{ref} L_{ref}$
μ'	:	Non-dimensional dynamic viscosity
μ_m	:	Mass ratio
ν	:	Kinematic viscosity of the fluid
Ω	:	Rotational frequency
Ω_{ref}	:	Reference rotational frequency defined as $\Omega_{ref} = V_{ref}/L_{ref}$
Ω'	:	Non-dimensional rotational frequency
ω	:	Frequency of flow unsteadiness
ω_n	:	Natural fluid frequency
ω_0	:	Natural frequency of structure
ρ	:	Density of fluid
ρ_{ref}	:	Total density defined as $\rho_{ref} = p_{ref}/(R_{gas} T_{ref})$
ρ'	:	Non-dimensional fluid density
τ	:	(1) Pseudo-time variable
	:	(2) Blade torque
τ_{xx}	:	Shear stress in the xx direction

τ_{xy}	:	Shear stress in the xy direction
τ_{xz}	:	Shear stress in the xz direction
τ_{yy}	:	Shear stress in the yy direction
τ_{yz}	:	Shear stress in the yz direction
τ_{zz}	:	Shear stress in the zz direction
τ_{hx}	:	Shear stress related to enthalpy in the x direction
τ_{hy}	:	Shear stress related to enthalpy in the y direction
τ_{hz}	:	Shear stress related to enthalpy in the z direction
θ	:	Inlet flow angle
ξ	:	Modal amplitude
ζ	:	Damping coefficient

Acronyms

CFD	:	Computational Fluid Dynamics
FEA	:	Finite Element Analysis
FR	:	Forced Response
HB	:	Harmonic Balance
HCF	:	High Cycle Fatigue
HPC	:	High Pressure Compressor
IGV	:	Inlet Guide Vane
IBPA	:	Interblade Phase Angle
LCO	:	Limit Cycle Oscillation
LB	:	Left Bound
ND	:	Nodal Diameter
NSV	:	Non-Synchronous Vibration

PR	:	Pressure Ratio
RB	:	Right Bound
RPM	:	Rotations Per Minute
SFV	:	Separated Flow Vibration

Superscripts

$\tilde{}$	:	Fourier transformed variable
*	:	Time domain variable

Acknowledgements

The research presented here is the culmination of my academic endeavors at Duke University. However, many other people contributed to this research effort and I am grateful for their extensive assistance and guidance. In particular, I would like to thank my advisor Dr. Robert Kielb for providing me with the opportunity to work on this project and introducing me to the field of turbomachinery. In addition, throughout my tenure at Duke, he provided me with continued guidance, constructive advice, and financial support through the Air Force Office of Scientific Research (AFOSR) and the GUIDE Consortium for which I am genuinely appreciative. I would also like to thank Dr. Steven Manwaring for giving me the opportunity to work at GE Aviation in Cincinnati, OH for a summer and gain valuable industry experience.

In addition, I would like to thank the other members of my committee: Dr. Kenneth Hall, Dr. Earl Dowell, Dr. Donald Bliss, and Dr. Anita Layton for serving on my committee and providing valuable input and recommendations for the advancement of my research. I also am grateful for the help and guidance of other members of Duke's Turbomachinery Aeroelasticity team: Dr. Jeffrey Thomas, Dr. Kivanc Ekici, and Tomokazu Miyakozawa.

Finally, I would like to thank my family and friends for their encouragement and support throughout my academic career. My parents have always been an inspiration and shown faith and confidence in my abilities. I also want to thank the good friends that I have made along the way for their support and memorable experiences. A heartfelt thanks also goes to Dr. Kurt Wulff for his love, patience, and understanding throughout the doctorate process. His continued support, encouragement, and companionship has turned my time in graduate school into a true pleasure.

Chapter 1

Introduction

This research presents a detailed study of non-synchronous vibration (NSV) and the development of an efficient design method for NSV. NSV occurs as a result of the complex interaction of an aerodynamic instability with blade vibrations. Typical features of aerodynamic instabilities encountered in turbomachinery are dynamic separation, tip flow instability and vortices, vortex shedding, acoustic instabilities, and other secondary flows. NSV has been most commonly seen in the front stages of high pressure compressor (HPC) and fan blades, vanes, and blisks. It is a serious aeroelastic problem that has been observed by most engine companies and the unsteady loading can reach levels high enough to cause blade high cycle fatigue (HCF) failures. Furthermore, there is limited knowledge of the underlying mechanisms of NSV so failures typically do not occur until the testing phase, which often requires redesign of the blade or the rotor. This procedure is costly and greatly increases engine development time.

Consequently, the predominant goal of this research effort is to establish a pragmatic preliminary design tool for NSV for routine use by industry. To accomplish this task, this research incorporates the following novel techniques:

- Use of nonlinear frequency domain harmonic balance (HB) method developed by Hall et al. [5] which requires 1 - 2 magnitudes less computational time than traditional time-marching computational fluid dynamics (CFD) methods
- Use of phase error method to efficiently determine frequency of instability [2]
- Application of the "lock-in" phenomenon to turbomachinery by using blade

motion to attempt to force the frequency of the aerodynamic instability to lock-on to a blade mode natural frequency at a specified critical amplitude

- Simplicity of implementation of proposed method into traditional design practice - flutter analysis, except conducted at a finite, critical amplitude

However, it is important to note here that the main objective of the research has not been to improve the CFD method itself. Rather, the research efforts have concentrated on using existing CFD techniques to develop a design method for NSV.

1.1 Research Motivation

Currently, the two main aeroelastic design considerations for turbomachinery blading are forced response and flutter. Forced response (FR) of rotor blades is a response whereby the aerodynamic excitations from upstream wakes occur at integer multiples of the vane passing frequency. The excitation frequencies are therefore said to be synchronous with the rotor speed. When the excitation frequencies are coincident with one of the blade natural frequencies, a resonant response occurs. Conversely, flutter is a self-excited aeroelastic instability in which the unsteady aerodynamic forces on the blade are caused by the blade motion itself and typically, occur at low reduced frequencies. Flutter is generally a non-synchronous phenomenon. Both of these aeroelastic phenomena have been well-studied and efficient industry design methods are established. In addition, the design analysis only requires the use of linear CFD techniques.

For forced response problems, the Campbell diagram is the primary design tool to avoid resonant responses. The Campbell diagram is a plot of the blade's natural frequencies of vibration in Hz as a function of the rotational speed of the engine in RPM. The diagonal lines of constant slope represent engine order excitations lines,

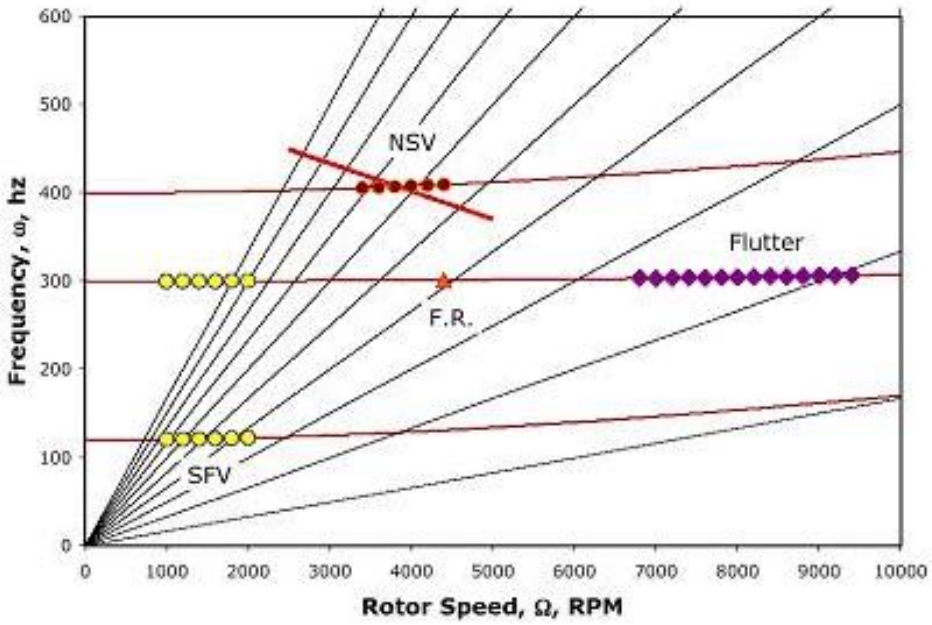

Figure 1.1: Hypothetical Campbell diagram including all aeroelastic blade design considerations [1].

i.e. multiples of the operation speed or machine harmonics. The nearly horizontal lines represent natural frequencies of particular blade modes, i.e. first flex (1F) or first torsion (1T). First, finite element analysis (FEA) is conducted and the blade mode shapes and natural frequencies are determined as a function of rotational speed. Resonant responses occur when there is a crossing between the synchronous excitations (such as vane passings) and the blade natural frequencies as shown in Figure 1.1. It is therefore advantageous to avoid these potential crossings.

To study flutter, CFD analysis is conducted to determine the aerodynamic damping (or stability) of the rotor for all interblade phase angles (IBPAs). Typically, we assume that all the blades vibrate at an identical frequency except for a phase lag, or interblade phase angle. A design is deemed acceptable if the rotor is stable for all IBPAs. If any IBPA is unstable, there are five dominant flutter design parameters that can be changed (depending on type of flutter) to achieve stability. The five parame-

ters are: reduced velocity, Mach number, incidence angle, static pressure/density, or vibratory mode shape [6]. Flutter could also be added to the Campbell diagram as shown in Figure 1.1.

However, in recent years, engine manufacturers have encountered a new class of aeromechanical problems. This category generally includes separated flow vibration (SFV) and non-synchronous vibration (NSV). Separated flow vibrations are similar to buffeting in wings and occur when an unsteady, separated flow is generated over a row of turbomachinery blades that randomly excites blade vibration. In addition, SFV generally has a broadband flow frequency content. Although separated flow vibration is an emerging research area, this effort has focused on the study and prevention of non-synchronous vibrations. Non-synchronous vibrations are similar to separated flow vibrations except they can occur away from a stalled condition and occur at one dominant frequency. NSV occurs at non-integral multiples of the shaft rotational frequencies, far from the classical flutter regime. The blade vibrations due to NSV are generally frequency and phase locked. Hence, they occur at one dominant frequency and one interblade phase angle. Furthermore, NSV results from large amplitude flow disturbances so a full nonlinear, unsteady, viscous Navier-Stokes solver must be used to study the flow.

1.2 Previous Work

Numerous other researchers have observed and studied NSV related phenomena in turbomachinery and areas that have received considerable interest are tip flow instability, vortex shedding, and rotating stall. Examples of work in this area can be found in Mailach [7], Mailach et al. [8] [9], Marz et al. [10] [11], Inoue et al. [12], Lenglin and Tan [13], Vo [14], Thomassin and Vo [15], Kielb et al. [3], and Sanders [16]. Mailach et al. [9] presents experimental results from both a four stage low speed

research compressor and a linear cascade. The tip instability was found near the stall line with a large tip clearance and the frequency was characterized by a Strouhal-type number using the radial distance of the clearance vortex as the characteristic length. They conclude that the tip flow instability is a vortex interaction effect that produces a rotating structure with higher order modes. Camp [17] reports that this problem has also been observed in a high speed compressor and an experimental study was performed. He proposed that the vortex shedding can be amplified by duct or cavity modes in the annulus. A helical acoustic structure (circumferential Mach number of 0.84) was found using casing dynamic pressure transducers. He reported lock-in type behavior when the vortex shedding frequency is near a duct resonance, resulting in large amplitude unsteadiness and step changes in frequency as the flow rate was changed.

More recently, Sanders [16] describes an NSV problem similar to rotating stall on a composite fan stator. An instability is created in high Mach number regions between a shock and downstream separation, causing large amplitude periodic unsteadiness [16]. Sanders investigated this problem both experimentally and computationally. Although the CFD simulations were not able to predict the onset of NSV, the instantaneous flow field snapshots correlated well with the engine test visualization flow patterns. Thomassin and Vo [15] studied an axial compressor rotor blade. They described the underlying physical mechanism of NSV as the blade tip trailing edge flow acting as an impinging jet on the pressure side of an adjacent blade, based on the jet core feedback theory. A simple model was developed to predict the rotor speed when NSV will occur and verified by two separate rotor designs.

There have also been numerous computational studies performed to compare with measured rig data. For example, Marz et al. [11] found a tip flow instability on a low speed fan rig near the stall line and with a large tip clearance. Their unsteady

CFD model predicted a frequency of 950 Hz as compared to the measured value of 880 Hz. Similarly, Lenglin and Tan [13] used a three-dimensional viscous CFD model to study tip clearance flow and predicted a Strouhal number (based on the rotor chord) of 0.7 for the unsteadiness and found unsteady loadings in the tip region as large as 30% of the static pressure coefficient. Kielb et al. [3] also performed numerical simulations and experimental investigation of a non-synchronous excitation phenomenon for a first stage compressor rotor. They predicted a NSV frequency approximately 9% less than that measured in the rig test using the unsteady CFD code TURBO [18]. Although these results show fairly good agreement with experiment, the CFD time domain models can be very computationally expensive to run just a single aerodynamic condition.

1.3 Current Industry Design Approach

In order to "solve" the NSV problem in turbomachinery, industry commonly changes the variable geometry or vane schedule. This is accomplished by adjusting the angle of variable angle inlet guide vanes. However, as a result, the engine suffers a loss of efficiency. Another possible solution is to add dampers or alter a blade's design to lessen the blade's response. While these are adequate fixes for the problem, they can be costly and often add unnecessary weight to the engine. Therefore, there is a strong motivation to develop techniques to predict the occurrence of NSV and the expected amplitude of the blade vibrations.

Currently, industry analysis methods treat NSV much like a forced response problem. A three-dimensional (3-D) viscous CFD time marching scheme is applied to the governing Navier-Stokes equations. The CFD analysis provides the frequency of the flow instability and a structural code (ANSYS, etc.) computes the fundamental blade mode frequencies. Then, analogous to the forced response problem, it is assumed that

the worst case scenario is when the frequency of the aerodynamic instability is coincident with a blade mode frequency, resulting in high amplitude blade vibrations. This possible point of intersection have been identified on the Campbell diagram in Figure 1.1. It has been seen that the stress levels at the NSV condition can be high enough to cause HCF failure of the blades.

However, this method has some important limitations. In particular, it can very computationally expensive to run a 3-D unsteady, viscous time marching CFD calculation. The analysis can take up to a month to determine the frequency for one aerodynamic condition. In addition, the simulation does not include blade motion. Although this eliminates classical flutter as a mechanism for unsteadiness, it also assumes that the maximum blade response is at a blade natural frequency. This assumption has been investigated in this dissertation, as well as a fully coupled aeroelastic model.

In this work, a novel frequency domain harmonic balance method [5] was used to solve the governing Navier-Stokes equations (see also Hall et al. [19] and Thomas et al. [20]). For periodic unsteady flows, such as the transonic flow through a turbomachinery cascade, the HB method requires considerably less computational time than traditional time-marching CFD methods, and it can model nonlinear effects brought about by large amplitude flow disturbances. The solution to the HB equations requires the user to input the frequency of the flow instability. However, the purpose of the study is to find the shedding frequency as one of the unknowns of the solution. One simple method is to choose a wide range of frequencies and compute the solution residual of the harmonic balance equation for each case. However, previous studies by McMullen, et al. [21] indicate that the solution residual drops off suddenly and only at the precise NSV frequency. As a result, this method of searching for the natural shedding frequency can easily miss the correct frequency, and it requires numerous

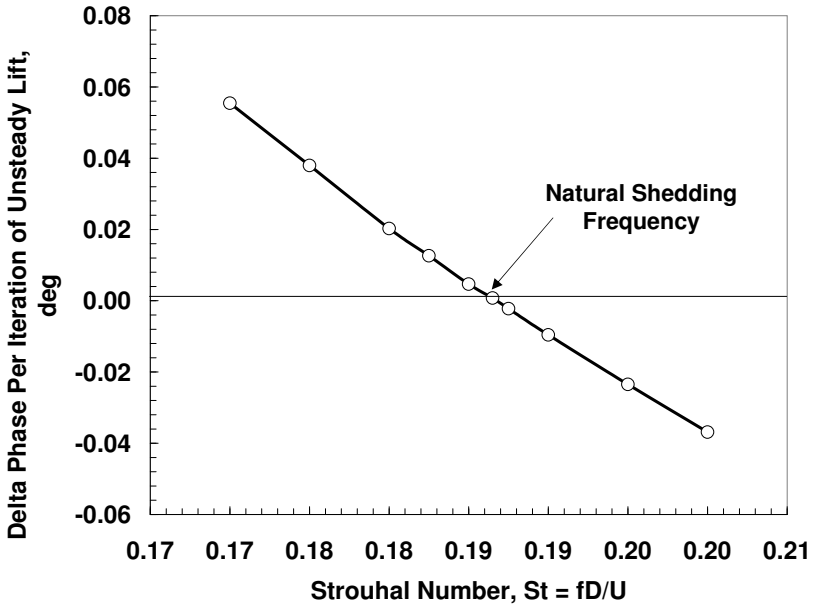

Figure 1.2: Demonstration of phase error method.

runs of the HB code.

Therefore, a novel frequency search technique has been developed by Hall et al. [2] For a given input frequency, the converged solution will have a constant phase change per iteration of an unsteady first harmonic quantity, such as unsteady lift. When an incorrect frequency is input, the HB method will predict that the phase change per iteration is greater than or less than zero. Once this value is calculated for a few different frequencies, it becomes readily apparent that the phase is nearly linearly related to the assumed frequency. The nearly exact frequency can be calculated by determining the frequency for which the phase shift is zero as shown in Figure 1.2. This can be accomplished by simple interpolation with as few as two HB solutions.

One disadvantage of the standard harmonic balance analysis is that it can only handle one fundamental frequency and its higher harmonics. A multiple frequency HB method has been developed by Ekici et al. [22] but in application to NSV, it requires the user to guess two or more fluid instability frequencies, which is no longer

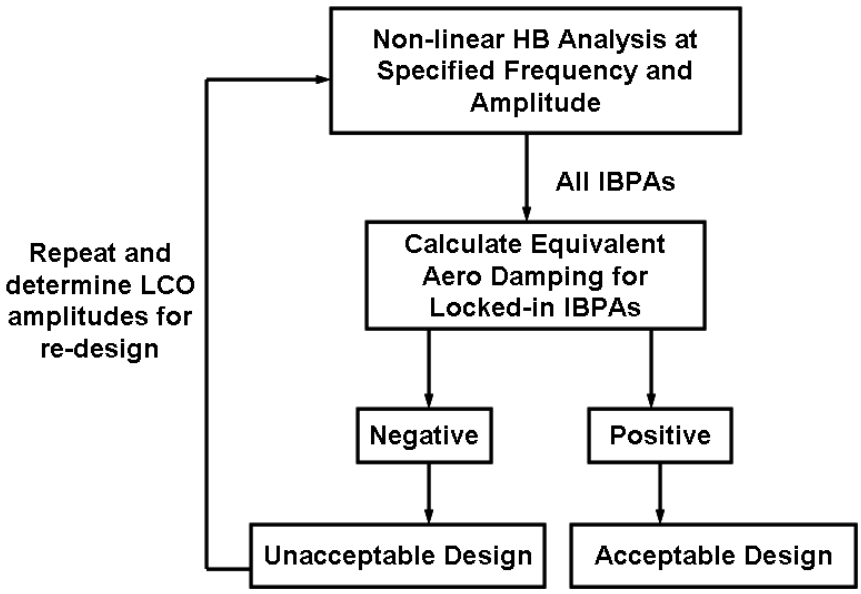

Figure 1.3: Flow diagram of enforced motion design procedure.

computationally efficient.

This method was very effective for 2-D applications such as a circular cylinder and a 2-D airfoil section. However, when applied to a full 3-D blade, HB solution stability problems were encountered because the fluid dynamic instability contains multiple (irrational) frequencies. As a result, an alternative method was developed.

1.4 Enforced Motion Design Method

This dissertation presents results from a new preliminary design method which uses blade motion to attempt to force the NSV frequency to lock-on to a blade vibration frequency at a specified critical amplitude. This enforced motion design method is suitable for all NSV related phenomena at a fraction of the computational cost. The proposed industry design procedure is explained below and shown in Figure 1.3. It is easily adoptable to existing preliminary design methods because a linear flutter analysis is typically already conducted at infinitesimal amplitude. To study NSV using the enforced motion method, the nonlinear HB technique is applied for a specific mode

shape at a chosen amplitude and frequency for a range of interblade phase angles (IBPAs). In a design analysis, the engine manufacturers' main concern is whether or not the blade vibratory amplitudes will be large enough to ultimately cause HCF of the blades. The chosen amplitude will therefore be a maximum allowable blade amplitude and the frequency will be the blade mode frequency of interest.

For the range of IBPAs, two distinct conditions are possible at the prescribed blade frequency and critical amplitude. First, the fluid natural frequency may be locked-in to the blade frequency. For this case, only a single frequency, the blade frequency, is observed experimentally. This allows for the use of the standard harmonic balance analysis. The HB solution residual within the lock-in region converges to machine zero. The second condition occurs when the fluid is oscillating at a frequency other than the blade mode frequency. For this case, two distinct frequencies are present and the current numerical method fails to converge. It is assumed that the condition for which the frequencies are unlocked is a low amplitude, off-resonant response.

For the IBPAs that are locked-on, the unsteady modal forces for each harmonic can be determined from the calculated Fourier coefficients. The imaginary part of the first harmonic of the modal force determines the aeroelastic stability of the rotor. The equivalent (linear) damping is proportional to the negative of the imaginary part of the modal force and is given by

$$\zeta = \frac{-Im(\frac{\partial Q}{\partial \xi})}{2M\omega^2} \tag{1.1}$$

$Im(\frac{\partial Q}{\partial \xi})$ is the modal force in the linear region, M is the modal mass, and ω is the forced oscillation frequency for the lock-in condition. This mode is acceptable if the equivalent damping is greater than zero for all IBPAs. The enforced amplitude for which the imaginary part goes from positive to negative damping determines the limit cycle oscillation (LCO) amplitude. If a negative damping is achieved for any IBPA,

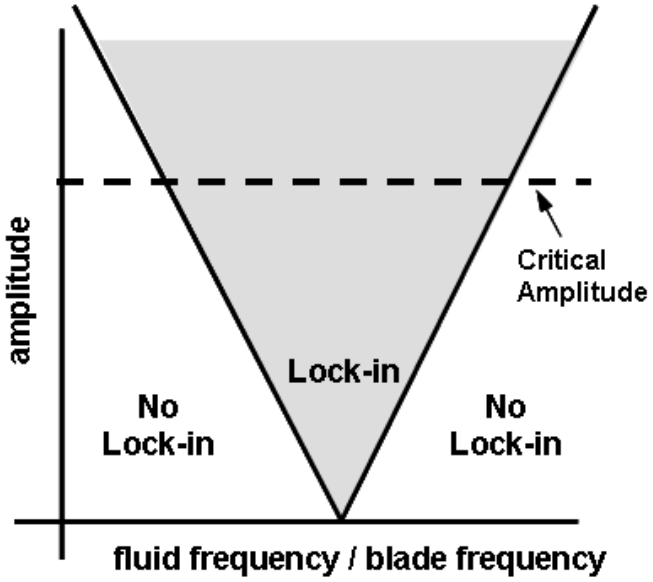

Figure 1.4: Schematic of lock-in region for blade re-design.

the LCO amplitude is greater than the accepted critical amplitude so the design is unacceptable.

1.4.1 Blade Re-design

For re-design, the nonlinear HB technique can be repeated for a range of frequencies and amplitudes at the least stable IBPA to determine the LCO amplitude for each frequency. The best design is then at the frequencies with low LCO amplitudes and therefore minimizes high amplitude blade vibrations.

A schematic demonstrating the enforced motion lock-in region is shown in Figure 1.4. As described previously, lock-in is achieved when the fluid natural frequency "jumps" to the blade vibration frequency at a particular amplitude and therefore only the blade frequency is present in the system. The lock-in region is generally centered about the blade mode frequency and it is assumed that the condition for which the frequencies are unlocked is low amplitude and off-resonant.

1.5 Research Objectives

The objectives for this research are:

Objective 1: Develop a design tool for studying NSV by searching directly for the frequency of the aerodynamic instability.

One approach to understanding NSV is to model the flow through a single blade passage and directly search for the frequency of the instability. One disadvantage of this method is that the computations can be prohibitively expensive, especially for routine use by industry. For most flows through transonic turbomachinery, the flow can be assumed to be fully developed and periodic in time and conventional time-accurate CFD calculations can be particularly inefficient. Therefore, numerous methods have been developed to take advantage of the time-periodic nature of the flow including the time-linearization approach [23] [24] [25] [26] [27] [28], time-averaging technique [29] [30] [18], and the harmonic balance (HB) method [5] [19] [31] [20] [21]. Of these three methods, the unsteady, nonlinear harmonic balance technique has the ability to model large flow disturbances and strong linearities found in turbomachinery and takes one to two orders of magnitude less computational time than traditional time marching techniques. However, typically in a flow analysis, the oscillation frequency is known beforehand and therefore serves as an input to the system. Since the overall goal of this research is to find the NSV frequency, a new phase error method is employed to achieve quick solution convergence. This novel frequency search technique utilizes the phase difference between successive iterations of an unsteady first harmonic quantity such as unsteady lift and was developed by Kenneth Hall [2]. It requires only a few harmonic balance solution computations to determine the precise NSV frequency. However, the main shortcoming of this method is that it does not consider blade motion. The direct frequency search method assumes the

worst case scenario is when the blade and the fluid frequencies are coincident.

Objective 2: Due to limitations of the direct frequency search method, develop a design tool that utilizes enforced motion to cause lock-on of the aerodynamic instability to a particular blade mode frequency.

Another design approach was developed when problems were encountered using the harmonic balance method. In particular, the harmonic balance solver can only handle one fundamental frequency and its harmonics. Consequently, in cases in which the fluid dynamic instability contained multiple (irrational) frequencies, the HB method failed to predict the NSV frequencies. A multiple frequency harmonic balance method has been developed by Ekici et al. [22] but it requires the user to guess two or more frequencies which is no longer computationally efficient. Moreover, in the design analysis, the exact frequency and amplitude of the NSV are not necessarily needed. Engine manufacturers are primarily concerned with whether or not the blade vibratory amplitude will be large enough to ultimately cause the blade to fracture.

The new method uses enforced motion to force the fluid frequency to lock-on to the blade vibration frequency at a particular amplitude. Instead of determining the frequency and amplitude directly, one can calculate the equivalent aerodynamic damping (stability) of the system and determine if it is positive or negative at a critical amplitude. A negative damping indicates that the design is not unacceptable or the NSV LCO amplitude is greater than the critical value. Therefore, the process can be repeated with a larger amplitude until a positive damping value is achieved. It is possible to determine the precise amplitude by honing in on the point for which the damping goes from positive to negative. It is assumed that the condition for which the frequencies are unlocked is a low amplitude, off-resonant response and therefore not considered significant.

Objective 3: Apply the proposed direct frequency search method and enforced motion method to a cylinder, 2-D airfoil section, and 3-D cases from industry to determine the importance of blade motion in NSV design approaches.

The test cases considered are a circular cylinder (at low Re), a 2-D airfoil section of a modern first stage compressor rotor blade near the tip at an off-design condition (to achieve NSV response), and the full compressor blade that encountered NSV in compressor rig testing. The 2-D shedding flow about a circular cylinder is a good test case because numerous experimental and computational data are available for comparison. Since there is no 2-D experimental data for this airfoil section, the harmonic balance method results were compared to previous time domain results. The 3-D blade results were compared with the compressor rig test data in which the blade experienced a coupled suction side vortex unsteadiness (near 75 percent span) and tip flow instability [3] at a frequency of 2600 Hz. Furthermore, the lock-in effect was studied for all three cases. The specific application of the design methods to the test cases is detailed in subsequent chapters. For each case, two distinct conditions are investigated. First, the natural shedding frequency is determined without motion. Next, we consider the enforced motion case in which the body is forced to vibrate at prescribed frequencies other than its natural shedding frequency. The results indicate how both the natural shedding frequency and the blade natural frequency should be considered for NSV design analysis.

1.6 Research Impact

This research has provided a new approach to understand a complex flow phenomenon encountered in turbomachinery configurations. The proposed enforced motion method utilizes a novel nonlinear harmonic balance method which will save

designers 1-2 magnitudes of computational time over existing time marching CFD techniques. Also, a full aeroelastic model is used to investigate the importance of including blade motion in the design approach. The lock-in concept is uniquely applied to a modern front stage transonic HPC cascade. In this method, blade motion is used to force the frequency of the instability to lock-on to a blade mode natural frequency at a particular critical amplitude. The lock-in phenomenon has been well-studied for cylinder motion, but only more recently has it been investigated for vortex shedding flow behind a NACA0012 airfoil section and a subsonic blunt trailing-edge turbine cascade. Furthermore, by building on the knowledge obtained by investigating 2-D applications such as a circular cylinder and 2-D airfoil section, a novel, efficient preliminary design tool for NSV is presented. This method is easily adoptable to existing preliminary design practice because a linear flutter analysis is typically already conducted at infinitesimal amplitude. The proposed method would therefore only require the designer to determine the aerodynamic damping for all IBPAs at a prescribed critical amplitude. The results will indicate that blade motion is important and necessary to adequately design for NSV. Therefore, this research will immensely impact the engine industry. Engineers will be able to predict the occurrence of NSV before testing at a relatively small cost.

1.7 Organization

To develop an efficient design method for non-synchronous vibrations, a couple different test cases and design approaches were investigated. Each case and the application of the different methods are addressed in a separate section. These sections detail the application of both the direct frequency search method and the enforced motion design method to a circular cylinder, 2-D airfoil section, and finally a full 3-D compressor blade. Ultimately, a quick, systematic, and effective design method will be

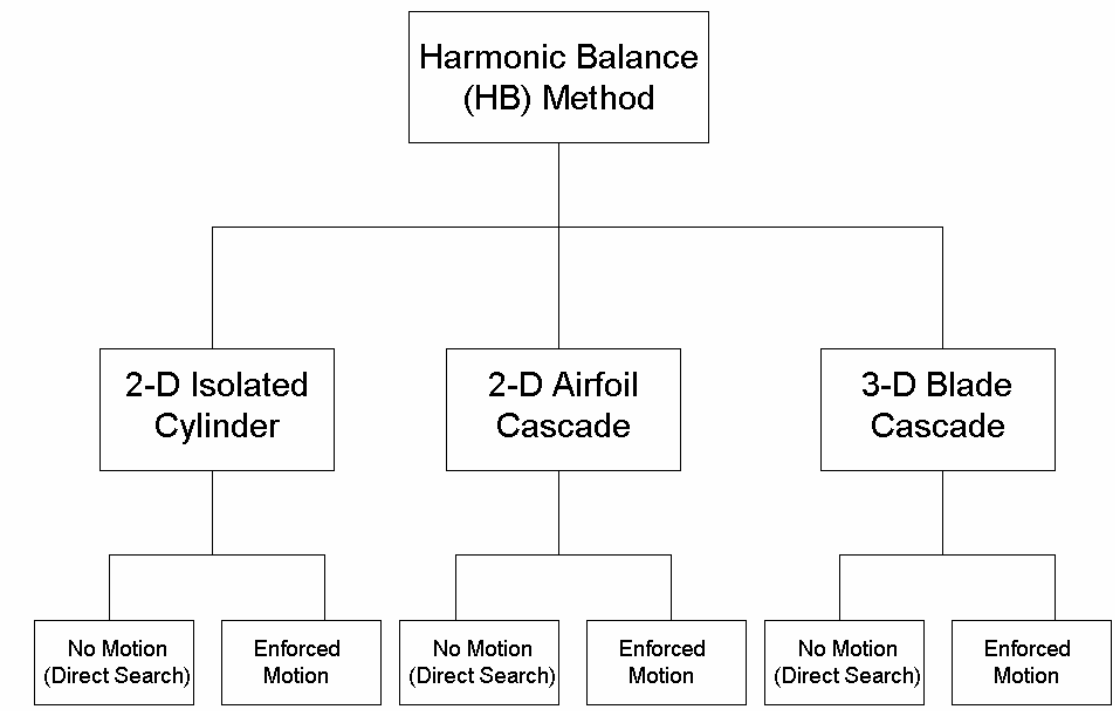

Figure 1.5: Flow diagram of organization of research results.

proposed for industry use. A flow diagram of the paper organization is presented in Figure 1.5 and brief explanations for each chapter follow.

Chapter 2 introduces the harmonic balance method and its application to the governing flow equations. The solution technique, discretization scheme, and boundary and initial conditions are also presented.

Chapter 3 introduces the shedding flow about a stationary circular cylinder and the application of a unique phase error method to search directly for the shedding frequency. The unsteady forces are also calculated and all results are compared with existing experimental and computational data.

Chapter 4 discusses the lock-in region for a cylinder undergoing prescribed motion. The aerodynamic damping is calculated within the lock-in region and the stability is examined. The results are compared with experimental data and the enforced motion

method is demonstrated.

Chapter 5 presents a study of a flow instability about a stationary 2-D airfoil cascade section of a modern front stage HPC near the tip at an off-design condition. The frequency of the instability is determined and compared with time domain results.

Chapter 6 discusses the use of enforced motion to study the lock-in effect for a 2-D airfoil cascade undergoing a periodic pitch motion. Two different interblade phase angles are investigated and the stability of the rotor is examined. Furthermore, the proposed enforced motion design approach is applied for this 2-D cascade undergoing pitching motion.

Chapter 7 discusses the shortcomings of the direct search method and introduces the application of the enforced motion method to a modern front stage compressor rotor blade that experienced NSV in rig testing. Furthermore, a procedure for blade re-design (frequency changing) is presented.

Chapter 8 concludes the research and suggests future applications and areas of improvement in the enforced motion method.

Chapter 2

Governing Equations and Harmonic Balance Theory

In general, the unsteady perturbations in NSV applications are significant and serve as a useful test case for the verification of the harmonic balance method as a valuable tool for solving NSV problems in turbomachinery. Two currently available analysis techniques, namely the time domain approach and the time-linearized frequency domain approach, are considered and the merits of each are examined. Next, the harmonic balance method used in this study will be described. For time-periodic flows, the HB method can be computationally more efficient than the other approaches and it is not limited by the assumptions required by a linearized solution. Finally, the HB method is applied to the governing three-dimensional Navier-Stokes equations.

2.1 Time-Domain Approach

In the past, most researchers have employed a time-domain approach to model the fluid flow over bluff bodies [32] [33] [30]. In this case, the governing Navier-Stokes equations are discretized over the computational grid and then the flow solution is marched in time using conventional CFD techniques and applying appropriate unsteady boundary conditions. The discretization of the flow equations requires the solution of a set of coupled nonlinear equations at each physical time step. Commonly, an inner iteration is introduced with a pseudotime variable and marched to a steady state. The converged solutions obtained at the end of the inner iteration represents a solution of the equations at the end of the physical time step [31]. Therefore,

this procedure must be repeated numerous times to achieve one physical time step and resolve the features of one period in the oscillation of the flow. Many convergence acceleration techniques such as multi-grid and variable pseudotime stepping can be implemented in the inner iteration. However, as more periods are needed for convergence, the computations can become extremely costly. This approach is straightforward to implement and can model both nonlinear as well as linear disturbances but it typically takes considerable computational time to ensure numerical stability. Therefore, this approach can become prohibitively expensive for routine use by industry to predict and design for NSV.

2.2 Time-Linearized Frequency Domain Approach

Another popular technique for modelling the flow over turbomachinery blades is the time-linearized frequency domain approach. This method has been used to model transonic flow problems as well as two- and three-dimensional viscous flows in turbomachinery [28] [26]. In this method, the problem is divided into two parts: the steady flow and the unsteady perturbations in the flow. The steady, or time-mean, part of the flow is solved using well-known CFD techniques and the unsteady part is assumed to be small and harmonic in time ($e^{j\omega t}$). The governing Navier-Stokes equations can then be linearized about the mean flow solution to determine a set of equations that describe the unsteady flow component and they can be solved relatively easily. By replacing the time derivative by $j\omega$ where ω is the frequency of the unsteady flow disturbance, the resulting time-linearized equations can be solved inexpensively. A solution to the complex harmonic amplitude is obtained at a given frequency. When compared to unsteady time marching methods, the time-linearized frequency domain method is much more efficient but it is limited by the linear assumption of unsteadiness.

2.3 Harmonic Balance Approach

This study utilizes the harmonic balance technique for nonlinear, unsteady flows developed at Duke University by Kenneth Hall in 2000 [5]. It was originally developed as a mathematical tool to study the behavior of harmonic ordinary differential equations [34]. However, in recent years, Hall extended the application to the study of turbomachinery flows. In this novel method, the unsteady flow is assumed to be periodic time and can be represented by a Fourier series with frequencies that are integer multiples of the fundamental excitation frequency. Then, using the harmonic balance technique, a set of coupled partial differential equations is obtained for the unknown Fourier coefficients of the flowfield. A source term, the time derivative of the conservation variables with respect to time, is derived in subsequent sections and accounts for the unsteadiness. Finally, a pseudo-time term is introduced into the harmonic balance equations and the solution is marched like a steady CFD solver. From this result, the lift, drag, etc. for each harmonic can be determined from the calculated Fourier coefficients. For a given problem, it is desirable to use the minimum number of harmonics because the computational cost is proportional to the number of harmonics included. However, for many applications, only a few higher harmonics are needed to achieve engineering accuracy. Local time stepping, preconditioning, and multi-grid can be used to accelerate convergence. Therefore, a key aspect of the methodology is its ability to exploit the use of conventional CFD techniques.

2.3.1 Governing Equations

The transonic flow in turbomachinery cascades can be best represented by the three-dimensional Navier-Stokes equations for unsteady, nonlinear flow. The derivation of these equations is well documented in literature and arises from applying three con-

servation laws: conservation of mass, conservation of momentum, and conservation of energy. The flow is assumed to be compressible and viscous. Therefore, the resulting equations of motion written in a frame of reference attached to the blade in integral form are:

$$\frac{\partial}{\partial t}\int\int\int_V UdV + \int\int_A (F - U\frac{\partial f}{\partial t}, G - U\frac{\partial g}{\partial t}, H - U\frac{\partial h}{\partial t}) \cdot dA = \int\int\int_V SdV \quad (2.1)$$

Here, the x, y, and z components of the displacement of the control volume are denoted by f, g, and h and the elemental control volume and control surface are dV and dA respectively. U is a vector of conservation variables, F, G, and H are flux vectors in the x, y, and z directions, and S is the source vector.

Based on the strong conservative law form of the Navier-Stokes equations given above, the vector U and the inviscid and viscous components of F, G, H and S can be written in vector form as:

$$U = \begin{pmatrix} \rho \\ \rho u \\ \rho v \\ \rho w \\ \rho e \end{pmatrix} \quad (2.2)$$

$$F = \begin{pmatrix} \rho u \\ \rho u^2 + p - \tau_{xx} \\ \rho uv - \tau_{xy} \\ \rho w - \tau_{xz} \\ \rho u h_e - \tau_{xh} \end{pmatrix}, G = \begin{pmatrix} \rho v \\ \rho uv - \tau_{yx} \\ \rho v^2 + p - \tau_{yy} \\ \rho vw - \tau_{yz} \\ \rho v h_e - \tau_{yh} \end{pmatrix}, H = \begin{pmatrix} \rho w \\ \rho uw - \tau_{zx} \\ \rho vw - \tau_{zy} \\ \rho w^2 + p - \tau_{zz} \\ \rho w h_e - \tau_{zh} \end{pmatrix} \quad (2.3)$$

$$S = \begin{pmatrix} 0 \\ 0 \\ \rho(\Omega^2 y + 2\Omega w) \\ \rho(\Omega^2 z - 2\Omega v) \\ 0 \end{pmatrix} \quad (2.4)$$

By examining the governing equations in compact vector form, the first row corresponds to the continuity equation, the second, third and fourth rows are the momen-

tum equation in the x, y, and z directions respectively, and the final equation is the conservation of energy equation. In these equations, ρ is the density of the fluid; u, v, and w are the velocity components in the x, y, and z directions, respectively; e is the total internal energy; h_e is the total enthalpy; and p is the static pressure. The source term contains the centripetal and Coriolis forces per unit volume, where Ω is the rotational frequency.

If the divergence theorem is applied, a differential form of the Navier-Stokes is obtained:

$$\frac{\partial U}{\partial t} + \frac{\partial F(U)}{\partial x} + \frac{\partial G(U)}{\partial y} + \frac{\partial H(U)}{\partial z} = S \tag{2.5}$$

Assuming the fluid (air in this case) is an ideal gas with constant specific heats, it is possible to express the pressure and enthalpy in terms of the conservation variables. The equation of state is given by:

$$p = \rho R_{gas} T \tag{2.6}$$

where T is the temperature and R_{gas} is the universal gas constant. In addition, for a perfect gas, the following relationships exist:

$$e = c_v T, \quad h_e = c_p T, \quad \gamma = \frac{c_p}{c_v}, \quad c_v = \frac{\gamma}{\gamma - 1}, \quad c_p = \frac{\gamma R_{gas}}{\gamma - 1} \tag{2.7}$$

where c_v is the specific heat at constant volume, c_p is the specific heat at constant pressure, and γ is defined as the ratio of these two specific heats. Therefore, the pressure and enthalpy can be determined in terms of the conservation variables and are given by:

$$p = (\gamma - 1)\rho[e - \frac{1}{2}(u^2 + v^2 + w^2) + \frac{1}{2}\Omega^2 R^2] \tag{2.8}$$

$$h_e = \frac{\rho e + p}{\rho} \tag{2.9}$$

where R is the radial distance from the x-axis. The shear stresses τ_{xx}, τ_{xy}, τ_{xz}, τ_{yy}, τ_{yz}, and τ_{zz} can be written in terms of the viscosity and the shear rate in the x, y, and z directions, respectively:

$$\tau_{xx} = \mu\left(\frac{4}{3}\frac{\partial u}{\partial x} - \frac{2}{3}\frac{\partial v}{\partial y} - \frac{2}{3}\frac{\partial w}{\partial z}\right), \quad \tau_{xy} = \mu\left(\frac{\partial u}{\partial y} + \frac{\partial v}{\partial x}\right) \tag{2.10}$$

$$\tau_{xz} = \mu\left(\frac{\partial u}{\partial z} + \frac{\partial w}{\partial x}\right), \quad \tau_{yy} = \mu\left(\frac{4}{3}\frac{\partial v}{\partial y} - \frac{2}{3}\frac{\partial u}{\partial x} - \frac{2}{3}\frac{\partial w}{\partial z}\right) \tag{2.11}$$

$$\tau_{yz} = \mu\left(\frac{\partial v}{\partial z} + \frac{\partial w}{\partial y}\right), \quad \tau_{zz} = \mu\left(\frac{4}{3}\frac{\partial w}{\partial z} - \frac{2}{3}\frac{\partial u}{\partial x} - \frac{2}{3}\frac{\partial v}{\partial y}\right) \tag{2.12}$$

where μ is the dynamic molecular viscosity. Furthermore, the terms τ_{hx}, τ_{hy} and τ_{hz} in the energy equation are given by:

$$\tau_{hx} = u\tau_{xx} + v\tau_{xy} + w\tau_{xz} + q_x \tag{2.13}$$

$$\tau_{hy} = u\tau_{yx} + v\tau_{yy} + w\tau_{yz} + q_y \tag{2.14}$$

$$\tau_{hz} = u\tau_{zx} + v\tau_{zy} + w\tau_{zz} + q_z \tag{2.15}$$

where q_x, q_y, and q_z are the x, y, and z components of the heat flux and can be written as:

$$q_x = -\left(\frac{\mu c_p}{Pr_L}\right)\frac{\partial T}{\partial x}, \quad q_y = -\left(\frac{\mu c_p}{Pr_L}\right)\frac{\partial T}{\partial y}, \quad q_z = -\left(\frac{\mu c_p}{Pr_L}\right)\frac{\partial T}{\partial z} \tag{2.16}$$

where Pr_L is the laminar Prandtl number and $\partial T/\partial x$, $\partial T/\partial y$, and $\partial T/\partial z$ are the temperature gradients in the x, y, and z directions, respectively. The variable μ is determined from Sutherland's Law and results from the use of a dynamic molecular viscosity. Sutherland's formula for viscosity is given by:

$$\mu = \mu_0\left(\frac{T}{T_0}\right)^{3/2}\frac{T + S_0}{T_0 + S_0} \tag{2.17}$$

where $\mu_0 = 3.583E^{-7}$ at a reference temperature $T_0 = 491.4$ R and the constant $S_0 = 199.8$ R. For air at standard conditions, $Pr_L = 0.72$. The turbulence model used in this study is the one-equation model proposed by Spalart-Allmaras [35]. Therefore, by using knowledge of the flow and the principles of thermodynamics, it is now possible to implement the harmonic balance method to solve the governing three-dimensional, nonlinear, unsteady Navier-Stokes equations.

2.3.2 Non-Dimensionalization

In order to make the computations easier, the equations are often put into a non-dimensional form. This allows the system parameters such as Reynolds number, Mach number, etc. to be varied independently. Therefore, the variables of interest were non-dimensionalized as follows:

$$x' = \frac{x}{L_{ref}}, \quad y' = \frac{y}{L_{ref}}, \quad z' = \frac{z}{L_{ref}} \tag{2.18}$$

$$u' = \frac{u}{V_{ref}}, \quad v' = \frac{v}{V_{ref}}, \quad w' = \frac{w}{V_{ref}} \tag{2.19}$$

$$p' = \frac{p}{P_{ref}}, \quad T' = \frac{T}{T_{ref}}, \quad \rho' = \frac{\rho}{\rho_{ref}}, \quad \mu' = \frac{\mu}{\mu_{ref}}, \quad \Omega' = \frac{\Omega}{\Omega_{ref}} \tag{2.20}$$

where the reference quantities are given by Table 2.1.

By rewriting the equations in dimensionless form, it makes it easier to compare with experimental results. As a result, the system's behavior and dependence on various parameters can be extracted more easily.

2.3.3 Application of Harmonic Balance Method

This method has been well-documented in the literature and can be found in Hall et al. [5] [19] [20] so only a brief description is given here. To introduce the harmonic

Reference	Definition
L_{ref}	User-defined constant length scale
p_{ref}	User-defined total pressure
T_{ref}	User-defined total temperature
ρ_{ref}	Total density defined as $\rho_{ref} = \frac{p_{ref}}{R_{gas}T_{ref}}$
a_{ref}	Freestream total acoustic velocity defined as $a_{ref} = \sqrt{\gamma R_{gas} T_{ref}}$
V_{ref}	Reference velocity defined as $V_{ref} = \frac{a_{ref}}{\sqrt{\gamma}}$
μ_{ref}	Reference viscosity defined as $\mu_{ref} = \rho_{ref} V_{ref} L_{ref}$
Ω_{ref}	Reference rotational frequency defined as $\Omega_{ref} = \frac{V_{ref}}{L_{ref}}$

Table 2.1: Reference quantities and corresponding definitions

balance method in a simplistic manner, one can assume that the flow is inviscid [5]. However, this method is easily extendable to the full, viscous Navier-Stokes equations. Most often, the flows of interest in turbomachinery can be assumed to be periodic in time. Therefore, the conservation variables can be represented as a Fourier series in time with spatially varying coefficients. For example,

$$U(x,y,t) = A_0(x,y,z) + \sum_{n=1}^{\infty}[A_n(x,y,z)\cos(wnt) + B_n(x,y,z)\sin(wnt)] \qquad (2.21)$$

Here, ω is the frequency of the flow unsteadiness and A_0, A_n, and B_n are the Fourier coefficients of the flow variables.

In theory, one would sum the variables over all n but in practice, the solution is truncated and summed over a finite number of terms, N_H. Next, the Fourier expansions are substituted into the Navier-Stokes equations and expressions for the conservation of mass, momentum, and energy can be developed. The terms in the resulting equations are grouped by frequency and each frequency component must satisfy the conservation equations individually.

The vector $\tilde{U}$ is a vector of the Fourier coefficients for each conservation variable. In addition, since the conservation variables are all real-valued, it is only necessary to store the Fourier coefficients for non-negative n. For example, if N_H harmonics

are retained in the Fourier series, then $2N_H + 1$ coefficients must be stored for each flow variable. There is one for the zeroth harmonic (mean flow) and $2N_H$ for the real and imaginary components of the rest of the harmonics.

2.3.4 Utilization of Time Domain Methodology

Next, for computational efficiency, the variables are cast back into the time domain by assuming that the values of U, F, G, and H can be evaluated at $2N_H + 1$ equally spaced points in time over one temporal period. Therefore,

$$U^* = E^{-1}\tilde{U} \tag{2.22}$$

where U^* is a vector of the conservation variable evaluated at $2N_H + 1$ points and E^{-1} is the inverse discrete Fourier transform operator. Conversely,

$$\tilde{U} = EU^* \tag{2.23}$$

It is important to note that E and E^{-1} are square matrices since the number of time levels is equal to the number of Fourier coefficients. Therefore, the vectors U^* and $\tilde{U}$ can be written as

$$\tilde{U} = \begin{pmatrix} A_0 \\ A_1 \\ \vdots \\ A_N \\ B_0 \\ B_1 \\ \vdots \\ B_N \end{pmatrix}, \qquad U^* = \begin{pmatrix} U_1 \\ U_2 \\ \vdots \\ U_{2N_H+1} \end{pmatrix} \tag{2.24}$$

Similar expressions can be developed for the flux vectors and the new governing vector equation becomes:

$$\frac{\partial U^*}{\partial t} + \frac{\partial F^*}{\partial x} + \frac{\partial G^*}{\partial y} + \frac{\partial H^*}{\partial z} = S^* \tag{2.25}$$

Equation 2.25 consists of 5 x $(2N_H + 1)$ equations. The advantage of this method over the classical form of the harmonic balance equations is that the fluxes are only of order N_H operations to compute. The time derivative term is approximated by the pseudospectral operator, D. First, note that:

$$\frac{\partial U^*}{\partial t} = \frac{\partial E^{-1}}{\partial t}\tilde{U} \tag{2.26}$$

Also, by making use of equation 2.23, the pseudospectral becomes:

$$\frac{\partial U^*}{\partial t} = \frac{\partial E^{-1}}{\partial t}EU^* = DU^* \tag{2.27}$$

Therefore, the resulting harmonic balance equations are:

$$DU^* + \frac{\partial F^*}{\partial x} + \frac{\partial G^*}{\partial y} + \frac{\partial H^*}{\partial z} = S^* \tag{2.28}$$

To obtain the solution to the harmonic balance equations, a "pseudo-time" term is introduced. This allows the equations to be marched to a steady state using conventional CFD techniques. Therefore, the final equation becomes

$$\frac{\partial U^*}{\partial \tau} + \frac{\partial F^*}{\partial x} + \frac{\partial G^*}{\partial y} + \frac{\partial H^*}{\partial z} + DU^* = S^* \tag{2.29}$$

where τ is a new time variable merely used to march the equation to a steady state. This equation very closely resembles the differential form of the Navier-Stokes equations (see Equation 2.30). Therefore, existing well-established steady CFD techniques can be used to solve the nonlinear harmonic balance equations. This method is similar to the dual time-step method [36] [37] for solving unsteady flows in the time domain. However, the harmonic balance approach has distinct advantages over the dual time step method. In particular, in the dual time-step method, one marches

from one time level to the next accurately, using pseudo-time to drive the residual of the time-accurate equations to zero. This process must be repeated over many time-steps for several periods until a periodic solution is reaches. The harmonic balance method stores the solution at only a few points over a single period, and the solutions at all the temporal points are advanced simultaneously using pseudo-time marching until the solution converges. In addition, a spectral operation can be used to compute the physical time derivative $\partial/\partial t$ since one solves for the solution over one complete period. The spectral time derivative is much more accurate than finite difference operators, which are used in the dual time stepping approach. Consequently, significantly fewer physical time levels are required using the harmonic balance method.

2.3.5 Lax-Wendroff Method

In general, the grid is constructed based on the geometric attributes of the body under consideration for a single blade passage. For the full, three-dimensional blade model, the multi-block H-O-H mesh topology is used. The O-type grid allows for good resolution near the blade surface. Furthermore, the H-type blocks near the inlet and exit far-field are nearly uniform in the tangential direction, providing good resolution of acoustic, vortical, and entropic waves. The EZ-turbo commercial code is used to generate the grid. A sample two-dimensional grid is shown in Figure 5.1. The flow properties at each point in the grid are then assigned a value based on the initial flow condition [33].

In particular, for the three-dimensional Navier-Stokes equations, a computational grid is generated for each time level and then the harmonic balance equations are discretized over the entire domain using common CFD techniques. The conservation variables are stored at each node of the grid for each time level. In this analysis,

Ni's two-step explicit Lax-Wendroff method was used to solve the harmonic balance equations. The Lax-Wendroff method is a node-centered conservative finite difference scheme. For the Navier-Stokes equations, the Lax-Wendroff scheme is second-order accurate in space and first order accurate in time due to viscous terms [32]. As before, the Navier-Stokes equations are given as:

$$\frac{\partial U}{\partial t} + \frac{\partial F(U)}{\partial x} + \frac{\partial G(U)}{\partial y} + \frac{\partial H(U)}{\partial z} = S \tag{2.30}$$

where U, F, G, H, and S are defined in the preceding section. The Lax-Wendroff method is developed from a Taylor series expansion of U in time:

$$U(x,y,z,t+T) = U(x,y,z) + \Delta t \frac{\partial U(x,y,z)}{\partial t} + \frac{\Delta t^2}{2}\frac{\partial^2 U(x,y,z)}{\partial t^2} + O(\Delta t^3) \tag{2.31}$$

The first derivative term can be determined from the governing equation and therefore can be written as:

$$\frac{\partial U}{\partial t} = -\left[\frac{\partial F}{\partial x} + \frac{\partial G}{\partial y} + \frac{\partial H}{\partial z}\right] + S \tag{2.32}$$

The second time derivative can be found by differentiating this equation with respect to time:

$$\begin{aligned}\frac{\partial^2 U}{\partial t^2} = -\left[\frac{\partial}{\partial x}\left(\frac{\partial F}{\partial U}\right)\left(\frac{\partial U}{\partial t}\right) + \frac{\partial}{\partial y}\left(\frac{\partial G}{\partial U}\right)\left(\frac{\partial U}{\partial t}\right) + \frac{\partial}{\partial z}\left(\frac{\partial H}{\partial U}\right)\left(\frac{\partial U}{\partial t}\right)\right] + \\ \left(\frac{\partial S}{\partial U}\right)\left(\frac{\partial U}{\partial t}\right)\end{aligned} \tag{2.33}$$

When these expressions are substituted back into the Taylor-series expansion for U, the resulting equation becomes:

$$\begin{aligned}U(t+T) = U(t) - \Delta t\left[\left(\frac{\partial F}{\partial x} + \frac{\partial G}{\partial y} + \frac{\partial H}{\partial z}\right) - S\right] - \\ \frac{\Delta t^2}{2}\left[\frac{\partial \Delta F}{\partial x} + \frac{\partial \Delta G}{\partial y} + \frac{\partial \Delta H}{\partial z}\right] + O(\Delta t^3)\end{aligned} \tag{2.34}$$

where $\Delta U = \frac{\partial U}{\partial t}\Delta t$, $\Delta F = \frac{\partial F}{\partial U}\Delta U$, $\Delta G = \frac{\partial G}{\partial U}\Delta U$, $\Delta H = \frac{\partial H}{\partial U}\Delta U$, and $\Delta S = \frac{\partial S}{\partial U}\Delta U$.

Therefore, the first derivative representation provides a first-order correction while the second derivative gives a second-order correction. This technique is applied to the harmonic balance method described in the previous section and the solution can be obtained by marching these equations in time at each grid point. A steady state is reached when the corrections are driven to zero. Since this method was originally developed for inviscid flow analysis, some small changes must be made to the integration scheme to handle the viscous components [32]. Finally, it is common to use an artificial viscosity to maintain stability in regions with large discontinuities and coarse grid spacing. In this study, both second and fourth difference numerical smoothing are used to capture shocks. Also, since only "steady" state solutions are needed, multi-grid and local time stepping methods can be used to accelerate convergence. Effectively, multi-grid uses a combination of fine grids and coarse grids to achieve both rapid solution convergence as well as accuracy.

2.3.6 Boundary and Initial Conditions

Finally, proper boundary and initial conditions must be enacted. In particular, at each iteration of the code, the surface, far-field, and periodic boundary conditions must be applied. The solid surface boundary conditions require that there be no flow through the surface. For viscous analysis, this amounts to a no-slip boundary condition on the airfoil surface. Furthermore, the periodicity conditions must be implemented. In order to accomplish this task, the solution U^* along the periodic boundary is Fourier transformed and the resulting Fourier coefficients $\tilde{U}$ are modified such that the complex periodic conditions are satisfied. The resulting Fourier coefficients on the computational boundary can then be inverse Fourier transformed and used on the boundary of the individual grids. Also, non-reflecting far field boundary

conditions should be applied at the inlet and exit such that there are no reflections of outgoing waves. Both upstream and downstream initial flow conditions are also prescribed.

2.4 Summary

The computational methodology has been detailed in this chapter. In particular, the harmonic balance method has been introduced and its application to the governing Navier-Stokes flow equations has been presented. The merits of the harmonic balance method over existing solution techniques was highlighted, namely its ability to model highly non-linear flow found in turbomachinery in one to two magnitudes less computational time than traditional time-accurate solvers. Ni's two-step explicit Lax-Wendroff scheme was used to solve the harmonic balance equations and the application of proper boundary conditions - surface, far-field, and periodicity - were discussed.

In subsequent sections, the harmonic balance approach will be applied to three test cases, namely a cylinder in the laminar flow regime, a 2-D airfoil cascade section of a modern compressor blade, and finally, a 3-D front stage compressor blade that encountered NSV in rig testing. Furthermore, two distinct conditions are investigated for each case. First, the natural shedding frequency is determined without motion. Next, we consider the enforced motion case in which the body (cylinder, airfoil, or blade) is forced to vibrate at prescribed frequencies other than its natural shedding frequency. The results will indicate the importance of both the natural shedding flow frequency and the frequency of the body's motion in NSV design analysis considerations.

Chapter 3

Flow Over Cylinder Without Motion

As an initial step towards better understanding of NSV in turbine engine configurations, it is advantageous to investigate the well-known two-dimensional shedding flow about a circular cylinder case that exhibits similar NSV features. The low Reynolds flow over a cylinder serves as a useful test case because a large amount of experimental and numerical data is available for comparison (see, for example, Roshko [38], Williamson [39] [40] [41], Sarpkaya [42], Tanida [43], Norberg [44] [45], and McMullen [21]). If a cylinder is placed in a low Reynolds number flow ($47 < \mathrm{Re} < 180$), vortices are shed alternately and two-dimensionally from the top and bottom of the cylinder. This shedding behavior is demonstrated in Figure 3.1 where the instantaneous total pressure contours are plotted for a Reynolds number (Re) of 100. The phenomenon is generally known as Von Karman vortex shedding. For Reynolds numbers greater than 180, the flow aft of the cylinder becomes three-dimensional. As a result, this preliminary study only considers flow in the Reynolds number range of $47 < \mathrm{Re} < 180$. Typical examples of this phenomenon include the vortex shedding flow over a car antenna, power lines, cables, smokestacks, or off-shore risers.

The shedding flow over a stationary cylinder is determined by a single parameter - Reynolds number. A relationship between Reynolds number and Strouhal number, the frequency of wake oscillation, is determined and compared with existing computational simulations [21] and experimental data [41]. The Reynolds number is given by:

$$Re = \frac{U_\infty D}{\nu_\infty} \tag{3.1}$$

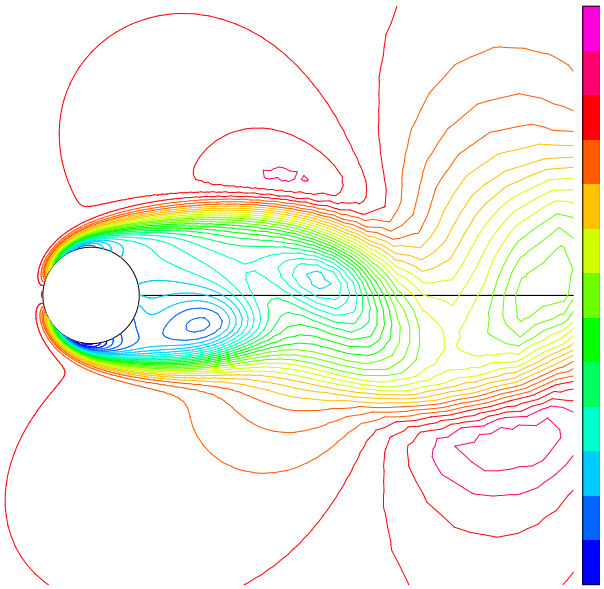

Figure 3.1: Instantaneous total pressure contours demonstrating the development of conventional Von Karman vortex streets in the laminar flow regime for Re = 100.

where U_∞ is the freestream velocity of the fluid, D is the characteristic dimension (i.e. diameter of the cylinder), and ν_∞ is the kinematic viscosity of the fluid.

Whether the flow is laminar or turbulent is primarily governed by the Reynolds number. This study is concerned with the laminar flow over a circular cylinder. The Strouhal number (St) is the non-dimensional vortex shedding frequency. It is

$$St = \frac{fD}{U_\infty} \tag{3.2}$$

where f is the dimensional frequency (cycles/time), D is the cylinder diameter, and U_∞ is the same as given above.

As the vortices are shed, periodic lift and drag forces are exerted on the cylinder. Lift is primarily due to variations in pressure on the cylinder's surface and is the integrated result of the pressure loading on the cylinder [44]. The lift coefficient is

defined as

$$C_L = \frac{L}{\frac{1}{2}\rho_\infty U_\infty^2 Ds} \tag{3.3}$$

where L is the amplitude of the lift fluctuations acting on a spanwise segment of length s exposed to the flow, ρ_∞ is the density of the fluid, U_∞ is the freestream velocity of the flow over the cylinder, and D is the diameter of the cylinder.

Based on experimental results and 2-D simulations, it can be seen that the amplitude of the lift coefficient increases rapidly within the laminar shedding regime from the onset of shedding at a Reynolds number of 47 (see Figure 3.6). The onset can be characterized as a supercritical Hopf bifurcation and is typically described by the Stuart-Landau equation [44]. The unsteady lift can be used to determine the transition from steady flow to Von Karman vortex shedding in the two-dimensional wake behind a circular cylinder in low Reynolds number flow. These forces will be calculated in this chapter and investigated using the HB method.

As described previously, the solution to the HB equations requires the user to input the frequency of the flow instability. Since the purpose of the study is to find the shedding frequency as one of the unknowns of the solution, both the frequency sweep method and phase error technique were applied to the stationary cylinder in cross flow. In the frequency sweep method, the solution residual of the HB equation is computed for each case. However, previous studies by McMullen, et al. [21] indicate the solution residual drops off sharply at the precise shedding frequency. As a result, this method of searching for the shedding frequency is inefficient and can easily miss the correct frequency.

The novel frequency search technique developed by Hall et al. [2] is also implemented. In this method, the phase difference between successive iterations of an unsteady integrated first harmonic quantity (such as unsteady lift, moment, etc.) is

calculated for a range of frequencies. When an incorrect frequency is input using the nonlinear harmonic balance method, a phase shift greater or less than zero is obtained. It becomes readily apparent that the phase is nearly linearly related to the assumed frequency. The precise shedding frequency is then determined as the frequency for which the phase shift is zero. Using simple interpolation, this frequency can be calculated with as few as two HB solutions.

In the upcoming sections, the two aforementioned frequency search methods are demonstrated for a stationary cylinder in cross flow. Furthermore, the unsteady lift and mean drag are calculated for the cylinder without motion. All of the results are compared with available computational and experimental data to validate the HB method as a viable technique for solving highly nonlinear shedding flows.

3.1 Stationary Cylinder in Cross Flow

A well-studied fluid dynamics phenomenon is a stationary cylindrical structure in cross flow. The flow over a stationary cylinder is modeled for various Reynolds numbers in an attempt to reproduce Williamson's [41] experimental data and compare with McMullen's [21] computational data. A typical mesh is shown in Figure 3.2 with 129 points in the circumferential direction and 65 points in the radial direction. The mesh boundary is 40 diameters from the center of the cylinder in this figure.

3.1.1 Demonstration of Two Frequency Search Techniques

Using the two frequency search methods described previously, Figure 3.3 and Figure 3.4 show the HB solution residuals and phase change in unsteady lift per iteration for a number of assumed Strouhal numbers at a Reynolds number of 170 when using two harmonics in the HB method. It is imperative to note the linearity between the change in phase and Strouhal number in Figure 3.4. This relationship makes interpolation

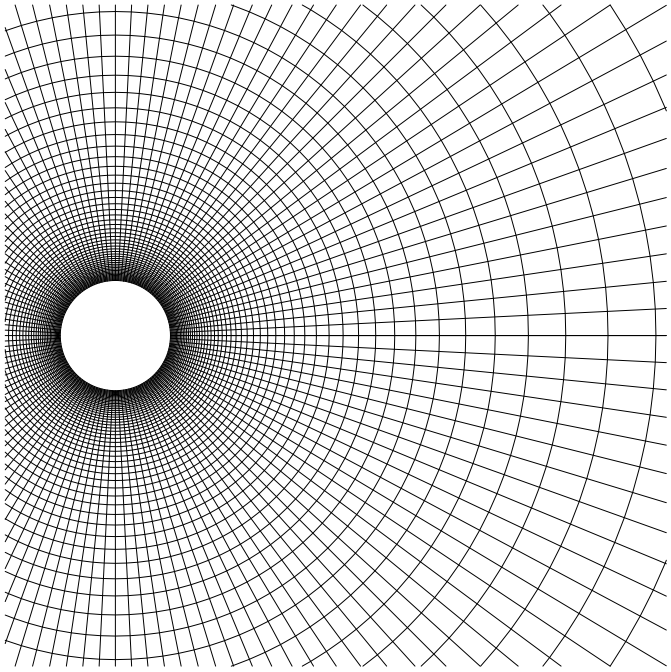

Figure 3.2: Computational grid (129x65 mesh) for cylinder in cross flow.

to the zero phase shift condition (and the predicted shedding frequency) a much simpler calculation and in fewer iterations than the residual sweep method. The solution residual is determined by computing the L_2 norm of the solution vector. As can be seen from the plots, the predicted Strouhal number is approximately 0.1865.

3.1.2 Strouhal - Reynolds Number Relationship

The frequency search procedure was repeated for a range of Reynolds numbers in the laminar flow regime, and a corresponding Strouhal number was determined for each Reynolds number. The resulting Strouhal numbers were then compared with experimental data [41] and numerical results [21] as shown in Figure 3.5. The HB method shows excellent agreement with the experimentally determined values and slightly better agreement than McMullen's [21] computational results.

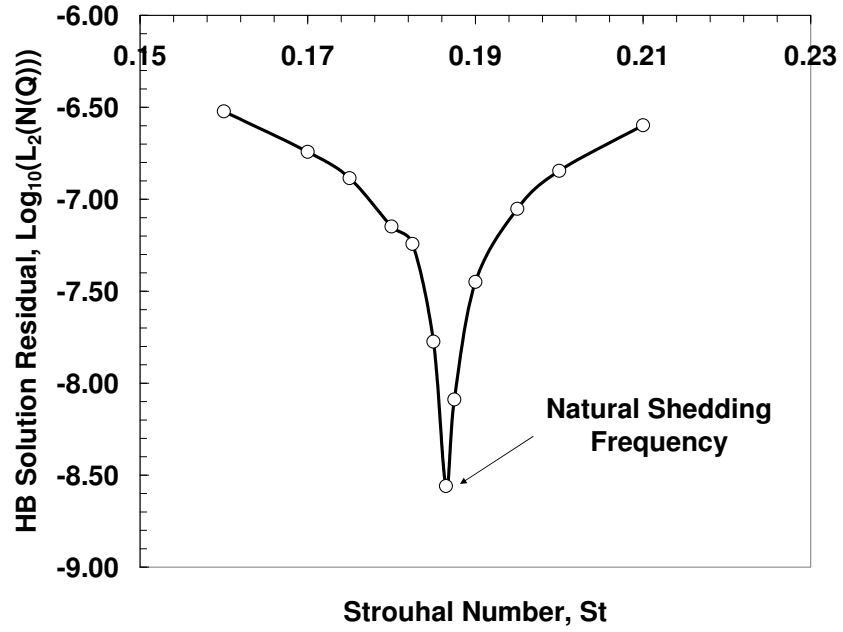

Figure 3.3: Frequency sweep method: HB solution residual as a function of Strouhal number for Re = 170 (2 harmonics).

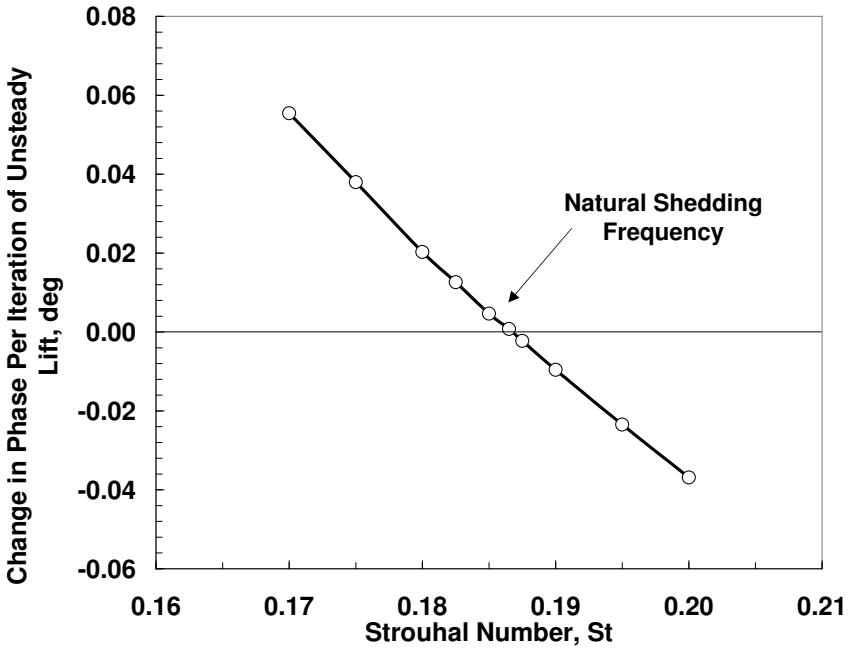

Figure 3.4: Phase error method: Change in phase angle of unsteady lift versus Strouhal number for Re = 170 (2 harmonics).

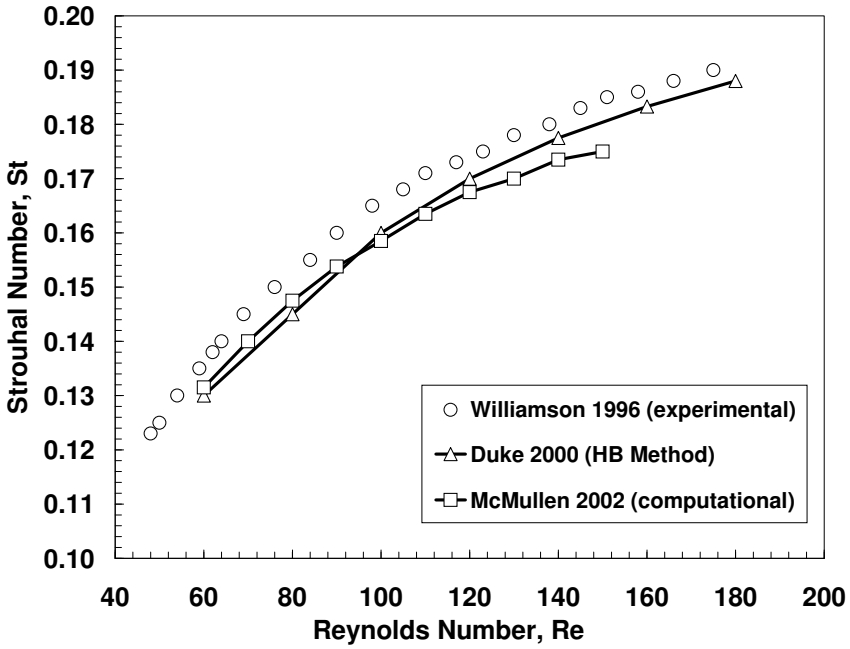

Figure 3.5: Cylinder in cross flow - Strouhal number dependency on Reynolds number.

3.2 Stationary Cylinder Unsteady Forces

In addition to determining the frequency of the fluid dynamic instability, the amplitude of the unsteady forces were calculated. At the shedding frequency for a range of Reynolds numbers, the amplitude of the first harmonic lift acting on the shedding cylinder is determined. Figure 3.6 shows the unsteady lift amplitude versus Reynolds number. By extrapolating to the Reynolds number of zero oscillating lift, the onset of the vortex shedding can be determined. This occurs at about a Reynolds number of 47, which is approximately the same value as determined from other nonlinear dynamic computational techniques [44].

To validate the results obtained by the HB method, a comparison was made with the experimental study of Tanida, et al. [43] as well as numerous 2-D numerical simulations. Figure 3.7 shows that the results obtained from the HB method show

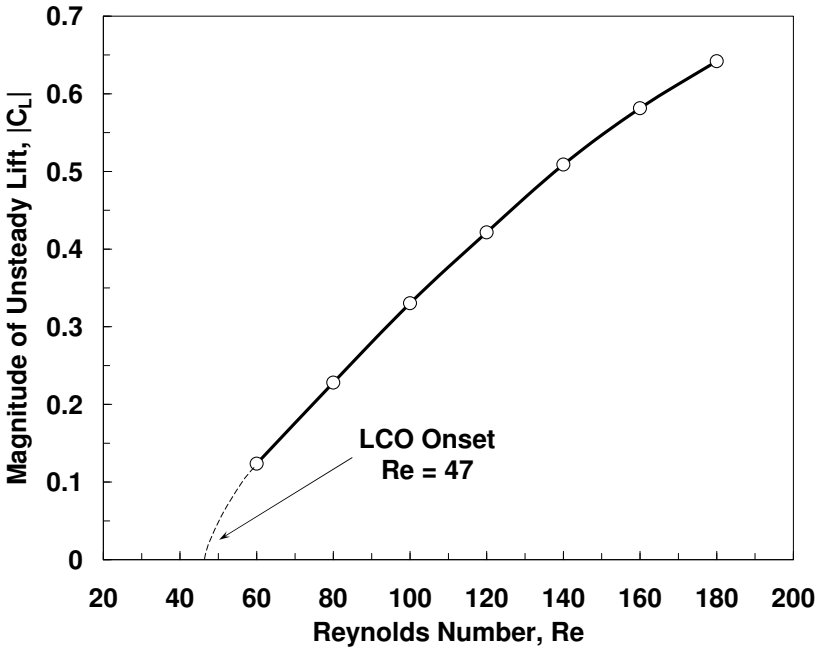

Figure 3.6: Computed amplitude of first harmonic of unsteady lift acting on shedding cylinder from onset at Re = 47.

reasonable agreement with the 2-D computational data but vary considerably from the experimental data. This discrepancy may be explained in part by the use of unsealed gaps in Tanida's towing tank study [44]. Tanida, et al. [43] utilized a force element method to measure the fluctuating lift in which the load-transmitting part of the cylinder is connected to a cantilever beam element that is fixed to a base inside a "dummy" part of the cylinder. Keefe [46] found that unsealed gaps can result in a drastic reduction in fluctuating unsteady lift forces as Reynolds number is decreased, as much as 10 times lower than with sealing [46]. However, his experiment was conducted at higher Reynolds numbers (Re = 3000 - 40,000) so it is difficult to determine a definitive reason for the incongruity between the experimental and computational data. Unfortunately, this is the only experimental data available in the Reynolds regime of interest so it is hard to make a qualitative comparison. When the HB method is compared with other numerical simulations, it results in slightly

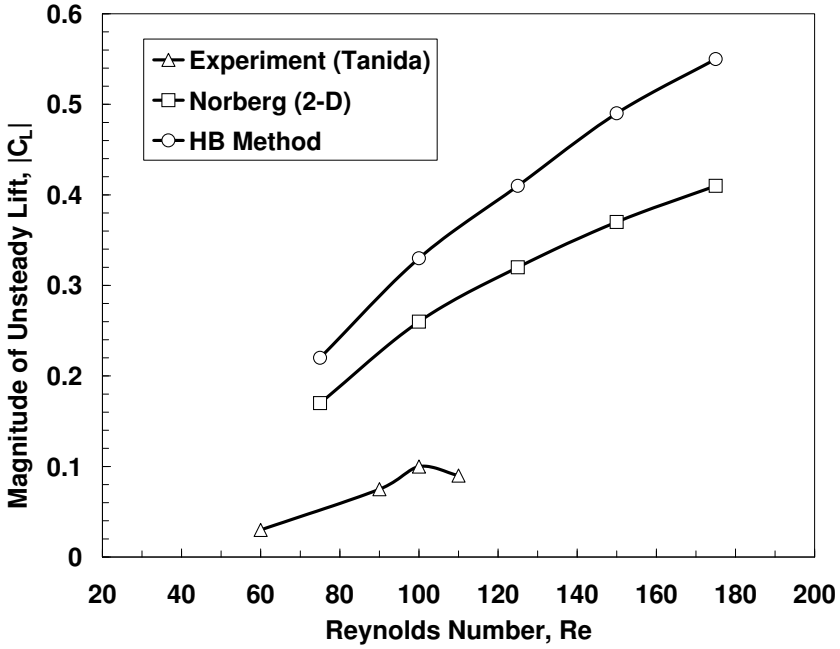

Figure 3.7: Comparison of lift data with other numerical results (Norberg) and experimental data (Tanida).

higher unsteady lift coefficients. As a result, further study is required to determine the validity of Tanida's experimental results.

3.2.1 Stationary Cylinder Mean Drag

Similarly, the dependency of cylinder drag on Reynolds number was examined. There are numerous contributions to the total drag on a cylinder, including the viscous drag coefficient and the pressure drag coefficient. Henderson computed these coefficients numerically using a highly accurate spectral element method based on 8th order polynomials [47]. Furthermore, McMullen [21] also computed the drag forces as a function of Reynolds number using a frequency domain technique. The change from a steady to an unsteady wake is marked by a gradual decrease in the viscous drag coefficient as well as the total drag throughout the laminar flow regime [47]. A plot comparing the values obtained by Henderson, McMullen, the harmonic balance

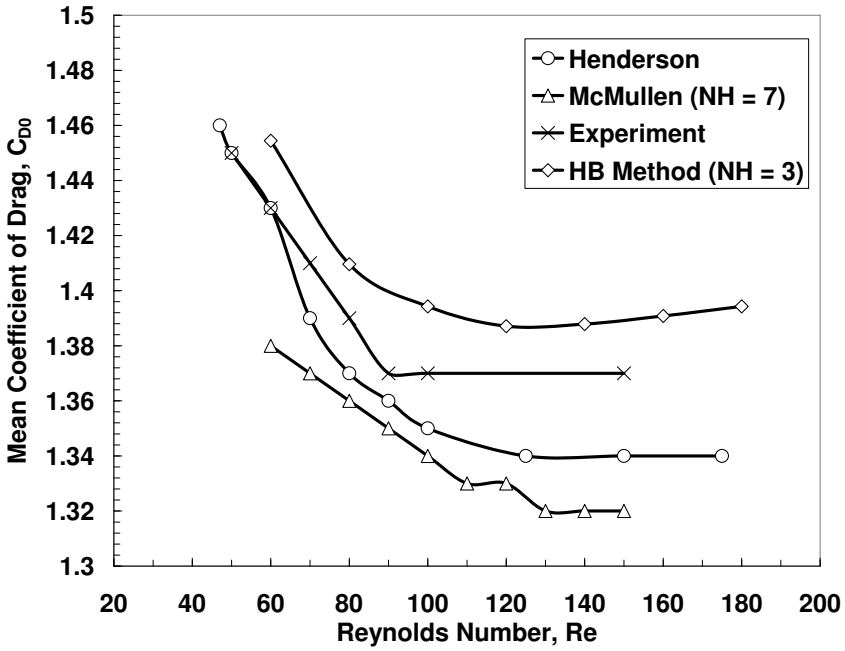

Figure 3.8: Comparison of mean coefficient of drag versus Reynolds number data for laminar vortex shedding.

method, and experiment is found in Figure 3.8. Again, the results show remarkable agreement with experiment and other computational techniques. It is noted that the mean drag coefficients are relatively constant with respect to Reynolds Number as compared to the unsteady lift coefficients. Therefore, the harmonic balance method is further validated as a valuable tool for predicting the forces on a cylinder.

3.3 Summary

In this chapter, the case without cylinder motion was considered. Results were presented for a stationary cylinder in cross flow in the low Reynolds number regime ($47 < \mathrm{Re} < 180$). This served as a useful test case for modeling NSV because it is a well-studied phenomenon and a significant amount of experimental data is available. The shedding frequencies were determined using a unique phase error method. This method utilizes the phase shift of an unsteady first harmonic quantity, such as the

unsteady lift on the cylinder. It was determined that the phase is nearly linearly dependent on Strouhal number and the shedding frequency is that for which the phase is identically zero. This method only required a few computations and saves considerable time and effort. Using the phase error method for a range of Reynolds numbers, a relationship between Reynolds number and Strouhal number was determined and compared with existing computational and experimental data. The HB results showed excellent agreement with Williamson's experimental data.

Both the oscillatory lift and the mean cylinder drag were also determined for the stationary cylinder case. A comparison of the unsteady lift data with the experimental data of Tanida showed relatively poor agreement but reasonable agreement was achieved when compared with other two-dimensional numerical simulations. However, it is speculated that this discrepancy is due to the use of unsealed gaps in the experiment, which can account for as much as a ten times reduction of the cylinder unsteady lift force. Furthermore, the mean coefficient drag results correlate very well with the experimental data. Hence, for a stationary cylinder in cross flow at low Reynolds numbers, the HB method accurately predicts both the natural shedding frequency and unsteady amplitude of vibration. However, these results are independent of the cylinder's motion. The next chapter will consider the case where the cylinder is forced to vibrate at prescribed frequencies other than its natural shedding frequency. The effect on the cylinder's unsteady forces, such as lift, will be investigated to determine at what frequency the maximum amplitude response is encountered.

Chapter 4

Cylinder Flow Vortex Shedding with Prescribed Motion

In the previous chapter, the vortex shedding behind a cylinder is investigated without consideration of the cylinder's motion. In this chapter, the cylinder is forced to oscillate normal to the flow direction at a specified amplitude and frequency. Over a range of forcing frequencies, the flow shedding frequency will "lock-in" to the frequency of the vibrating cylinder. This synchronization effect was first observed by Bishop and Hassan and later experimentally measured by Koopman at low Reynolds numbers [48]. Cylinder vibration with frequencies near the shedding frequency can influence both the pattern and the phasing of the vortices. Outside of this region, the cylinder will oscillate at one frequency and the vortices will shed at a frequency near that determined by the flow Strouhal number (see Figure 3.5). Koopman experimentally determined the lock-in region for Reynolds numbers of 100 and 200. Forced oscillations are achieved experimentally by using a shaking mechanism to generate a controlled motion at a range of amplitudes and frequencies.

As discussed in Chapter 1, the vortex lock-in phenomenon has been well-studied for cylinders by such researchers as Blevins [49], Williamson [40], Anagnostopoulos [50] [51], Sarpkaya [42], Tanida [43], Zdravkovich [52], Karniadakis and Triantafyllou [53], and Patnaik, et al [54]). A schematic of the lock-in region is shown in Figure 4.1 in which the amplitude of cylinder oscillation is plotted as a function of the forcing frequency, non-dimensionalized by the natural shedding frequency (without cylinder motion). For cylindrical structures, this region is roughly V-shaped and centered on the natural shedding frequency. As the driving frequency is varied, three

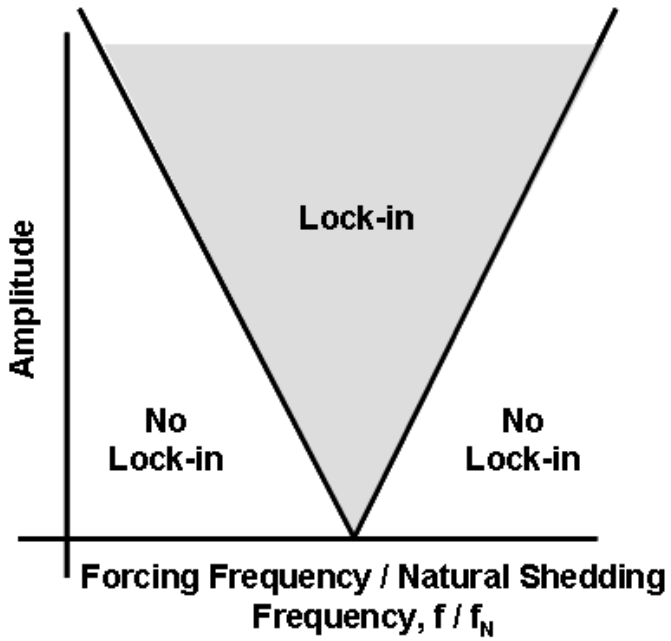

Figure 4.1: Schematic of the lock-in region for a cylinder oscillating over a range of prescribed frequencies and amplitudes.

distinct behaviors are observed, inside and outside of the so-called lock-in regime. Within the lock-in boundary, the vortices are shed at the forced frequency. Outside of this boundary, there is a region in which there is an interaction between the forced and natural frequencies, which leads to quasi-periodic and chaotic vortex shedding. Outside of this region, the wake oscillates at its natural shedding frequency and the cylinder is vibrating at a different frequency.

4.1 Study of Cylinder Lock-in Region

To investigate this phenomenon numerically, the same HB solution methodology was used as the stationary cylinder case but with the cylinder vibrating in the transverse direction at a prescribed frequency. In an attempt to replicate Koopman's data, the HB code was run at a Reynolds number of 120 and 150 with a fixed amplitude for many different Strouhal numbers, and the solution residual was noted for each case.

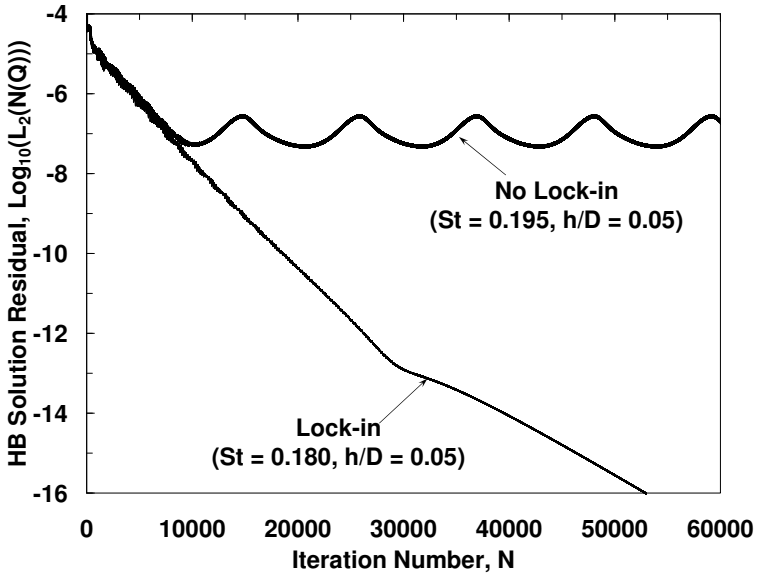

Figure 4.2: Solution residual behavior inside and outside of the lock-in region for determination of lock-in bounds.

Within the lock-in region, the solution residual converges to machine zero. Outside of this region, two distinct frequencies are observed experimentally; however the current HB method can only handle one frequency. Thus in the region where two frequencies are expected to be present, the current numerical method fails to converge. Figure 4.2 shows this behavior for two different Strouhal numbers, one inside and one outside of the lock-in region. As described previously, a multiple frequency method has been developed by Ekici et al.[22] but in application to NSV, it is not an efficient design method.

This procedure was repeated for various amplitudes and an estimate of the left and right bounds on the V-shaped lock-in region is determined based on the HB solution behavior. However, it is difficult to determine the exact left and right bounds of the lock-in region due to the inability of the HB method to accurately determine the frequencies outside of the lock-in region where the cylinder flow is shedding at a different frequency than the cylinder is oscillating. Furthermore, there is a quasi-

periodic and chaotic region where the cylinder can lock-in. Therefore, there is some subjectivity in assessing what constitutes a fully converged solution within the lock-in region.

Initially, a mesh size of 129x65 was used with a mesh boundary radius of forty diameters measured from the cylinder's center. A comparison between Koopman's reported data and the results obtained by the HB method is shown in Figure 4.3. The dimensionless amplitude is plotted versus the ratio of the frequency of the vibrating cylinder to the natural shedding frequency. The low amplitude (h/D $<$ 0.10) region is zoomed in Figure 4.4 and includes the HB results for Re = 100, 120, and 150 as well as Koopman's experimental values. There is good agreement up to an oscillation amplitude of approximately 0.05. However, above this amplitude, the HB solution begins to deviate from the experimental values. This discrepancy may be due to the use of a coarse mesh, a large mesh boundary, or the code's limitation of the use of only 3 harmonics. A number of improvements were made to achieve better agreement with Koopman's experimental data. In particular, three different mesh sizes and a larger mesh boundary were used as well as more harmonics. The effect of these parameters on the lock-in boundary will now be described.

4.1.1 Effect of Mesh Refinement

For Re = 100, the initial improvements involved utilization of finer meshes and a smaller mesh boundary. Both a 193x97 and a 257x129 mesh were considered as well as a mesh boundary of 20 times the diameter of the cylinder (20D) instead of 40D. Table 4.1 shows the results obtained from the mesh refinement study for a dimensionless amplitude of 0.10, where LB and RB refer to the left and right hand bounds of the lock-in region, respectively. As can be seen, the use of a finer mesh improves the results at an amplitude of 0.10 but there is still a significant difference

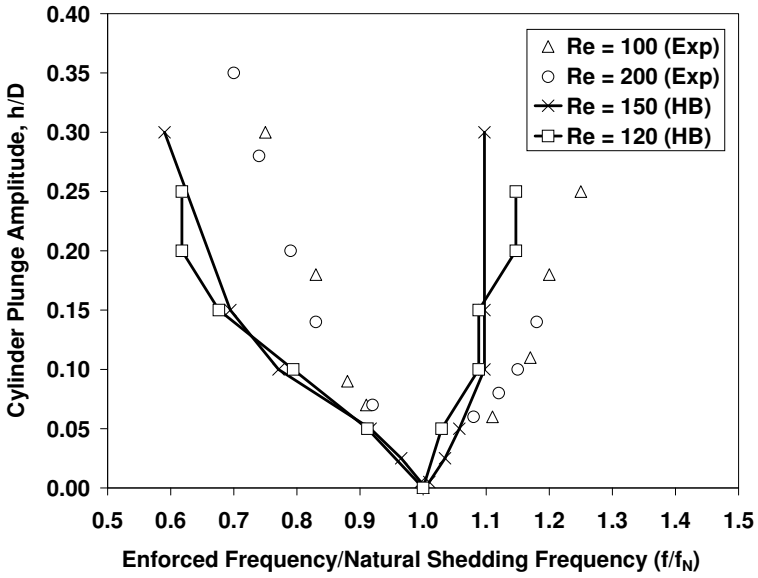

Figure 4.3: Comparison of lock-in region using HB method for Reynolds numbers of 120 and 150 with experimental results of Koopman.

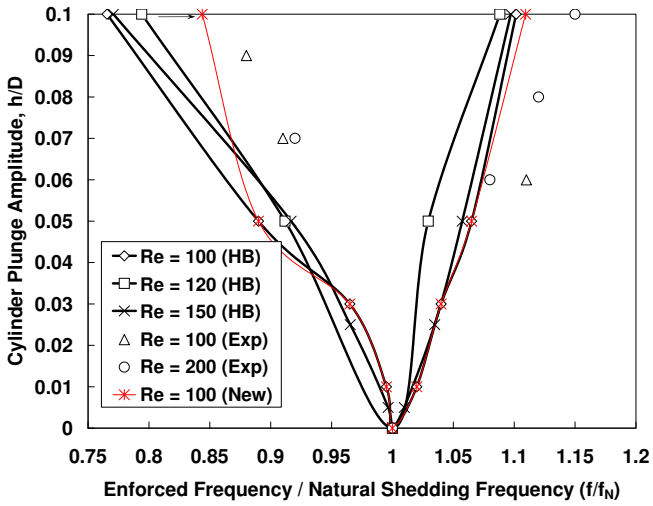

Figure 4.4: Zoomed in lock-in region for amplitudes up to h/D = 0.10 for Re = 100, 120, and 150 as well as Koopman's experimental results.

in the bounds of the lock-in region. Therefore, a further refinement is required to achieve better accuracy at higher vibratory amplitudes.

Mesh Size	Re	h/D	N_H	Radius	f/f_N (LB)	f/f_N (RB)
129x65	100	0.10	3	20	0.7656	1.1016
193x97	100	0.10	3	20	0.7656	1.1016
257x129	100	0.10	3	20	0.7891	1.1094
193x97	**100**	**0.10**	**7**	**20**	**0.8438**	**1.1094**
129x65	150	0.10	3	40	0.7708	1.0972
Experimental	100	0.10	-	-	0.875	1.1284

Table 4.1: Effect of mesh and harmonic refinement on modeling Koopman's experimental lock-in region for Re = 100.

4.1.2 Effect of Harmonic Refinement

Due to the constraints of using the HB method with a large grid domain, the original code limited the user to only three harmonics. In an attempt to avoid this problem, a filter was added to zero out the higher harmonics as you go farther and farther out in the domain, away from the cylinder where the wake effects are small. Therefore, it is possible to use as many as seven harmonics to achieve a more accurate solution. By examining Table 4.1, the results show that adding up to seven harmonics greatly improves the estimate of the left bound of the lock-in region and showed a slight improvement in the right bound. In addition, the results from the 193x97 mesh were added to Figure 4.4 to demonstrate the new bounds. The filter was a valuable tool because it gave a way to study the effect of adding more harmonics to the solution. It was found that the use of more harmonics resulted in a better approximation to Koopman's experimental results. However, mesh size had only a small effect on the bounds of the lock-in region. The improved results were also compared with other computational data and reasonable agreement was achieved with comparable time-marching and spectral element methods [54] [53].

4.2 Unsteady Forces for Prescribed Motion

The unsteady lift is also calculated for the prescribed motion case and as a verification, the results are compared with the experimental data of Tanida, et al. for a Reynolds number of 80 and a non-dimensional amplitude of h/D = 0.14 [43]. Tanida, et al. experimentally measured this quantity in a towing tank with 30 mm diameter test cylinders in which the lift and drag forces are sensed by strain gauges [43]. Oil was used as the fluid because it allows the unsteady forces on the oscillating cylinder to be measured with reasonable accuracy for such low Reynolds number flow [43]. Once again, the HB method was used at the same conditions and compared with the experimental data. A plot of the results can be found in Figure 4.5. The HB method shows remarkable agreement with the experimental results of Tanida, et al. Outside of the lock-in region, two frequencies are present, so the current HB method cannot be used to find the unsteady lift coefficient.

The stability of the cylinder oscillation is dependent on the component of the unsteady lift force that is in phase with the oscillating cylinder velocity [43]. The cylinder will be unstable if the imaginary part of the unsteady lift coefficient is greater than zero, which is equivalent to negative aerodynamic damping. Figure 4.5 shows the system is stable for St = 0.1000 to St = 0.1300 and then becomes unstable throughout the rest of the lock-in region. The stability of the system is determined by the imaginary part of the unsteady lift coefficient, C_L. A negative value of the imaginary part indicates a stable solution and a positive value gives an exponentially growing term which causes instability. A sensitivity study was conducted to determine the effect of including more and more harmonics. There does not appear to be a substantial benefit to keeping more than two harmonics in the HB solution for the parameter range studied herein.

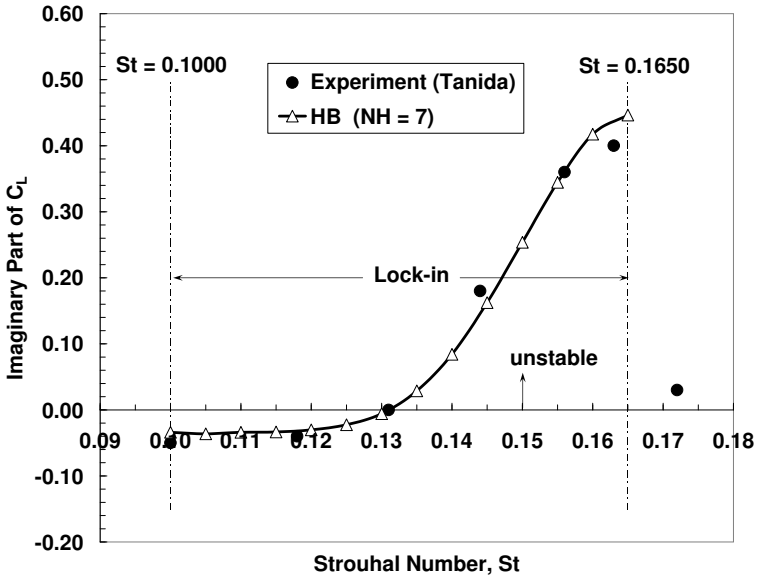

Figure 4.5: Magnitude of the imaginary part of the unsteady lift coefficient versus Strouhal number for a single cylinder oscillating transversely (Re = 80 and h/D = 0.14).

4.2.1 Amplitude of the Unsteady Lift

In addition, a plot of the amplitude of the unsteady lift coefficient was constructed as a function of the frequency within the lock-in region divided by the shedding frequency with no enforced motion. By examining the plot in Figure 4.6, the amplitude appears to steadily increase throughout the lock-in region until a peak displacement is reached. When compared with the stationary cylinder unsteady lift values, the unsteady lift coefficient monotonically decreases with enforced amplitude (see Figure 4.7). The lift coefficient decreases most significantly for lower Reynolds numbers.

4.2.2 Phase and Equivalent Aerodynamic Damping

Furthermore, the phase shift within the lock-in region is calculated as well as the equivalent linear aerodynamic damping from the fluid forces acting on the structure. The phase shift is a measure of the phase difference between the displacement of

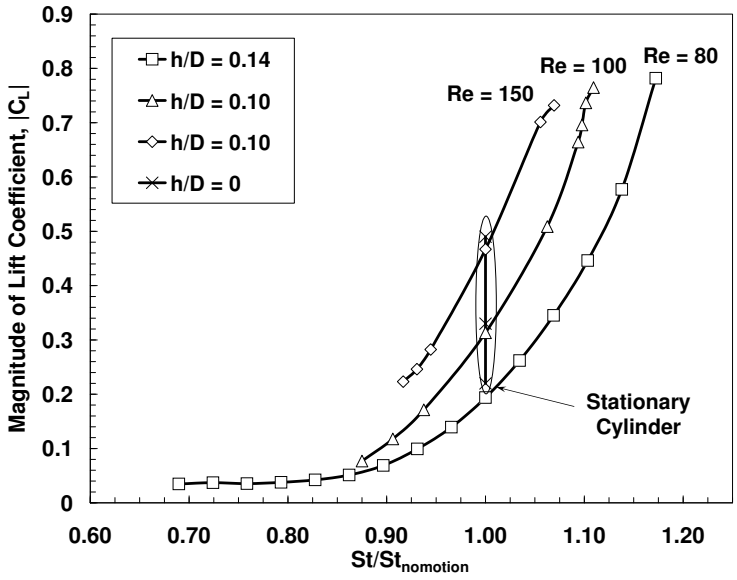

Figure 4.6: Amplitude of the unsteady lift coefficient as a function of the ratio of the Strouhal number (in the lock-in region) to the Strouhal frequency without motion.

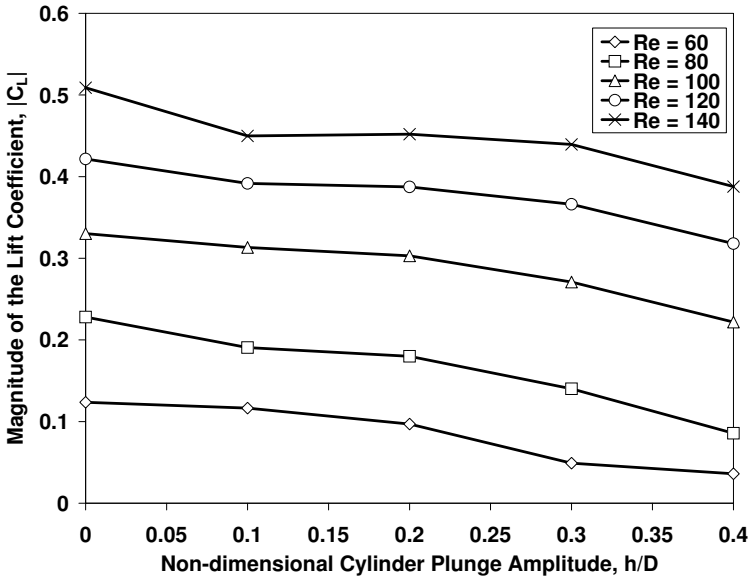

Figure 4.7: Effect of oscillation amplitude on the magnitude of the unsteady lift coefficient, $|C_L|$ for a range of Reynolds numbers.

the cylinder and the lift force. By examining Figure 4.8, the cylinder lift undergoes an abrupt 180 degrees phase shift between the shedding and the cylinder motion at about a Strouhal number of 0.1500. For a Reynolds number of about 80, the stationary cylinder shedding frequency was found to be St = 0.1450 using the HB method. Therefore, it appears that this 180 degrees phase shift occurs as the cylinder vibration frequency passes through the natural shedding frequency. This could be explained by Zdravkovich's [55] physical observation of the flow behind the cylinder. By examining the flow over an oscillating cylinder, it is noted that the vortices tend to shed when the cylinder is near its maximum displacement [49]. Zdravkovich found that for frequencies below the natural shedding frequency, the vortex is shed from the side opposite that experiencing its maximum displacement. However, for frequencies above the shedding frequency, the vortex is shed from the same side as the max displacement [55]. Therefore, the phase shift may be due in part to a switch in the timing of the shedding of the vortices. This appears to be consistent with flow animations generated for a frequency both below and above the natural shedding frequency. A phase shift of zero degrees refers to the condition for which the force and displacement are in-phase and no work is being done.

Also, Figure 4.9 shows that the equivalent linear damping becomes increasingly negative until it reaches a minimum value and then starts to increase again. A negative aerodynamic damping results in a net energy input to the cylinder vibration. The most unstable damping coefficient occurs at a Strouhal number of 0.1600 which coincides with the point for which maximum work is being done on the cylinder. Two enforced motion amplitudes are shown for comparison.

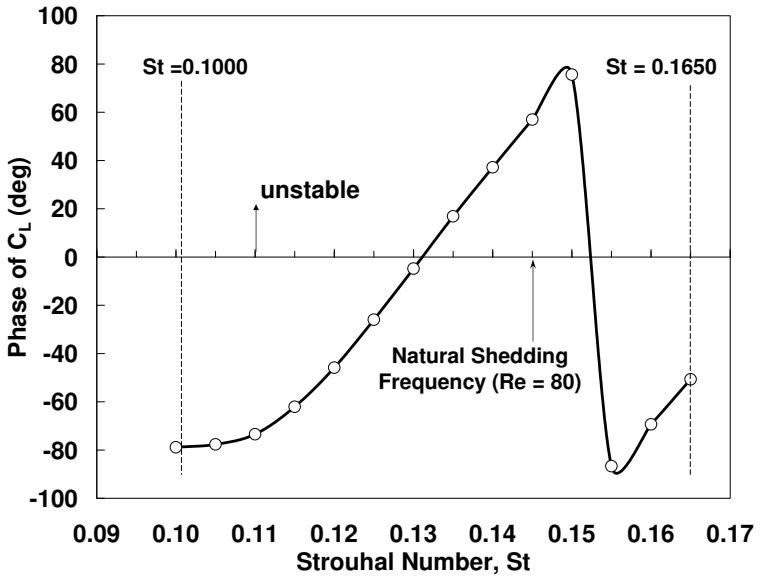

Figure 4.8: Phase difference between cylinder lift and displacement as a function of Strouhal number within the lock-in region for Re = 80 and h/D = 0.14.

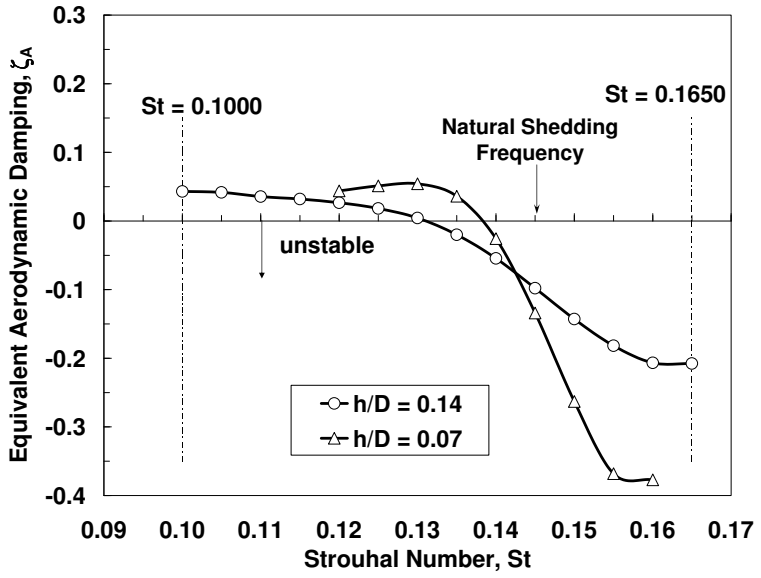

Figure 4.9: Equivalent aerodynamic damping in the lock-in region as a function of Strouhal number for Re = 80 and h/D = 0.07 and 0.14.

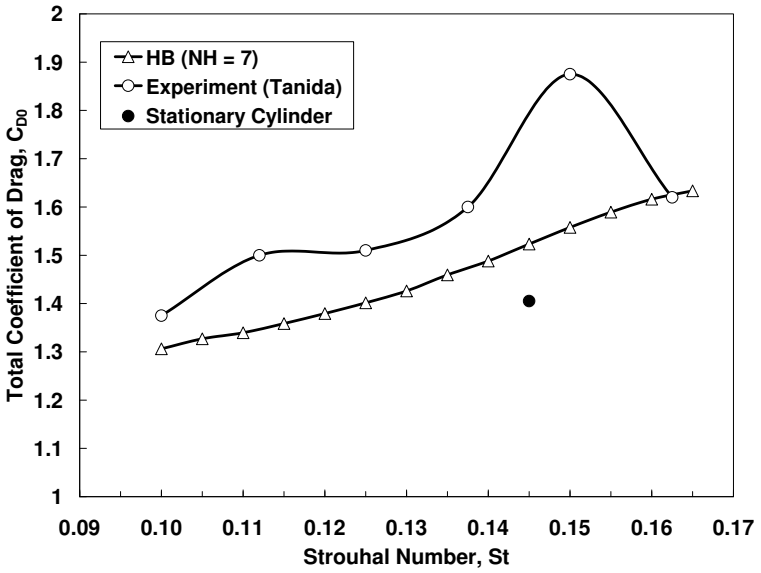

Figure 4.10: Comparison of the Mean Coefficient of Drag versus Strouhal Number Within the Lock-in Region with Tanida's experimental results for Re = 80 and h/D = 0.14.

4.3 Mean Drag for Prescribed Motion

In addition to the fluctuating lift forces on the cylinder, the mean drag was also calculated as a function of Strouhal number. Figure 4.10 shows the results obtained by the HB method as compared to the experimental results of Tanida. It can be seen that the drag coefficient steadily increases within the lock-in region until it reaches a maximum around $C_{D0} = 1.63$ at St = 0.1650 for the HB method. On the other hand, Tanida's results indicate a maximum value of $C_{D0} = 1.87$ at St = 0.1500. Overall, the HB method shows relatively good agreement with Tanida's experimental data [43]. At low Strouhal numbers, such as St = 0.1000, and higher Strouhal numbers like St = 0.1650, good agreement is achieved but there is poor agreement at St = 0.1500. The stationary drag coefficient was also compared to the enforced motion case at the same Strouhal number and the results indicate that cylinder motion slightly increases the drag coefficient.

4.4 Cylinder Mounted on a Spring

In addition, the fully coupled aerodynamics and structural dynamics (aeroelastic) system was considered. The response characteristics of a vortex-excited spring supported cylinder in the laminar flow regime are examined to compare with the prescribed motion results and existing experimental data. In this case, as the flow velocity is increased or decreased, the shedding frequency can approach the natural frequency of the structure. At a critical velocity, the shedding frequency will lock-in to the structure frequency [49]. In the lock-in region, resonant oscillation conditions can occur and produce large amplitude responses. Therefore, by determining the interaction between the flow oscillations and the cylinder motion, it will be possible to predict the cylinder oscillation frequency and the resultant cylinder amplitude.

4.4.1 Aeroelastic Cylinder Model

This cylinder aeroelastic "lock-in" problem [56] is modeled by a single degree of freedom spring-mass-damper system excited by a transverse lift force expressed as L', the lift per unit span. A schematic of this system can be seen in Figure 4.11. The cylinder is mounted on a linear spring of stiffness k and a structural damper with a coefficient of d. The external force on the cylinder is represented by the unsteady lift generated by the trailing vortices. The governing equation that describes this system is

$$m\frac{d^2h}{dt^2} + d\frac{dh}{dt} + kh = \frac{1}{2}\rho_\infty U_\infty DsC_{L'} \tag{4.1}$$

where m is the mass of the cylinder, d is the damping coefficient, k is the cylinder spring stiffness, ρ_∞ is the fluid density, U_∞ is the fluid velocity, D is the cylinder diameter, s is the cylinder span, $C_{L'}$ is the cylinder lift coefficient, and h is the transverse displacement of the cylinder.

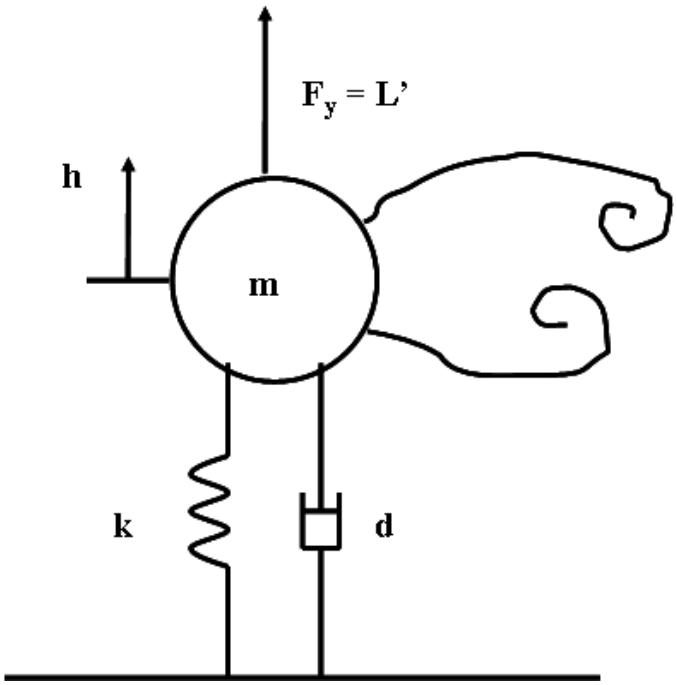

Figure 4.11: One degree of freedom model of a vortex-excited cylinder.

Next, one can assume simple harmonic motion so h and $C_{L'}$ can be represented as

$$h = h_1 e^{jwt}, \qquad C_{L'} = C_{L_1} e^{jwt} \tag{4.2}$$

As a result of this substitution, Equation 4.1 becomes

$$(-\omega^2 m + j\omega d + k)h_1 - \frac{1}{2}\rho_\infty U_\infty Ds C_{L'} = 0 \tag{4.3}$$

4.4.2 Non-Dimensionalization of Flow Parameters

In practice, it is more common to study the non-dimensionalized form of this equation because it reduces the number of parameters and also, makes it easier to compare with experimental results. As a result, some new dimensionless parameters should be introduced. The first parameter is the natural frequency of the system, which is

independent of any initial excitations. It is expressed as

$$\omega_0 = \sqrt{\frac{k}{m}} \tag{4.4}$$

Another parameter of interest related to the natural frequency is the damping factor. This value characterizes the energy dissipated by the cylinder as it vibrates. It is described by the following equation

$$\zeta = \frac{d}{2m\omega_0} \tag{4.5}$$

Another factor controlling the fluid-structure interaction is the mass ratio. It is the ratio of the mass of the cylinder to the mass of the fluid displaced by the cylinder. It provides a measure of the buoyancy effects and the inertia of the model as compared to the fluid [49]. It is given by

$$\mu_m = \frac{4m}{\pi\rho_\infty D^2 s} \tag{4.6}$$

It is also common to define a non-dimensional vertical displacement coordinate. Therefore, the plunge coordinate can be divided by a characteristic length such as the diameter of the cylinder. The new coordinate is defined as

$$h_1' = \frac{h_1}{D} \tag{4.7}$$

For convenience, a final parameter is introduced. It represents a ratio of the fluid frequency to the structural frequency and is given by

$$\kappa = \frac{2\pi\nu_\infty}{\omega_0 D^2} \tag{4.8}$$

Using all these dimensionless parameters, the governing equation can be greatly simplified. In general, the final equation can be written as

$$(-\kappa^2 Re^2 St^2 + 2j\kappa ReSt + 1)h_1' - \frac{\kappa^2 Re^2}{\mu_m \pi^3} C_{L'}(Re, St) = 0 \tag{4.9}$$

By separating this equation into its real and imaginary parts, a system of two equations is produced. Thomas, et al. initially demonstrated this method in 2002 [20]. These equations can be solved simultaneously for the two unknowns, Reynolds number and Strouhal number, for a specified h_1'. The nominal residual of the real and imaginary parts can then be written in the following form

$$R(L) = \begin{bmatrix} (-\kappa^2 Re^2 St^2 + 1)h_1' - \frac{\kappa^2 Re^2}{\mu_m \pi^3} Re[C_{L'}(Re, St)] \\ (2j\kappa ReSt)h_1' - \frac{\kappa^2 Re^2}{\mu_m \pi^3} Im[C_{L'}(Re, St)] \end{bmatrix} = 0 \tag{4.10}$$

where L is a vector of the unknown variables, Re and St.

4.4.3 Application of Newton-Raphson Technique

The Newton-Raphson technique is an efficient and stable way to quickly solve the system of equations given above [20]. This technique solves for the correct combination of Reynolds number and Strouhal number for which the residual goes to zero. The method requires the user to choose an initial value for Reynolds number and Strouhal number and then uses the HB solver to determine the real and imaginary parts of the unsteady lift coefficient. Next, the Reynolds number is perturbed by a small amount and the change in the forces with respect to Reynolds number is evaluated. The procedure is repeated for the Strouhal number. In vector notation, this procedure can be expressed as

$$\begin{bmatrix} \frac{\partial R(L)}{\partial L} \end{bmatrix} = \begin{bmatrix} \frac{\partial R}{\partial Re} & \frac{\partial R}{\partial St} \end{bmatrix} \tag{4.11}$$

where $\partial R/\partial Re$ and $\partial R/\partial St$ are given by the following relations

$$\frac{\partial R(L^n)}{\partial Re} \approx \frac{R(L^n, Re^n + \epsilon) - R(L^n, Re^n)}{\epsilon} \tag{4.12}$$

$$\frac{\partial R(L^n)}{\partial St} \approx \frac{R(L^n, St^n + \epsilon) - R(L^n, St^n)}{\epsilon} \tag{4.13}$$

for small values of ϵ. The resulting values can be put into matrix form and then the inverse is taken. This quantity is then multiplied by the original solution and subtracted from the initial guess of the Strouhal number and Reynolds number. Therefore, this is an iterative process and can be written as

$$L^{n+1} = L^n - \left[\frac{\partial R(L^n)}{\partial L}\right]^{-1} R(L^n) \tag{4.14}$$

This gives a new update for Re and St and the process is repeated until the solution converges. This technique is advantageous because it only requires a few iterations to achieve convergence.

4.4.4 Comparison of All Test Cases

By integrating the Newton-Raphson technique into the HB solver, a solution for the cylinder self-excited aeroelastic problem is obtained and the results are presented in Figure 4.13. For the prescribed motion case, the aeroelastic solution was used to cause the fluid natural frequency to lock-on to the non-linear flutter frequency. The HB method was applied for a range of aerodynamic conditions, or Reynolds numbers (Re), at their respective non-linear flutter frequencies. The total equivalent damping is then calculated at a range of amplitudes and the corresponding non-linear flutter frequency for each Re within the lock-in region. The total equivalent damping is the aerodynamic damping added to the structural damping. The aeroelastic lock-in amplitudes are determined by the zero crossings within the lock-in region as shown in Figure 4.12. It is important to note that for some Reynolds numbers, the lower amplitudes are not plotted since the natural fluid frequency is not locked-in to the cylinder vibration frequency for those cases. The LCO amplitudes are denoted by triangles in Figure 4.13.

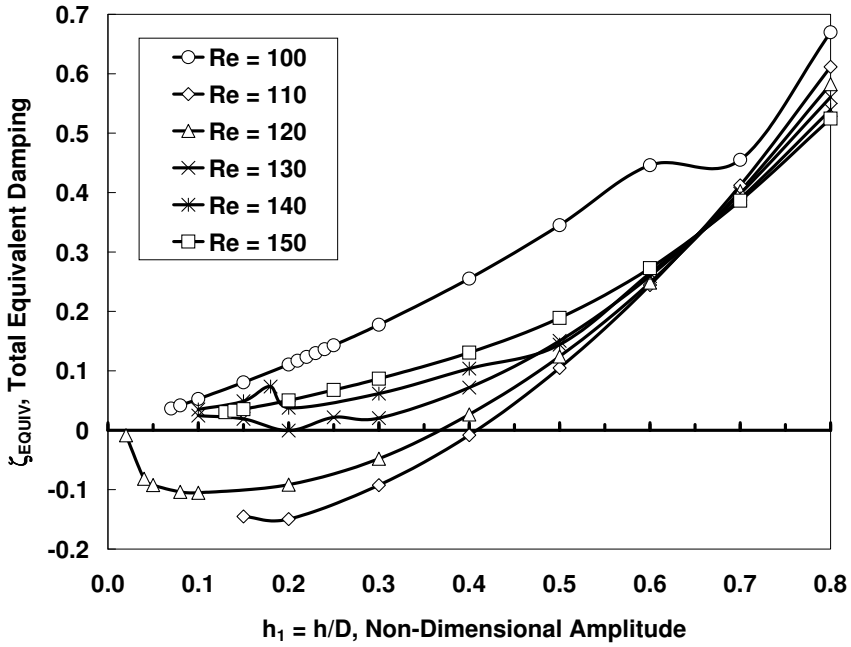

Figure 4.12: Total equivalent damping as a function of enforced amplitude, h/D, for a range of Reynolds number.

To validate these results, the solution was compared with those obtained experimentally by Anagnostopoulos and Bearman. They conducted their experiment in a water channel by mounting a 1.6 mm diameter circular cylinder on two steel springs on a horizontal shaft [50]. Using the experimental parameter values given for the natural frequency, the damping factor, and the mass ratio, a direct comparison can be made. Anagnostopoulos and Bearman examined Reynolds numbers in and out of the lock-in region. As predicted, they found that at a Reynolds number before lock-in, the vortices were shed at the Strouhal frequency but the cylinder was oscillating at a different frequency so two frequencies were present in the system [50]. However, when the Re was increased to 104, the cylinder oscillation frequency synchronized with the shedding frequency and the amplitude of the cylinder oscillations greatly increased. They found that the maximum oscillation amplitude occurred near the middle of the lock-in region [50]. When the Reynolds number was increased further to

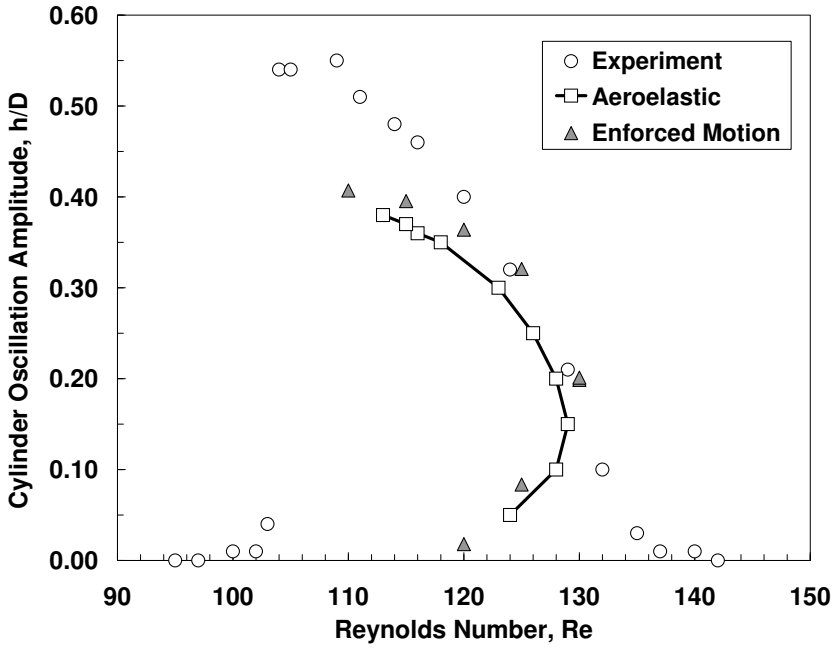

Figure 4.13: Comparison of enforced motion, aeroelastic, and experimental results for cylinder oscillation amplitude as a function of Reynolds number.

a value of about 126, the shedding becomes unlocked once again. Anagnostopoulos' results are compared with both the enforced motion results as well as the aeroelastic solution. The results in Figure 4.13 show that the HB method predicts the relationship between Reynolds number and Strouhal number fairly well within the lock-in region. Furthermore, they demonstrate the use of enforced motion to study NSV-like phenomena.

An interesting feature of this figure is the fact that there are two different amplitudes obtained for one Reynolds number, which is not possible to obtain experimentally. This may be explained by the fact that two solutions are present - a stable and an unstable one. Therefore, the experiment will not capture the unstable solution and will jump directly to the stable one.

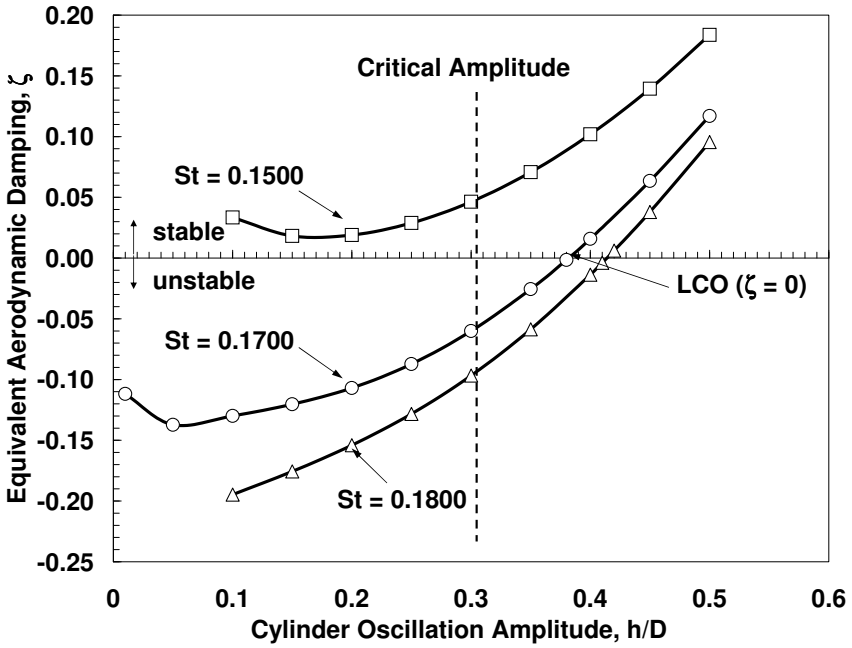

Figure 4.14: Total equivalent damping as a function of oscillation amplitude for Re = 120 and a number of Strouhal frequencies.

4.5 Demonstration of Enforced Motion Method

Finally, the enforced motion design method is demonstrated for the cylinder. For this case, the frequency is assumed to be the natural shedding frequency for a given aerodynamic condition, or Reynolds number (Re) of 120. The natural shedding frequency is St = 0.1700 as given by the Strouhal-Reynolds number relationship in Figure 3.5. An arbitrary maximum allowable amplitude of 30% of the cylinder's diameter, $h/D = 0.30$, is also chosen as shown in Figure 4.14. Furthermore, a cylinder frequency slightly above ($St = 0.1500$) and below ($St = 0.1800$) the natural shedding frequency are chosen. The total equivalent damping is then calculated at $h/D = 0.30$ for each frequency within the lock-in region.

As shown in Figure 4.14, the system would be stable for $St = 0.1500$ but unstable at $St = 0.1700$ and 0.1800. A negative damping value indicates that the limit cycle

oscillation (LCO) amplitude is greater than the critical amplitude so the design would not be acceptable at the natural shedding frequency of $St = 0.1700$. Furthermore, in accordance with the method for re-design, a range of enforced frequencies within the lock-in region can be studied to determine the maximum LCO amplitude as shown in Figure 4.15. For a given frequency, a range of enforced motion amplitudes can then be chosen to determine precisely where the system becomes unstable. Again, for some lower amplitudes, the total equivalent damping is not plotted because the shedding frequency has unlocked from the cylinder vibration frequency and there are two distinct frequencies in the system. As can be seen, the LCO amplitude is about 0.38 at the natural shedding frequency of $St = 0.1700$ and the maximum LCO amplitude is 0.41 at $St = 0.1800$. For design purposes, it would be advantageous to have a lower frequency to minimize the LCO amplitude. Therefore, the enforced motion design method shows promise as an effective design tool for NSV.

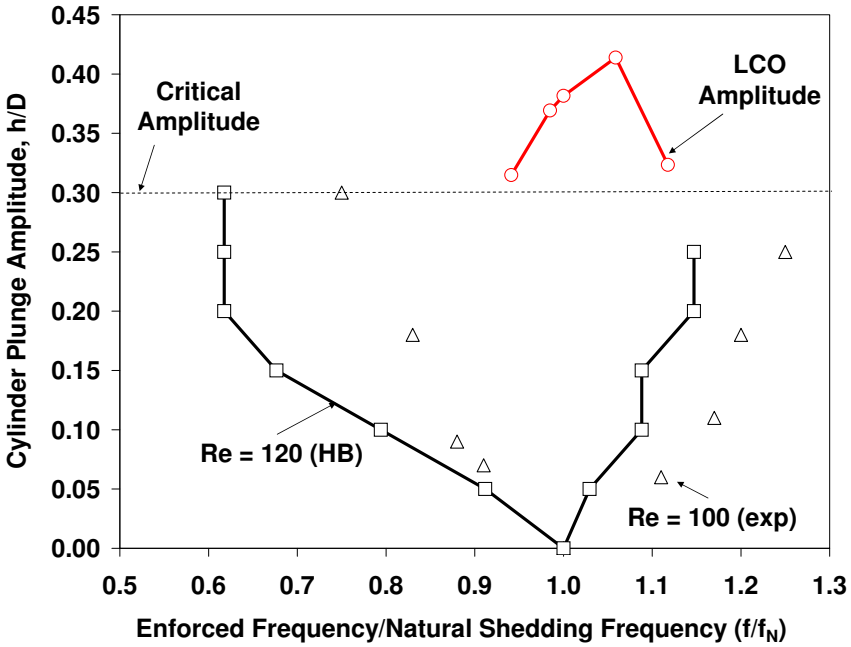

Figure 4.15: Cylinder re-design: LCO amplitude as a function of enforced frequency within the lock-in region.

4.6 Summary

In this chapter, the inclusion of cylinder motion was considered. The lock-in phenomenon was studied by forcing the cylinder to oscillate at prescribed frequencies and amplitudes. The vortex lock-in region has been well-studied for an oscillating cylinder and numerous experimental and computational data are available. The initial study showed reasonable agreement with Koopman's experimental data up to an oscillation amplitude of h/D = 0.05 but poor agreement at much higher amplitudes. As a result, a mesh refinement study was performed and the results showed somewhat better agreement but there was still a significant difference in the boundary region. To improve the results further, a filter was added to zero out the higher harmonics far away from the cylinder [57]. Preliminary results show that harmonic refinement provides better approximations to Koopman's experimental results.

Using prescribed motion, the amplitude, phase angle, and damping coefficient within the lock-in region were examined and various flow characteristics were deduced. Specifically, the stability of the flow, the frequency for which the maximum response occurs, and the behavior at the endpoints of the lock-in region were found and compared with the physics of the flow behind a cylinder. The imaginary part of the unsteady lift was calculated and compared with the experimental data of Tanida, et al. The harmonic balance method showed remarkable agreement with Tanida's results. In addition, the amplitude of the unsteady lift coefficient was calculated for a range of Reynolds numbers and amplitudes. It was concluded that cylinder motion caused a steady decrease in the lift coefficient. Furthermore, the phase shift and the aerodynamic damping coefficient were calculated. As in a linear vibration problem, the results indicated an abrupt 180 degree phase shift between the shedding force and the cylinder motion as the cylinder vibration frequency passes through the natural

shedding frequency.

A case study examined the response characteristics of a self-excited cylinder. This case differed from the previous one in the sense that the structural and fluid motions are coupled. The shedding frequency can lock in to the natural frequency of the structure as opposed to the prescribed vibratory cylinder frequency. The cylinder was mounted on linear springs and modeled as a single degree of freedom spring-mass-damper system. The Newton-Raphson technique is used to solve for the Strouhal number and Reynolds number for a prescribed amplitude. This technique is advantageous because it only requires a few iterations to achieve convergence. The solution was compared with the prescribed motion results as well as the experimental data of Anagnostopoulos and Bearman. Good agreement was achieved between all of the results.

Finally, the enforced motion design method was employed at a fixed aerodynamic condition, $Re = 120$, and an arbitrary amplitude of $h/D = 0.30$ for a couple frequencies, including the natural shedding frequency. It is noted that the LCO amplitude was slightly greater at a frequency greater than the natural shedding frequency. This is significant because it indicates that it is necessary to include the cylinder's motion to capture the maximum LCO response.

Therefore, the harmonic balance method has been established as a viable tool to solve NSV-like phenomena, such as the highly nonlinear unsteady shedding flow over a cylinder. In addition, the use of enforced motion and the lock-in phenomenon as a design tool has been validated for the cylinder. In subsequent chapters, the enforced motion method will be applied to the unsteady shedding flow about a 2-D airfoil cascade and finally, a full 3-D modern transonic compressor cascade.

Chapter 5

2-D Stationary Airfoil Cascade Natural Shedding (No Motion)

This chapter investigates a flow instability about a stationary two-dimensional airfoil cascade tip section of a modern front stage compressor blade operated at an off-design condition. For the rest of the chapter, "shedding" will be used as a generic term to describe the flow instability. In Chapter 3, the HB method was successfully demonstrated for a stationary circular cylinder in cross flow. The HB results showed good agreement with both experimental results and time domain CFD analysis.

5.1 Related Research

Vortex shedding aft of cylindrical structures has received considerable attention for many years for its application to power lines, cables, and off-shore risers. However, only recently has this phenomenon been studied for two-dimensional isolated airfoils as well as 2-D turbomachinery cascades. Lai and Platzer [58] experimentally studied a stationary NACA0012 airfoil in laminar flow and it was found to shed a typical von Karman vortex street, in which the upper row of vortices rotate clockwise and the lower row counterclockwise. At Re = 20,000, the stationary airfoil acts like a bluff body. The flow separates upstream of the trailing edge on both sides of the airfoil, creating the effect of a blunt body. Vortices are shed alternately from either side of the trailing edge in a manner analogous to the shedding behind a circular cylinder. In their latest study, Young and Lai analyzed the flow visualization results of Lai and Platzer by means of a 2-D compressible Navier-Stokes solver at Re = 20,000. They

found a natural reduced frequency of 9.4 and their results showed remarkably good agreement with experiment.

Jung and Park [59] also have experimentally investigated the frequency characteristics of von Karman vortex shedding in the near-wake of a single NACA0012 airfoil at low reduced frequencies through hot-wire measurements and a smoke-wire flow visualization. They studied the effect of angle of attack on the vortex shedding frequency. They made measurements of the wake for the case of a stationary airfoil at several angles of attack at a Reynolds number of 27,000 [59]. A typical vortex formation pattern was obtained, represented by a double row of vortices. For a stationary airfoil at a constant Reynolds number, the shedding frequency decreased with increasing angle of attack. The shedding frequency was found to be 153.6 $\pm$ 1.4 Hz and in terms of the Strouhal number based on airfoil thickness, was about 0.46 [59]. In a similar experiment, Bauer [60] and Huang and Lin [61] reported a Strouhal number of 0.43 and 0.47, respectively. The vortex shedding Strouhal number decreased from 0.47 to 0.30 as the angle of attack increased from 0 to 3 degrees [59]. It is noted that the sharp decrease in shedding frequency coincides with the region of rapid increase of the wake thickness.

Furthermore, Zhu and Kamemoto [62] have investigated the vortex shedding behind a thin, cambered blade used in axial flow pumps and the effect of angle of attack on an isolated blade. In the experiment, the flow around the fixed blade was visualized, and the dynamic torque acting on the blade (induced by the flow) was measured. Vortex shedding from the suction side was observed at angles of attack $\alpha \geq 10.7$ deg and from the pressure side at $\alpha \leq$ -1.3 deg [62]. No vortex shedding was observed either from the suction side or the pressure side of the blade at 1.7 deg $\leq \alpha \leq 7.7$ deg [62]. The vortex shedding frequency is expressed using the Strouhal number based on the chord. The measured frequency of the periodic vortex shedding yielded a

Strouhal number of 0.73 for α = -4.3 deg [62]. The vortex-shedding frequency and torque were determined for different angles of attack. The visualized flow patterns around the blade and FFT analysis of the measured torque acting on the blade were used to understand the mechanism of the induced vibration of the thin, cambered blade. The fluctuations in torque became significant at α = -4.3 degrees and 13.7 degrees [62]. They also examined this blade numerically using the vorticity-stream function equations with a fourth-order Runge-Kutta scheme [63]. Good agreement was achieved between the experiment and numerical simulations for both the vortex shedding frequency and torque.

A summary of the results for the isolated airfoils is presented in Table 5.1. As can be seen, the natural shedding Strouhal frequency varies somewhat with Reynolds number. The vast majority of the available literature is for a 2-D isolated airfoil or blade. To the author's knowledge, there is only one other researcher who has studied vortex shedding for a 2-D airfoil cascade.

Researcher	Re	St	Experiment	Numerical	Reference Quantity
Jung and Park	27000	0.46	X		thickness
Bauer	27000	0.43	X		thickness
Huang and Lin	27000	0.47	X		thickness
Zhu and Kamemoto	217000	0.75	X	X	chord

Table 5.1: Calculated Strouhal numbers for isolated airfoils at zero angle of attack and two different Reynolds numbers and based on both the airfoil thickness and chord length.

Gostelow et al. [64] experimentally studied a 2-D subsonic and transonic fixed blading turbine planar cascade with no oscillating force. The tested 2-D nozzle cascade had a chord of 175.3 mm with a turning angle of 76 deg and a design exit Mach number of 1.2 [64]. The blunt turbine blades had a circular trailing edge with a diameter of 6.35 mm [64]. They were primarily interested in the circumstances for which anomalous vortex shedding patterns are observed. In subsonic conditions,

the turbine nozzle cascade sheds wake vortices in a conventional Von Karman vortex street but under transonic conditions, a number of different shedding configurations in addition to the traditional von Karman vortex street were observed. For this case, the vortices are 2-D along the span except near the end walls where there is some interaction with the boundary layers. The transonic cascade schlieren photographs showed that the interaction between the base flow shear layers and the shock waves, which form at Mach numbers between 0.97 and 1.2, are the likely mechanism causing the changes in observed vortex-shedding patterns. In the transonic turbine cascade at $M > 1.0$, the Strouhal number was found to be 0.24 for the von Karman vortex street, based on the diameter of the nodal point formed by the confluence of the trailing edge shear layers and shock waves [64]. They also investigated the similarities of various vortex patterns behind oscillating bluff bodies and airfoils and blunt trailing-edge transonic turbine nozzle blades and found many patterns to fall into Williamson's [40] established shedding classification scheme.

Here, the no-motion case is considered for which the airfoil cascade is assumed to be stationary. According to the current industry analysis method, a time domain flow solver will provide the frequency of the instability, such as the shedding frequency. Here, the HB method is used to calculate the natural shedding frequency. This shedding frequency will then be compared with the blade mode natural frequency of interest, first torsion in this case. It is assumed that the highest amplitude response is achieved when the blade frequency is the same as the natural shedding frequency. In the next chapter, the case will be considered when the blade frequency is at a frequency other than the natural shedding frequency.

5.2 Direct Frequency Search Without Motion

To achieve vortex shedding, the analysis was run at an off-design condition and the 2-D section was taken near the tip, approximately 90 percent span. A single blade passage was modeled using an H-O-H grid with 17x33 nodes in the H-grid sections and 193x33 nodes in the O-grid section as shown in Figure 5.1. The grid has been distorted for proprietary reasons. At this spanwise location near the tip, the inflow relative Mach number M is 0.73 and the inlet Reynolds number is approximately 750,000. This particular engine configuration consists of 35 blades. Consequently, the shedding frequency is determined for a range of interblade phase angles.

5.2.1 Steady Flow Analysis

First, a "steady" flow solution was obtained. The solution residual does not approach zero but rather, it oscillates as shown in Figure 5.2(a). This oscillation is an indication of an underlying physical flow instability such as dynamic flow separation, vortex shedding, or a tip instability. However, because the steady flow solver uses local time stepping and multi-grid acceleration, one cannot infer the shedding frequency of the instability from this calculation. The "steady" Mach number contours (see Figure 5.2(b)) show the flow beginning to separate from the leading edge (LE) and suggest the existence of a flow instability.

5.2.2 Non-linear Harmonic Balance Analysis

Next, the nonlinear, unsteady harmonic balance solver was used to compute the shedding frequency for a range of interblade phase angles. As described previously, the procedure is to search for the shedding frequency that allows the harmonic balance flow solver to converge to a zero residual. Figure 5.3(a) shows the solution residual of

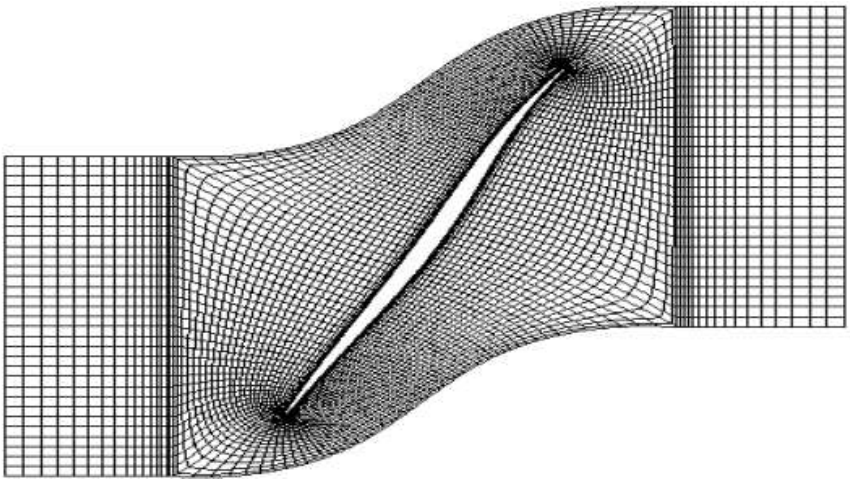

Figure 5.1: Computational grid for 2-D airfoil section of front stage modern compressor rotor blade (distorted view).

the harmonic balance solver as a function of shedding frequency for the zero interblade phase angle case. Note that at a Strouhal number of about 0.245 (based on the airfoil chord), the residual drops dramatically to zero, indicating that this is the shedding frequency of the flow instability. Note the very narrow trough in the residual curve in Figure 5.3(a), complicating the search for the correct frequency. The results shown are obtained when retaining five harmonics in the HB solution. An alternative procedure is to search for the frequency that produces a constant phase in a global quantity such as the first harmonic of the lift using the same method as described previously. Figure 5.3(b) shows the phase change in lift per iteration of the harmonic balance flow solver when the convergence reaches a steady state. In this case, the phase change is nearly linear with frequency. This makes interpolation to the correct shedding frequency a simple matter, and requires fewer calculations. This process may be repeated for other IBPAs as shown in Figure 5.4(a) and Figure 5.4(b) shows the natural shedding frequency as a function of interblade phase angle. It is important to note that a distinct natural shedding frequency was not obtained for all the IBPAs. At those IBPAs not plotted, the cascade was either not shedding or numerical stability

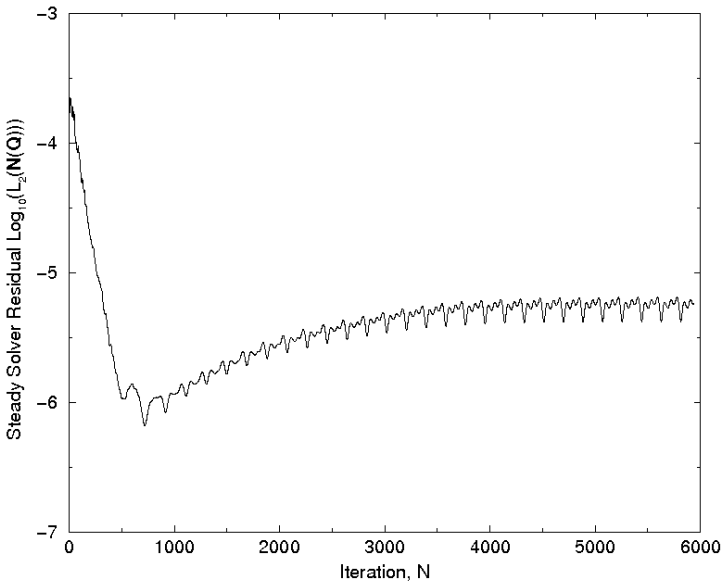

(a) Convergence History

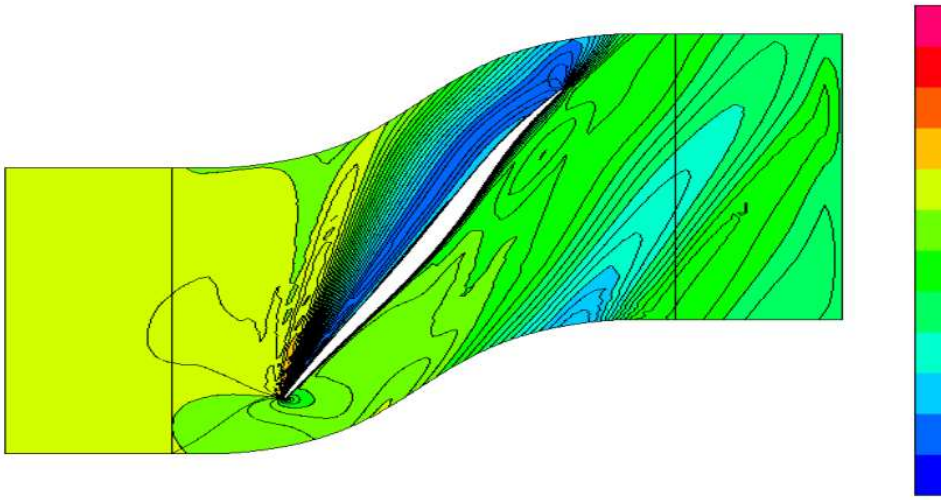

(b) Mach Contours

Figure 5.2: Convergence history and Mach number contours of steady flow computation for 2-D transonic flow about front stage modern compressor blade.

problems were encountered. The development of the flow instability is shown in Figure 5.5 where the total pressure contours are plotted at the natural shedding frequency of St = 0.245 for IBPA = 0 with 5 harmonics in the HB solution.

5.2.3 Comparison with Time Domain Results

Since experimental data is not available for comparison for this case, a time domain version of the flow solver was also generated by Jeffrey Thomas for an IBPA = 0 and the unsteady normal force on the blade was determined as a function of time [2]. A Fourier analysis of the unsteady normal force was conducted to determine the frequency content and compared with the HB results as shown in Figure 5.6. Excellent agreement is achieved between the FFT'ed time domain results and the HB method frequencies. The amplitudes of the first five harmonics were calculated and found to be 0.0185, 0.00325, 0.00125, 0.0011, and 0.001. By comparing these values to those obtained in Figure 5.6, it appears that the HB method over predicts the amplitude of the first harmonic force coefficient and under predicts the second harmonic. The higher harmonic amplitudes show good agreement. This discrepancy may be attributed to the FFT resolution of the time domain solution. Furthermore, the amplitudes of the harmonics can increase or decrease as the number of harmonics included in the solution changes. Therefore, the HB method is very effective for determining the frequency of the vortex shedding but does not predict the amplitude as well. However, the primary objective of the direct search method is to determine the frequency. Since amplitude is only a secondary concern, it was determined that these results were sufficient.

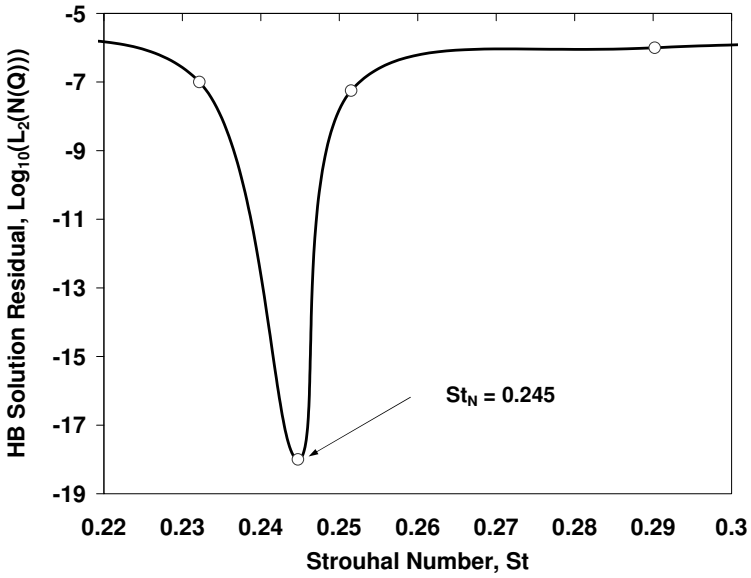

(a) HB Solution Residual

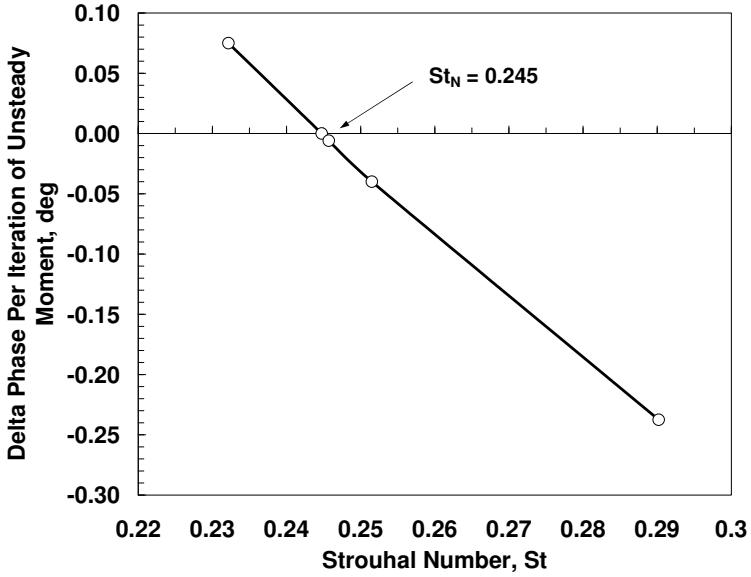

(b) Phase Error Method

Figure 5.3: Demonstration of two different frequency search techniques (for 2-D airfoil section of compressor blade) retaining five harmonics for IBPA = 0.

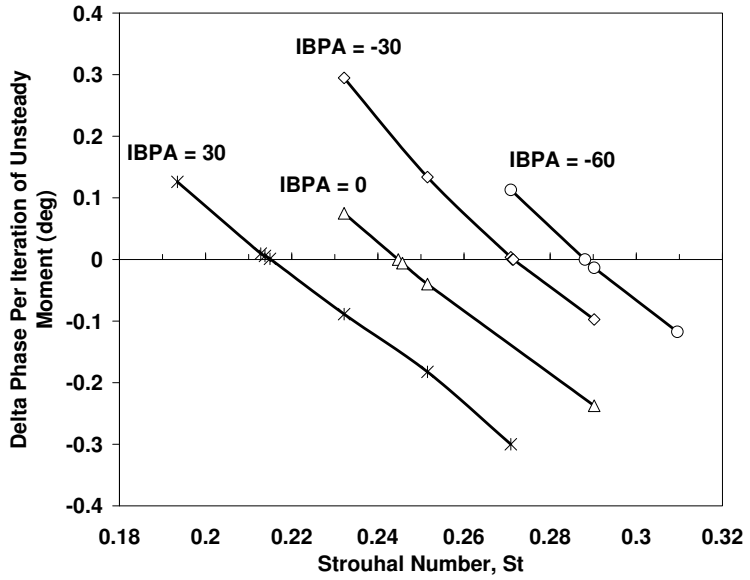

(a) Phase Error Method for Multiple IBPAs

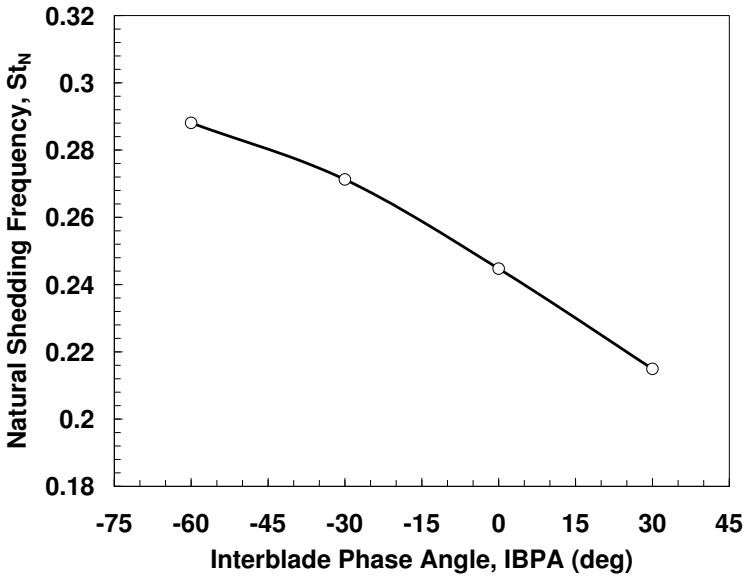

(b) Natural Shedding Frequency vs. IPBA

Figure 5.4: Determination of unique shedding frequency for each IBPA.

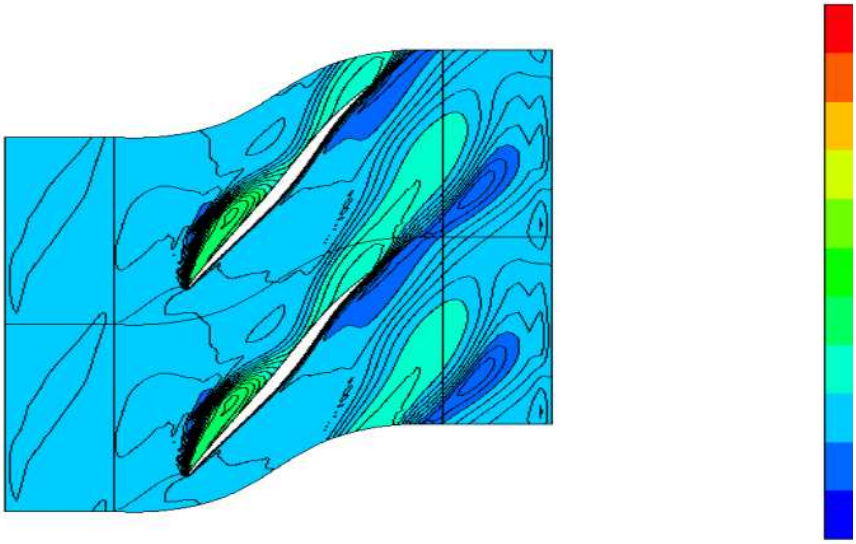

Figure 5.5: 2-D cascade total pressure contours at natural shedding frequency of 1265 Hz (St = 0.245) for an IBPA = 0.

5.3 Summary

This chapter demonstrates the traditional design approach in which the motion of the airfoil was not considered. The direct frequency search method was applied to determine the frequency of a flow instability about a 2-D airfoil tip section of an actual modern compressor cascade that experienced NSV. The stationary natural shedding frequency for a number of IBPAs was obtained using a unique phase error method. Furthermore, results for an IBPA = 0 were compared with time domain computations and excellent agreement was achieved in frequency but the HB method tends to over predict the amplitude of the first harmonic force coefficient and under predict that of the second harmonic.

It is also important to compare with other 2-D airfoil cascade studies. Gostelow experimentally investigated vortex shedding about a transonic planar blunt trailing edge turbine cascade as discussed in Section 5.1. The natural shedding frequency

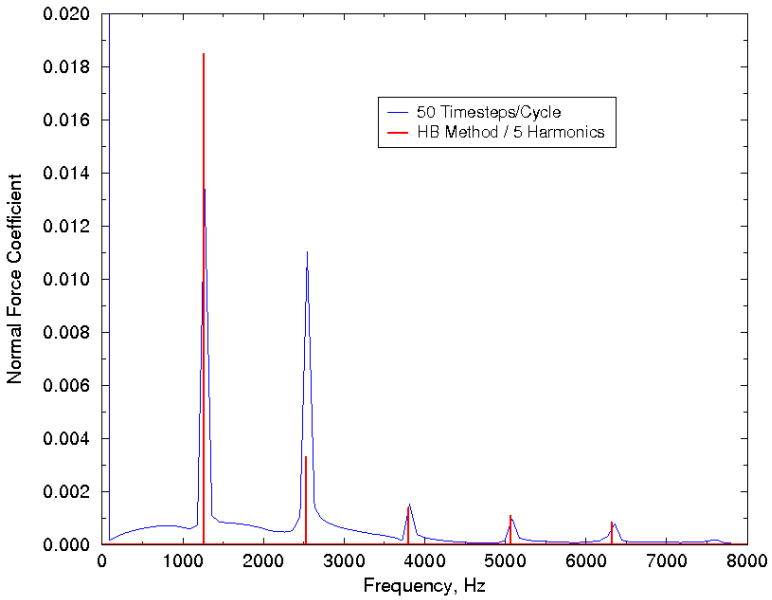

Figure 5.6: Comparison of FFT'ed Time Domain Results with the Harmonic Balance Method [2].

was determined to be St = 0.24. This is very close to the natural frequencies obtained here. For the IBPAs studied, the Strouhal numbers ranged from 0.21 - 0.29. In particular, a Strouhal number of 0.245 was found for the zero interblade phase angle case. Therefore, the HB direct frequency search method appears to accurately determine the natural shedding frequency.

However, the main purpose of this dissertation is to investigate the importance of including the motion of the blade in NSV design analysis. Hence, in the next chapter, the airfoil compressor cascade will be forced to undergo a pitching motion about midchord at prescribed amplitudes and frequencies. Using the knowledge of the stationary natural shedding frequency, the lock-in phenomenon will be investigated for different IBPAs as it was for the 2-D circular cylinder. Then, the LCO amplitudes for different frequencies will be calculated to determine the frequency for which the maximum response occurs. In addition, the enforced motion design method will be demonstrated.

Chapter 6

Enforced Motion of 2-D Airfoil Cascade at Prescribed Frequencies

In Chapter 5, the natural shedding frequency was determined without blade motion for a range of interblade phase angles. Generally, it is assumed that the highest response is achieved when the blade frequency is the same as the natural shedding frequency. Here, the enforced motion case is considered in which the airfoil cascade is forced to vibrate at prescribed frequencies other than its natural shedding frequency. The enforced motion design method will be demonstrated for the airfoils vibrating harmonically in pitch about midchord. A study of the cascade lock-in effect is performed for two interblade phase angles, namely IBPA = -60 and 0 degrees. An IBPA of -60 degrees is chosen because it is the least stable case and the IBPA = 0 case is considered for comparison. In Chapter 4, the lock-in phenomenon was successfully demonstrated for a 2-D circular cylinder undergoing plunging motion and the HB method showed good agreement with both experimental results and time domain CFD analyses.

The purpose of this chapter is to investigate the effect of including airfoil motion on the maximum LCO response. For the forced frequencies that are locked-in, the LCO amplitudes are determined and compared with the no-motion case at the natural shedding frequency. These results will indicate how both the natural shedding frequency and the blade natural frequency should be considered for NSV design analysis.

6.1 Related Research

A number of other researchers have investigated the forced oscillations of airfoils and the lock-in effect in recent years. The flow field near airfoils undergoing a pitching motion has been extensively investigated for rotorcraft applications. Furthermore, plunging airfoil flow characteristics at low frequencies and Reynolds number have been studied for their application to micro air vehicles. A lock-in region for both cases is observed and various parameters are investigated such as angle of attack, the generated unsteady forces, and phase difference between the displacement and these forces.

Recently, Young and Lai [65] numerically investigated the flow over a plunging NACA0012 airfoil for high reduced frequencies and small amplitudes ($h/c < 0.1$) to study the lock-in effect. Unusual vortex shedding modes in which multiple vortices are shed per half cycle are captured numerically and agree well with the experimental results of Lai and Platzer [58]. Furthermore, a vortex lock-in region is observed but the boundary is not symmetric about the shedding frequency. They speculate that this is due to the sharp trailing edge which forces the flow to separate on one side of the airfoil for most of the plunge cycle at higher frequencies and amplitudes.

Jung and Park [59] also looked at airfoil flow instabilities, except at low frequencies and low Reynolds number for the study of micro air and underwater vehicles. In particular, an experimental investigation of the vortex shedding characteristics in the near wake of an oscillating airfoil was carried out. In this study, the airfoil was given a harmonic pitching motion about the quarter-chord axis at four reduced frequencies: 0.1, 0.2, 0.3, and 0.4. To analyze the frequency characteristics of the vortex shedding, a short-time spectrum by the autoregressive (AR) method and a moving window were both used [59]. The wake vortex patterns exemplified the classical von Karman

vortex shedding. It was also found that the shedding frequency in the wake of the oscillating airfoil was much different from that for the case of the stationary airfoil at a given angle of attack as discussed in Chapter 5. They determined that the state of the boundary layer dictated the vortex shedding characteristics. In particular, the oscillatory motion of the airfoil made the boundary layer remain attached for a much wider range of angles of attack as compared with the stationary airfoil [59]. Furthermore, the range of variation of the shedding frequency diminished as the reduced frequency of oscillation increased.

Finally, Zhu and Kamemoto [62] also investigated vortex shedding from turbomachinery blades and the static blade case was discussed in Chapter 5. As stated previously, they were primarily interested in whether vortex shedding would induce self-oscillation of the blade. In order to accomplish this task, they determined the synchronization region, or lock-in boundaries for a pitching blade by forcing it to oscillate with a stepping motor. To determine whether the vortex shedding synchronizes with the pitching motion, the flow pattern around the pitching blade was viewed and the torque acting on the blade was measured [62]. Moreover, the phase differences between the blades oscillating displacement and the torque to oscillate the blade were calculated. These phase differences were then used to infer the likelihood of self-oscillation of the blade.

The frequency of oscillation was varied from St = 0.02 to 0.97. The vortex shedding frequency for the fixed blade is St = 0.66, 0.73, 0.83, and 0.90 for angles of attack of α = -8.3 deg, -4.3 deg, -1.3 deg, and 1.7 deg, respectively [62]. Both small oscillation amplitudes (1.0 deg, 1.5 deg, 2.0 deg, and 3.0 deg) and large oscillation amplitudes (10 deg, 15 deg and 20 deg) were used in the oscillation experiments. The lock-in boundaries are determined for two different angles of attack, namely α = -8.3 deg and -4.3 deg. Within the lock-in region, the natural shedding frequency is coin-

cident with the blade frequency. The lock-in boundary for this case is symmetric and up to an amplitude of 1.5 degrees, its width is approximately ±15% of the natural shedding frequency.

6.2 Demonstration of Enforced Motion Method

Here, the enforced motion design method is demonstrated for the tip section of a modern compressor blade cascade, operating at an off-design condition to achieve a fluid instability. For this case, the blade frequency is assumed to be the natural shedding frequency for zero interblade phase angle, or 1265 Hz, and an arbitrary critical 1T pitch amplitude of $\beta = 0.75$ degrees is chosen. The nonlinear HB method was conducted at this 1T amplitude and an assumed blade frequency of 1265 Hz for a range of IBPAs as shown in Figure 6.1. For the locked-in frequencies and amplitudes, the negative of the imaginary part of the unsteady moment coefficient, which is proportional to damping, is calculated. Without considering structural damping, the rotor is stable only if the negative of the imaginary part of the unsteady moment coefficient is positive for all IBPAs. The amplitude for which the unsteady moment coefficient goes to zero is the LCO amplitude. At this amplitude and frequency, the blade will vibrate in a stable limit cycle. In addition, it is possible to get unstable solutions but similar to the cylinder, the airfoil will experimentally jump to the stable one.

As can be seen in Figure 6.1, the system is unstable at an IBPA = -60 degrees for a critical 1T amplitude of 0.75 degrees so the design is deemed unacceptable. However, other amplitudes are also shown and it is noted that the blades would be stable and not encounter NSV for a pitch amplitude of 1.5 degrees. It is also important to note that for those cases in which the IBPA is not locked-in, the stability cannot be determined using the standard HB technique because there are two dis-

tinct frequencies present, the blade frequency and the natural shedding frequency. However, the response outside of the lock-in region is considered low amplitude and off-resonant. Also, Figure 6.1 shows that the stability tends to increase monotonically with enforced pitch amplitude.

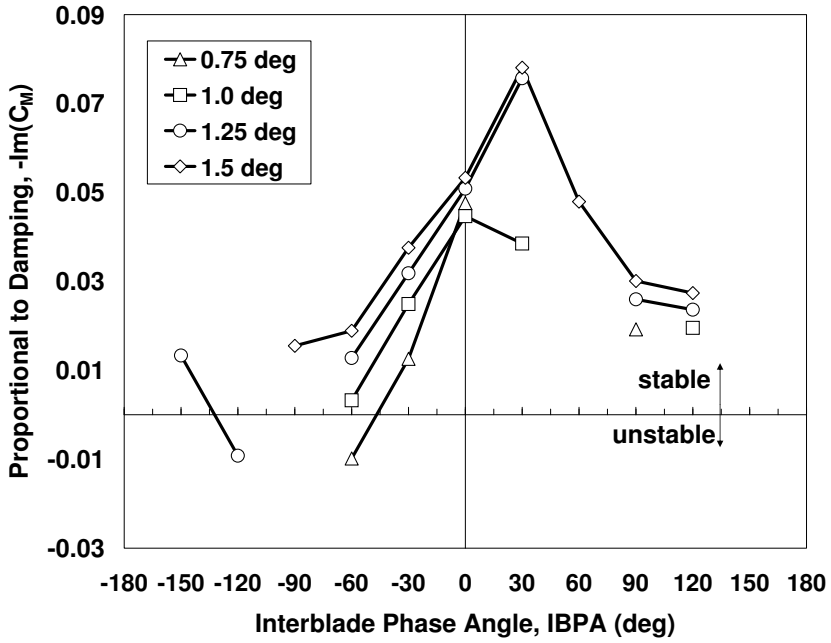

Figure 6.1: Demonstration of enforced motion design method for 2-D airfoil cascade with assumed blade frequency of 1265 Hz and 1T critical pitch amplitude of 0.75 deg.

By examining Figure 6.2 and interpolating to zero damping, the LCO amplitude for IBPA = -60 is about 0.94 deg, which is greater than the maximum allowable 1T amplitude of 0.75 deg. At an IBPA = 0 and at its natural shedding frequency of 1265 Hz, the blades are always stable. This is significant because in design practice, this is often assumed to be the worst case scenario, i.e. when the blade frequency is coincident with the fluid natural frequency. For the 2-D airfoil cascade section studied here, the analysis indicates that this is a stable condition.

Since it is not known a priori at which spanwise location NSV will be observed on a specific engine configuration, a 3-D analysis must be performed. Hence, the

2-D airfoil cascade was investigated primarily to demonstrate the merits of the HB method to predict the shedding frequency as was seen in Chapter 5 and also the use of the lock-in phenomenon as a design tool. Next, a detailed analysis of the lock-in effect will be examined for the least stable IBPA of -60 degrees and also, an IBPA = 0 degrees for comparison. The maximum LCO amplitude will be determined for each case by varying the frequency about the natural shedding frequency for its respective IBPA.

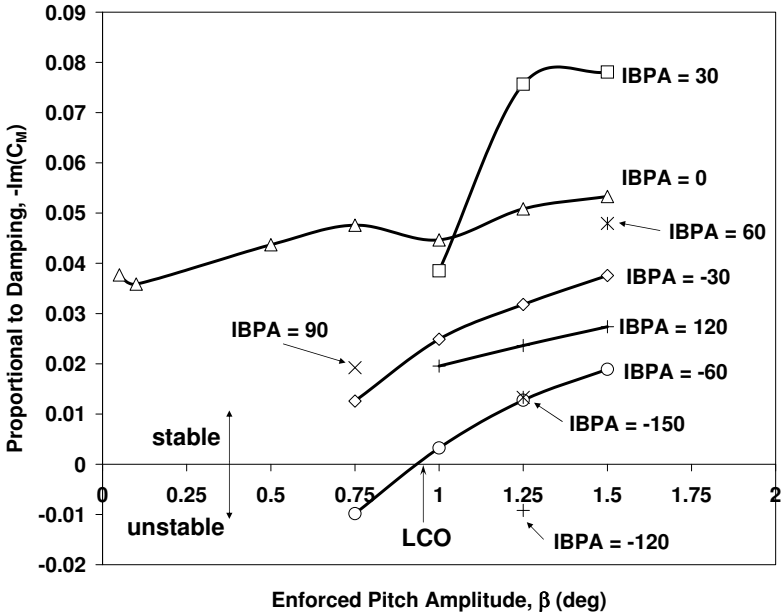

Figure 6.2: Determination of LCO amplitude at least stable IBPA = -60 deg.

6.3 Airfoil Cascade Lock-in Phenomenon

To study the cascade lock-in effect, enforced motion is used to promote lock-on of the frequency of the blades' motion to the natural shedding frequency for two IBPAs, namely IBPA = 0 and -60. In particular, it is assumed that the airfoils vibrate harmonically in pitch about midchord for a particular IBPA at a given frequency and amplitude. Analogous to the circular cylinder, there is a range of frequencies over

which the forcing blade frequency will lock-on to the natural shedding frequency.

To obtain an estimate of the lock-in bounds, the HB flow solver was used for a fixed amplitude for many different prescribed frequencies and the solution residual was noted for each case. The HB solution residual within the lock-in region converges to machine zero. Outside of this region, two distinct frequencies are observed experimentally; however the current HB method can only handle one fundamental frequency and its higher harmonics. Thus in regions where two frequencies are expected to be present, the current numerical method fails to converge. A multiple frequency HB method has been developed [22] but requires the user to input two or more frequencies and renders the method no longer efficient for NSV applications. Figure 6.3 shows this behavior for two different frequencies, one inside and one outside the lock-in region. This procedure was repeated for various amplitudes and an estimate of the left and right bounds on the lock-in region is determined based on the HB solution behavior.

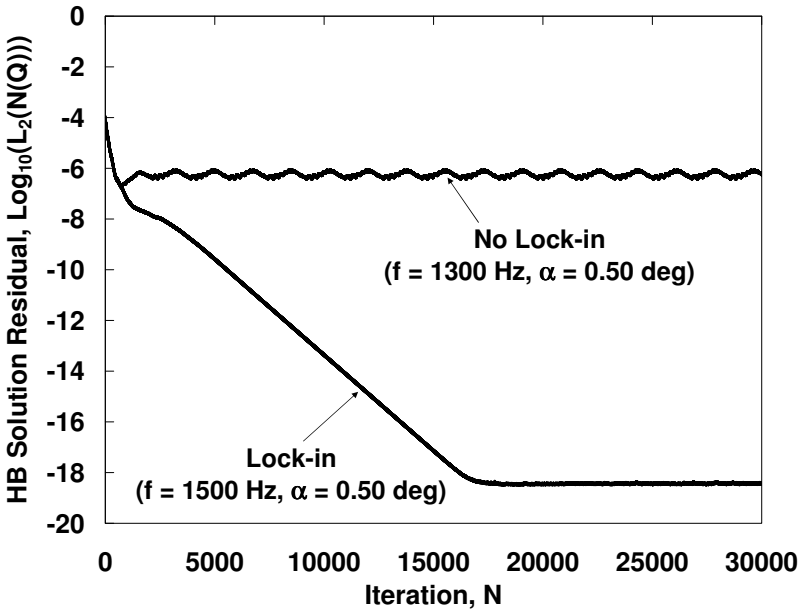

Figure 6.3: Behavior of solution residual in and out of the lock-in region.

A roughly V-shaped lock-in region is observed for both IBPAs studied and shown in Figure 6.4. For each IBPA, the prescribed blade frequency is non-dimensionalized by the natural shedding frequency without motion found in Chapter 5 to make comparisons easier. In both plots, a locked-in solution is represented by a filled in triangle and an unlocked one by an open circle. Interestingly, for an IBPA = -60, there is a higher frequency and amplitude combination that is locked-in but is outside of the lock-in region. It is hypothesized that there is another mode and therefore another possible lock-in region at higher frequencies for which the airfoil has locked. The overall goal of this section is to demonstrate the existence of lock-in regions in compressor cascade applications for design purposes and assess the stability by determining the LCO amplitudes of the rotor for two different interblade phase angle conditions. It is noted that the lock-in region is narrower for an IBPA of zero degrees as compared to the IBPA = -60 case. Further study of the underlying physics is needed to understand the reason for this difference.

Next, the stability of the cascade is examined within the lock-in region. The response outside of this synchronization regime is considered a low amplitude, off-resonant condition. Figure 6.5 shows the variation of the stability (negative imaginary part of the unsteady moment coefficient) with frequency. As the enforced pitch amplitude is increased, the rotor becomes more stable.

Furthermore, the limit cycle oscillation amplitude is determined by the amplitude for which the damping goes to zero as shown in Figure 6.6. Again, it is noted that even at low pitch amplitudes, the system is stable at the natural shedding frequency for both IBPAs. Figure 6.7 shows the LCO amplitude as a function of the forcing frequency divided by the natural shedding frequency without motion. Only one stable LCO solution is obtained for an IBPA = 0 for the frequency and amplitude range studied here. It is noted that the largest magnitude response is not at the natural

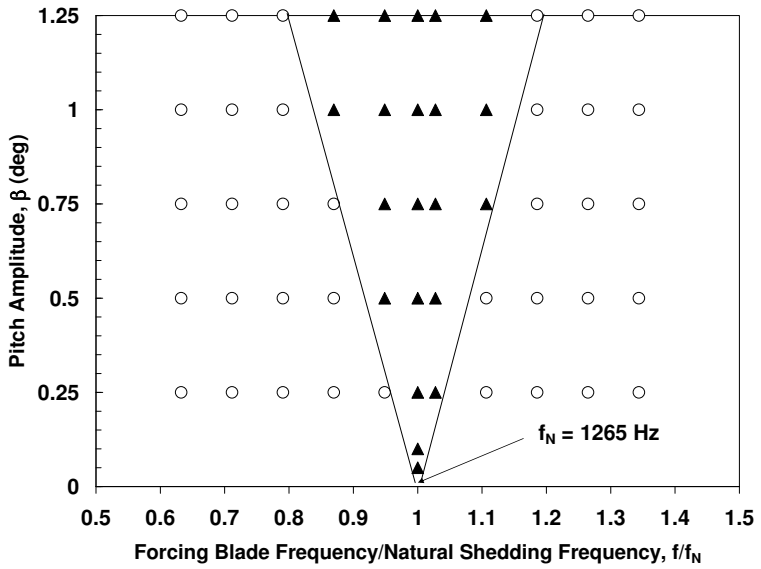

(a) IBPA = 0

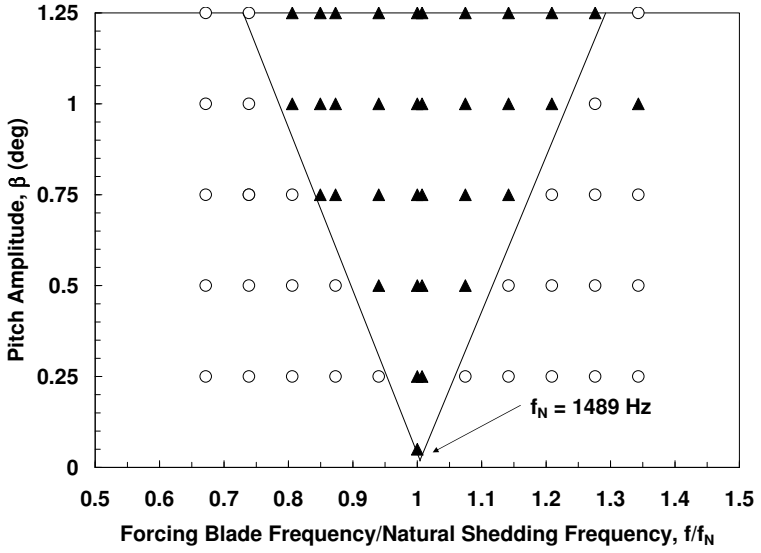

(b) IBPA = -60

Figure 6.4: Lock-in regions for two interblade phase angles for 2-D tip section of modern compressor blade.

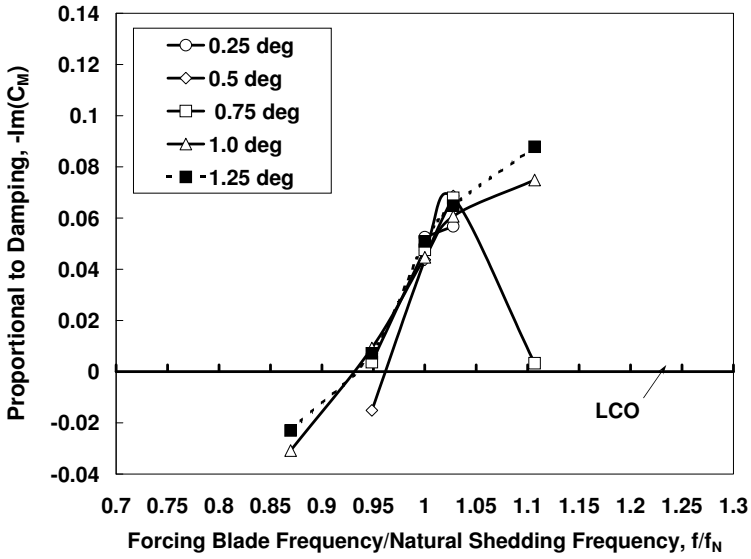

(a) IBPA = 0

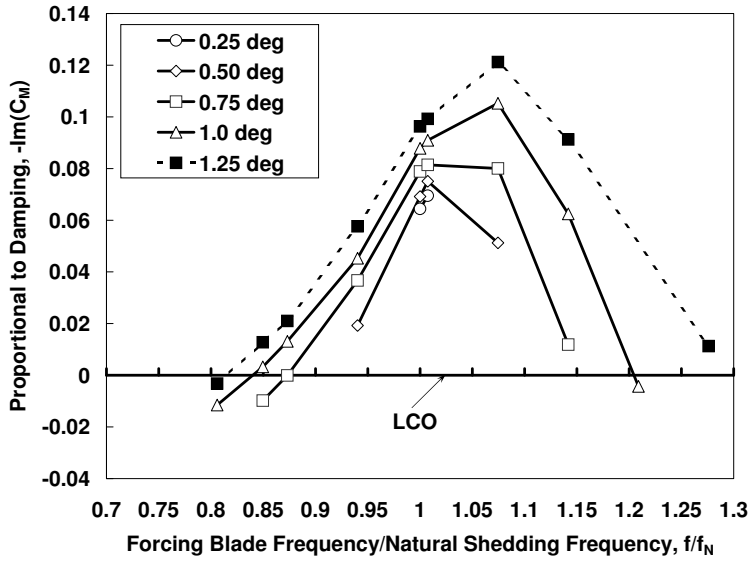

(b) IBPA = -60

Figure 6.5: Aeroelastic stability of 2-D airfoil section: negative imaginary part of moment coefficient as a function of non-dimensional frequency for locked-in frequency/amplitude combinations.

shedding frequency. In fact, the cascade is always stable at this frequency. This is contrary to conventional thought in which the worst design case is assumed to be when the natural shedding frequency matches the blade frequency. Again, it is noted that the response outside of the lock-in region is assumed to be off-resonant and low amplitude. In addition, a stable solution indicates a low amplitude response as shown in Figure 6.7. The lock-in bounds are also included for reference. Therefore, using the current analysis techniques, an incorrect prediction of NSV would result. This indicates that blade motion is necessary in order to adequately design for NSV. To further validate this conclusion, it is necessary to investigate this observation at other IBPAs and for other test cases.

6.4 Summary

In this chapter, the enforced motion method was demonstrated for a 2-D compressor cascade section undergoing harmonic pitch motion about midchord with a 1T critical amplitude of 0.75 degrees and an assumed blade frequency of 1265 Hz. It is determined that the design is unacceptable since the LCO pitch amplitude for an IBPA = -60 is greater than the maximum allowable amplitude. Therefore, an IBPA = -60 was chosen to perform a more in-depth study of the lock-in phenomenon. For comparison, an IBPA = 0 was also investigated.

Using knowledge of the stationary natural shedding frequency, enforced pitch motion was then used to promote lock-on of the blade frequency to the natural shedding frequency without motion for two IBPAs, namely IBPA = 0 and -60 degrees. Analogous to a circular cylinder, a V-shaped lock-in region is observed for both IBPAs studied. It is noted that the lock-in region for an IBPA = 0 was narrower than that obtained for IBPA = -60. In addition, the relative size of the lock-in region was compared with the blade studied by Zhu and Kamemoto. The lock-in frequency

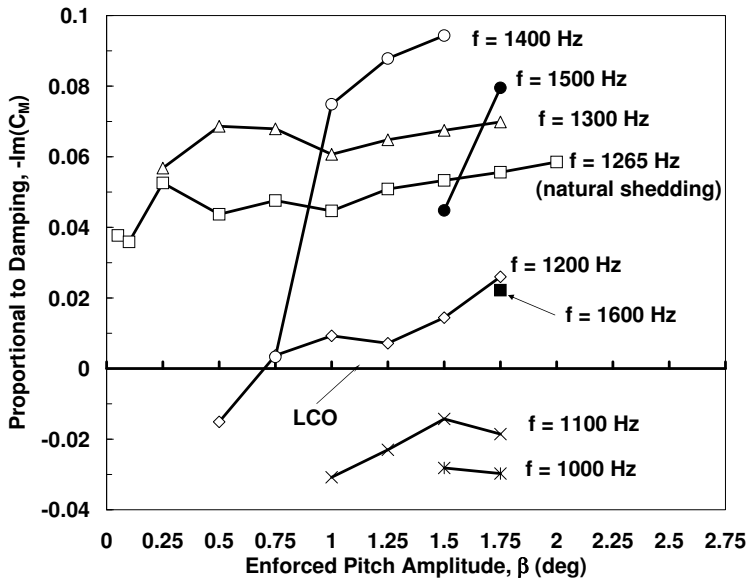

(a) IBPA = 0

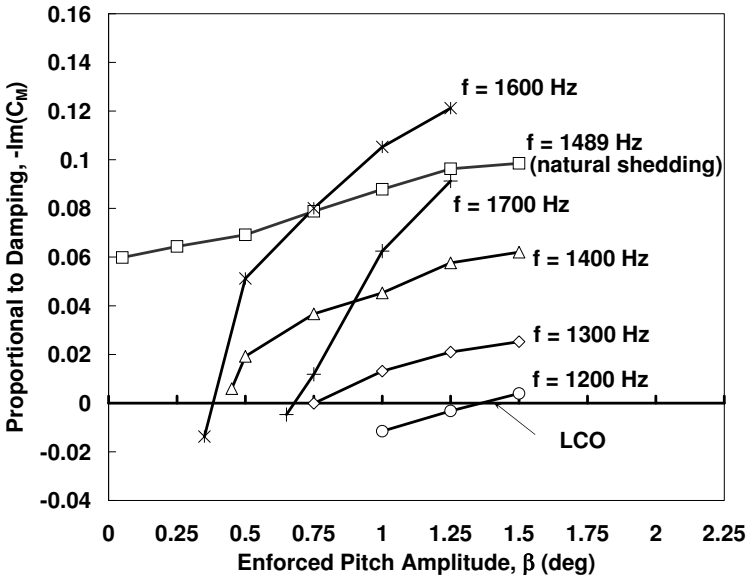

(b) IBPA = -60

Figure 6.6: Determination of LCO amplitude as a function of non-dimensional frequency for respective IBPAs.

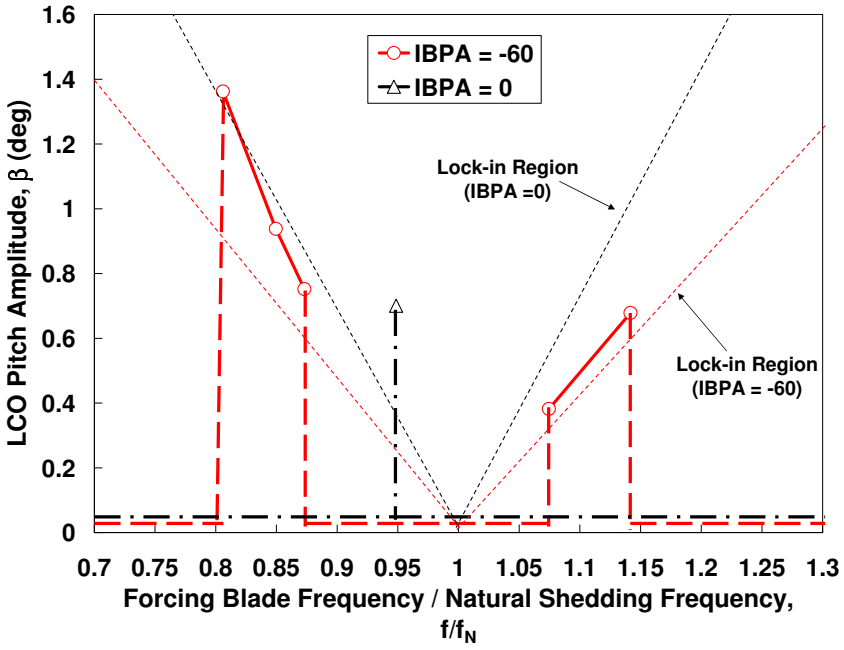

Figure 6.7: LCO amplitude as a function of non-dimensional frequency for IBPA = 0 and IBPA = -60.

band (±15%) for an amplitude of 1.5 degrees is approximately the same as that obtained for an IBPA = 0 degrees.

Furthermore, the stability of the rotor is determined. Most significantly, it is found that the system is aeroelastically stable (positively damped) at the blade's natural shedding frequency. Furthermore, the largest response is at a frequency other than the natural shedding frequency. This is contrary to conventional thought in which the worst case scenario is assumed to be when the blade frequency is coincident with the frequency of the fluid dynamic instability. Furthermore, using the current analysis techniques, an incorrect prediction of NSV would result as much higher amplitude responses would occur at other blade frequencies. These 2-D airfoil cascade results indicate that airfoil motion is important and necessary to adequately design for NSV.

Chapter 7

Application of Enforced Motion Method to Full 3-D Turbomachinery Blade Model

In this chapter, the enforced motion method is demonstrated for a first stage modern compressor blade that encountered NSV in compressor rig testing and was previously studied by Kielb et al. [3] For this test, there were 35 rotor blades and 56 inlet guide vanes (IGV's). The stage 1 blades are observed to experience a significant first torsion mode (1T) response at lower speed that shifts to a second torsion mode (2T) response at somewhat higher speed. Figure 7.1 shows an example plot of blade response frequency and amplitude versus rotational speed. The vertical lines at fixed values of rotor speed and frequency are a measure of blade response amplitude at that frequency. The response at low speed is a moderate separated flow vibration (SFV) response of the first flex (1F) and 1T modes. SFV is a broadband buffeting-like response of the blades. This SFV 1F response is followed at higher speeds by a significant NSV, which excites the 1T mode to a high level of response. This response switches from a higher frequency (2661 Hz) excitation to a lower frequency (2600 Hz) excitation at a somewhat higher speed. As the speed further increases, the response switches to a 2T mode excitation. The NSV excitation of the 1T mode exists from approximately 12700 to 12880 rpm.

In a previous study, the unsteady CFD code, TURBO [18] was used to investigate the NSV observed in the rig test. A single row, five passage mesh modeled one-seventh of the rotor circumference. The mesh, consisting of 188 axial, 56 radial, and 280 circumferential grid points, contained approximately three million grid points. Using TURBO, the analysis would have taken about six months to run on a single processor.

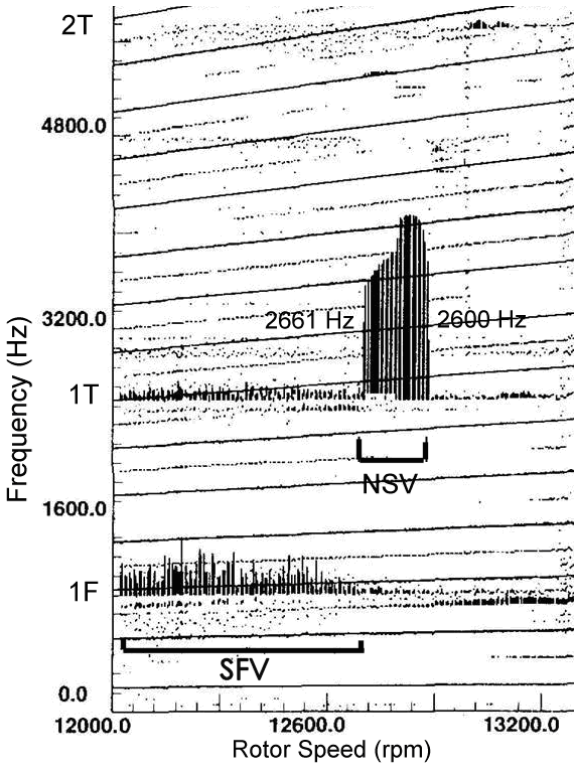

Figure 7.1: Strain gauge response of first-stage rotor blades of compressor rig [3].

The local unsteady static pressures from the periodic CFD solution were investigated at many locations on the blade surface near the blade tip. This is shown in Figure 7.2, where the unsteady static pressures in passage three, near the leading edge on the pressure side, are presented. As can be seen, the unsteady pressure content at 2365 Hz and 4730 Hz is much greater than that at the vane passing frequency. The predicted NSV frequency (2365 Hz) is approximately 9% lower than that measured in the rig test. The TURBO results show that NSV is primarily a coupled, suction side vortex unsteadiness (near 75% span) and tip flow instability.

7.1 3-D Compressor Cascade Without Motion

In a first attempt to replicate the experimental data and the TURBO computational results, similar flow conditions were used and the analysis was performed by Jeffrey

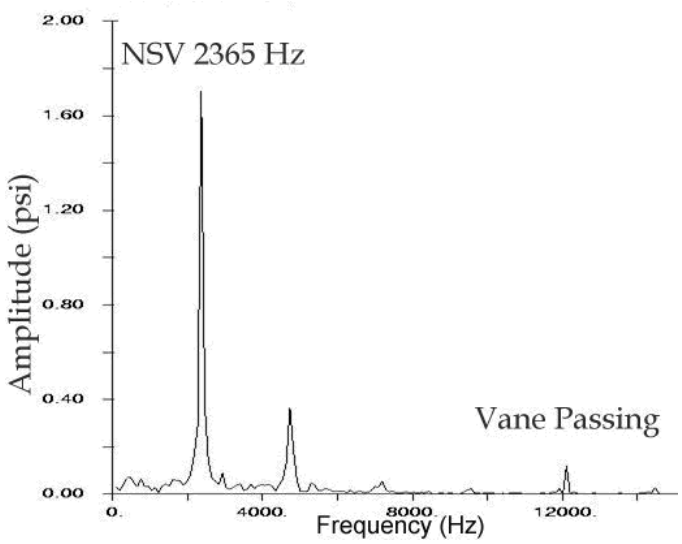

Figure 7.2: Unsteady static pressure near tip pressure side near leading edge [3].

Thomas using Duke University's time domain and HB computational methods [19] [1]. The computations were performed using a single blade passage and an H-O-H grid with 9 x 25 x 41 nodes in the H-grid sections and 161 x 25 x 41 nodes in the O-grid section. Furthermore, the tip clearance is modeled. The inlet Mach number M is 0.35 and the inlet flow angle θ = -10 deg in the relative frame. The Reynolds number is of order 10^6 so the flow is fully turbulent. All analysis is conducted using three harmonics. It becomes prohibitively expensive to retain more than three harmonics for full 3-D blade applications on standard computing machines. In particular, it requires considerable computational time and large memory storage. A summary of the NSV frequency results obtained can be found in Table 7.1 for a range of back pressure ratios (PRs) and two tip clearances. Here, an "X" is used to indicate the PRs for which the HB method was not able to get a solution.

	Running Clearance (0.020 in)		Tight Clearance (0.002 in)	
PR	Time Domain (Hz)	HB (Hz)	Time Domain (Hz)	HB (Hz)
1.000	No NSV	No NSV	2000	2000
1.015	f_1 =2650	X	3200	X
	f_2 = 50	X	3750	X
1.020	f_1 =2850	X	———	———
	f_2 =Low Freq	X	———	———

Table 7.1: Summary of time domain and HB results for both the running and tight tip clearances for three different pressure ratios.

7.1.1 Rig Test Running Tip Clearance

A time domain CFD analysis was conducted using the running clearance of 0.020 in., zero interblade phase angle, and various back pressures, namely $PR = \frac{p_{exit}}{p_{exit_{CAFD}}} =$ 1.000, 1.010, 1.015, and 1.020 where "CAFD" is the exit pressure for which NSV was encountered in the experiment. The PRs are slowly increased in order to get NSV to occur in the numerical simulation. For the cases of $\frac{p_{exit}}{p_{exit_{CAFD}}} = 1.000$ and 1.010, the flow is steady and no NSV is encountered. However, at PR = 1.015, NSV occurs. The time history results for mass flow rate and blade torque are presented in Figures 7.3 and 7.4, respectively.

In Figures 7.5 and 7.6, Fast Fourier transforms (FFTs) of the time domain results for the blade torque for back pressures of $\frac{p_{exit}}{p_{exit_{CAFD}}} = 1.015$ and 1.020 were computed to determine the NSV frequency. For the 0.020 inch clearance case and $\frac{p_{exit}}{p_{exit_{CAFD}}} =$ 1.015, the predicted NSV frequencies are about $f_1 = 2650$ Hz and $f_2 = 50$ Hz. For the 0.020 inch clearance case and $\frac{p_{exit}}{p_{exit_{CAFD}}} = 1.020$, the predicted NSV frequencies are about $f_1 = 2850$ Hz and a very low frequency component (see Figure 7.5). Figure 7.6 zooms in on the results for $\frac{p_{exit}}{p_{exit_{CAFD}}} = 1.020$ in the 0-100 Hz range, where the very low frequency component is present. It is noted that f_2 is not a multiple of f_1. Therefore, for these cases, two distinct frequencies are present in the solution.

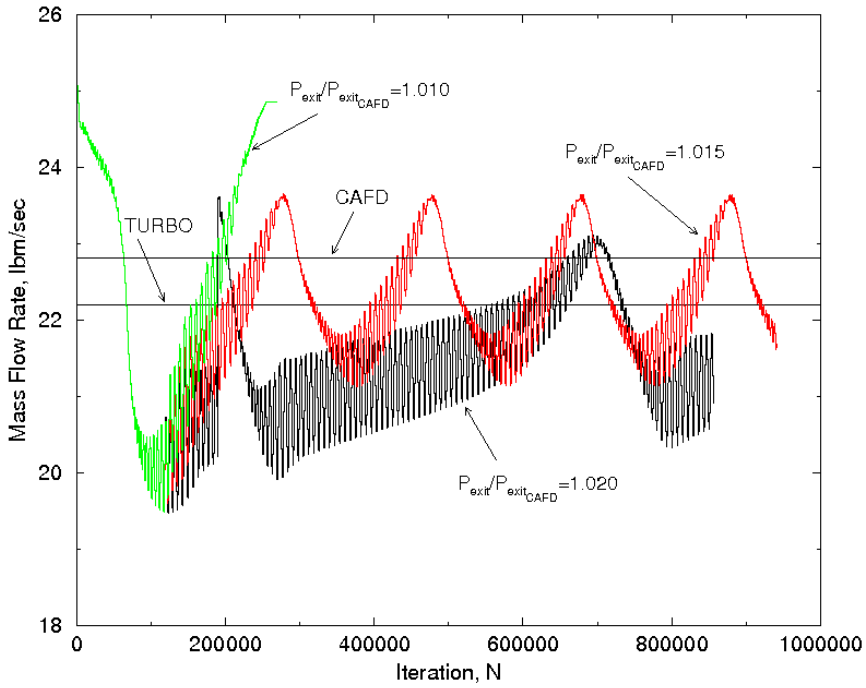

Figure 7.3: Time domain solution mass flow rates for different back pressures (0.020 in. running tip clearance) [2].

Next, the harmonic balance solver was used to study this case. As described previously, the phase error method was attempted to search directly for the frequency of the instability. The phase change per iteration of the unsteady torque is shown in Figure 7.7 for five assumed frequencies with the same conditions as the time domain case. As can be seen, the phase change reaches a constant value for 2.5 and 2.6 KHz. For 2.65 and 2.75 KHz, the phase change does not converge to a constant value. This is likely because the fluid dynamic instability contains multiple (irrational) frequencies.

7.1.2 Tighter Tip Clearance for Demonstration of HB Method

Due to the limitations of the HB method to only handle one frequency, a tight tip clearance case was also examined at an IBPA = 0 deg. Figure 7.8 shows the time

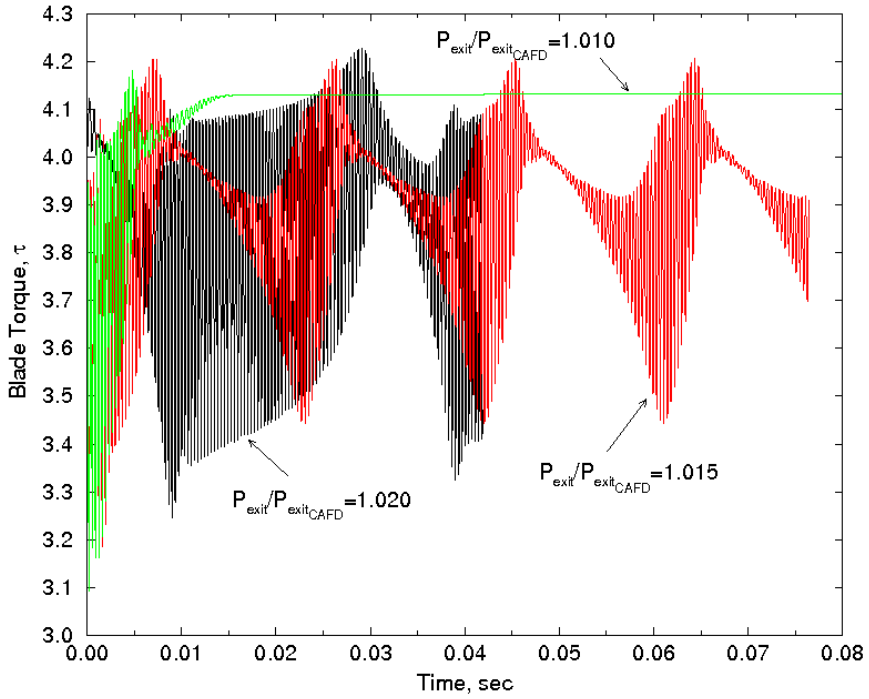

Figure 7.4: Time history of blade torque for various back pressures (0.020 in. running tip clearance) [2].

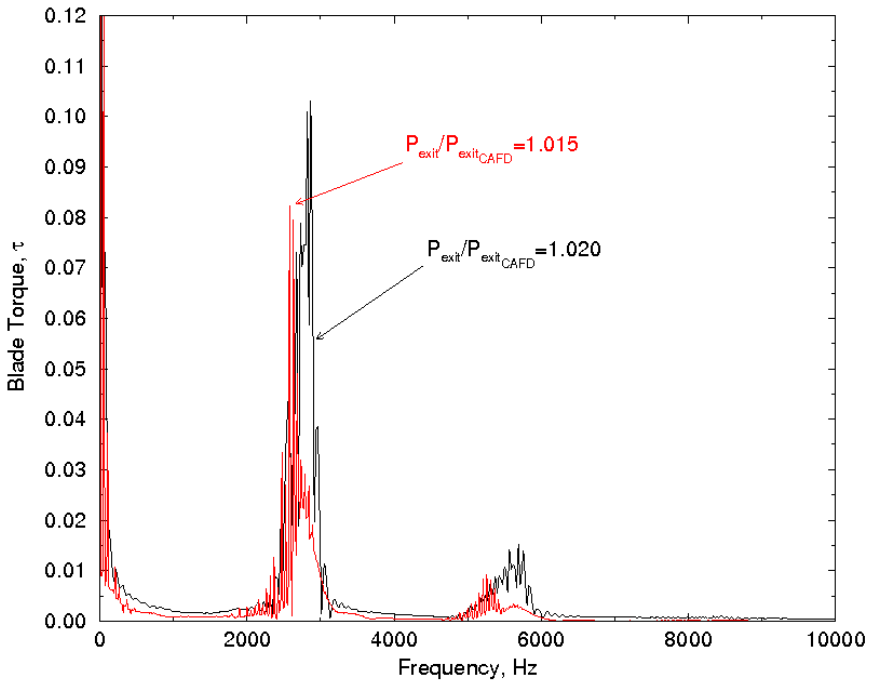

Figure 7.5: FFT of blade torque for two different back pressures (IBPA = 0, 0.020 in. running tip clearance) [2].

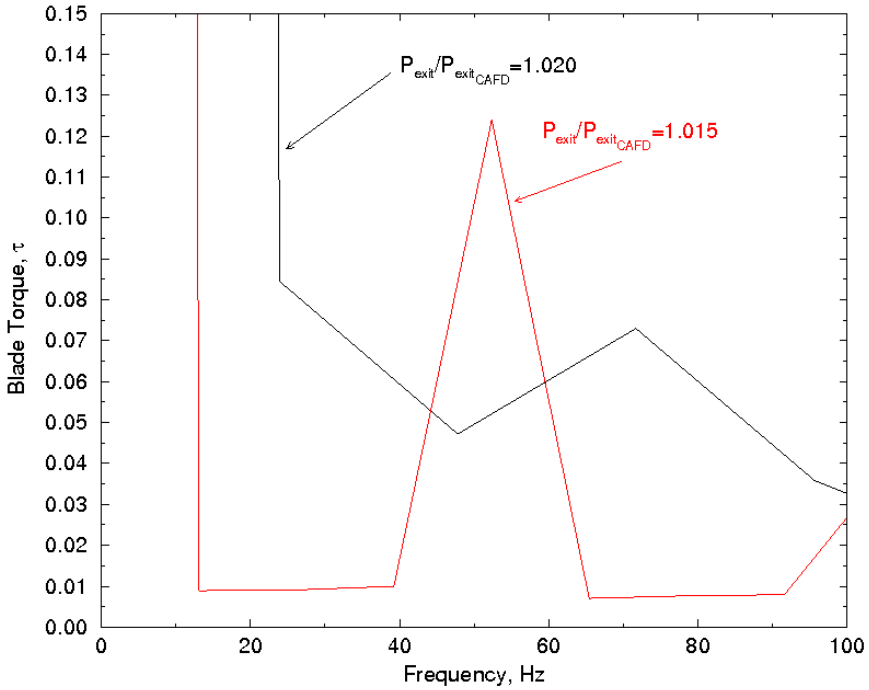

Figure 7.6: FFT of blade torque for two different back pressures (IBPA = 0, 0.020 in. running tip clearance) in low frequency region [2].

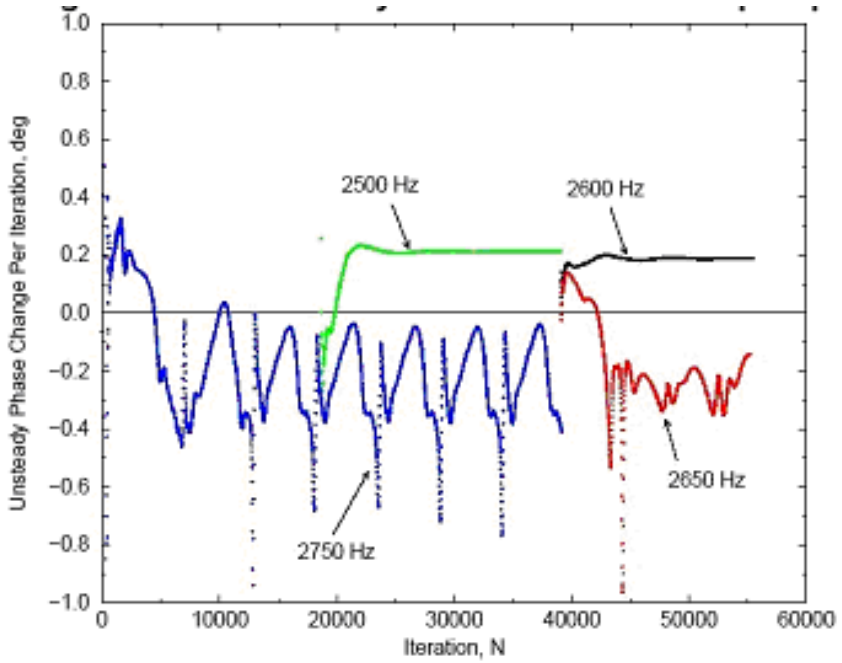

Figure 7.7: Phase change per iteration (IBPA = 0, 0.020 in. running tip clearance, $\frac{p_{exit}}{p_{exit_{CAFD}}} = 1.020$ [2].

history of blade torque for the tight tip clearance case and Figure 7.9 shows the FFT of the time domain solution along with the HB result. As can be seen, at the back pressure encountered in the experimental rig ($p_{exit}/p_{exit_{CAFD}} = 1.000$), both the time domain method and the HB solver predict an NSV frequency of 2000 Hz. However, as can be seen in Table 7.1, for the $p_{exit}/p_{exit_{CAFD}} = 1.015$ case, the time domain method predicts NSV frequencies of 3200 Hz and 3750 Hz. Therefore, the higher back pressure case has two distinct, irrational frequencies (beats) present, and HB can only handle one fundamental frequency and its harmonics. It is speculated that the HB method shows good agreement with the time domain method for the lower back pressure case since there appears to be only a single frequency, and higher harmonics thereof, present in the time domain solution.

Although good agreement is achieved in frequency for $p_{exit}/p_{exit_{CAFD}} = 1.000$, the HB method tends to under predict the amplitude of the blade torque at the fundamental frequency and over predict the amplitudes at the 2nd and 3rd harmonic. Despite the small differences in harmonic amplitude prediction, the HB method seems to adequately model the NSV phenomena for the tighter tip clearance case. Hence, the harmonic balance method is a useful tool but it necessitates the existence of only one dominant frequency in the fluid. It is also important to note here that the HB method does not improve the "physics". It's advantage lies in its efficiency. If the time domain code cannot predict NSV, then the HB method won't be able to either. Some possible solutions to overcome the shortcoming of the standard harmonic balance method and its ability to only handle one fundamental frequency and higher harmonics thereof are to extend the HB method to handle multiple irrational frequencies, use enforced motion to cause "lock-in" to the blade frequency, or use the aeroelastic solution to cause "lock-in" to the non-linear flutter frequency (very near the blade frequency).

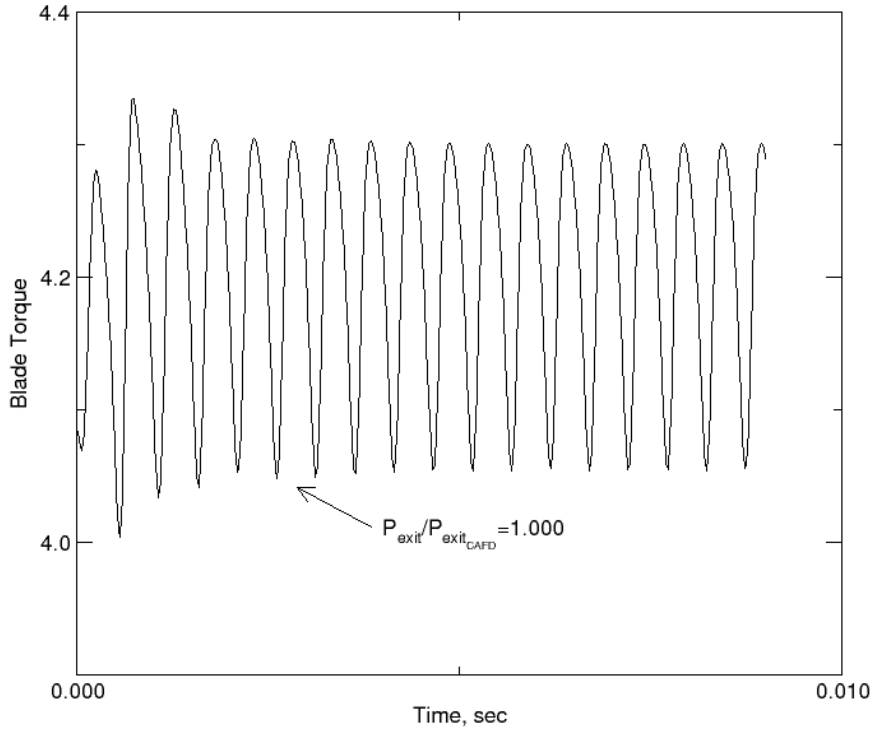

Figure 7.8: Time history of blade torque for a 0.0002 in. tight tip clearance and IBPA = 0 [4].

A multiple frequency harmonic balance method has been developed by Ekici et al. [22] but it would require the user to guess two or more frequencies which is no longer computationally efficient for turbomachinery NSV design applications. Furthermore, solving the fully, coupled aeroelastic solution would take consider computational time and it was shown for the cylinder that the enforced motion method can yield comparable results. Therefore, for the purpose of this study, the enforced motion method was examined in detail. The enforced motion method is computationally efficient and it is similar to the current industry method for linear flutter analysis.

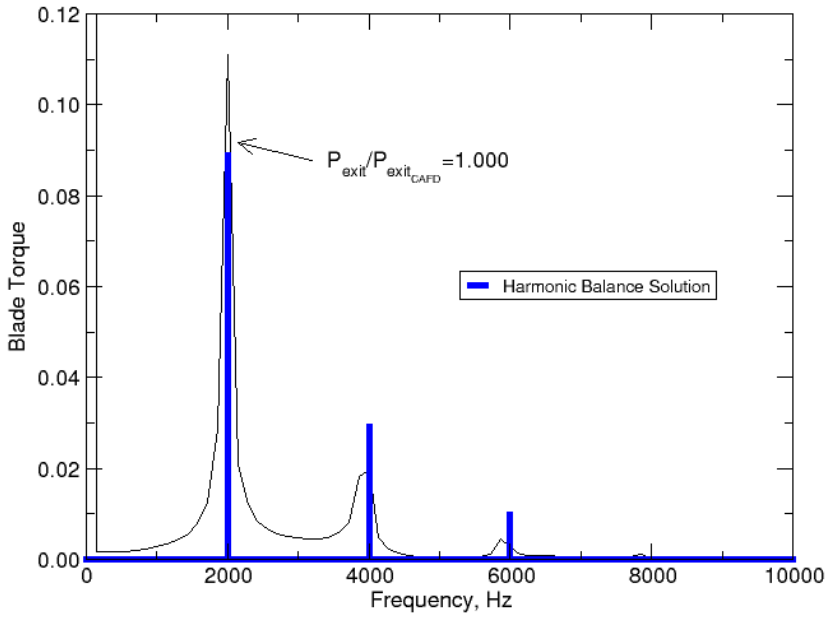

Figure 7.9: FFT of blade torque compared with harmonic balance solution (0.0002 in. tight tip clearance and IBPA = 0) [4].

7.2 3-D Cascade at Prescribed Frequencies

As was discussed previously, the lock-in phenomenon has been well-studied for cylinders (see for example, Blevins [49], Williamson [40], Sarpkaya [42], Anagnostopoulos [50], and Tanida [43] and most recently demonstrated for a 2-D airfoil in laminar flow [65]. Gostelow et al.[64] have also observed vortex shedding flows behind blunt trailing-edge turbine blades. In subsonic conditions, the turbine nozzle cascade sheds wake vortices in a conventional Von Karman vortex street but under transonic conditions, a variety of different shedding configurations were observed. However, they do not report the existence of a lock-in region. This section highlights the application of the proposed enforced motion design method to a modern front stage high pressure compressor rotor blade. The enforced motion method exploits the lock-in effect be-

tween the fluid frequency and the blade vibration frequency at a critical amplitude to determine whether or not a design is acceptable.

In particular, lock-in is achieved when the fluid frequency "jumps" to the blade vibration frequency at a particular amplitude and therefore only the blade frequency is present in the system. This allows the use of the standard harmonic balance analysis which can only handle one fundamental frequency and its higher harmonics inside the lock-in region. The lock-in region is centered about the blade mode frequency. It is assumed that the condition for which the frequencies are unlocked is a low amplitude, off-resonant response and therefore not considered significant.

7.2.1 Enforced Motion Design Method

The enforced motion design method is now applied with the running tip clearance of 0.020 in. and a back pressure ratio $PR = 1.020$. From Table 7.1, the dominant natural shedding frequency without motion is 2850 Hz found from a time domain analysis. First, in accordance with the enforced motion design method, the nonlinear HB method was conducted at a critical 1T modal amplitude of 0.0001 and an assumed blade frequency of 3500 Hz for a range of IBPAs as shown in Figure 7.10. A critical modal amplitude of 0.0001 is chosen because it corresponds to the stress levels encountered in the experimental rig test. Each run of the harmonic balance code takes about 3 weeks to achieve machine zero convergence on a single processor. However, it is computationally advantageous to run all IBPAs at the chosen amplitude and frequency at the same time on different machines. Therefore, one is able to make an initial assessment of whether or not a design is acceptable in a fraction of the time it takes to run a full 3-D CFD time domain simulation. From Figure 7.10, it can be seen that the 1T mode is unstable over most of the nodal diameter range so the design is unacceptable. Furthermore, it is important to note that the fluid frequency

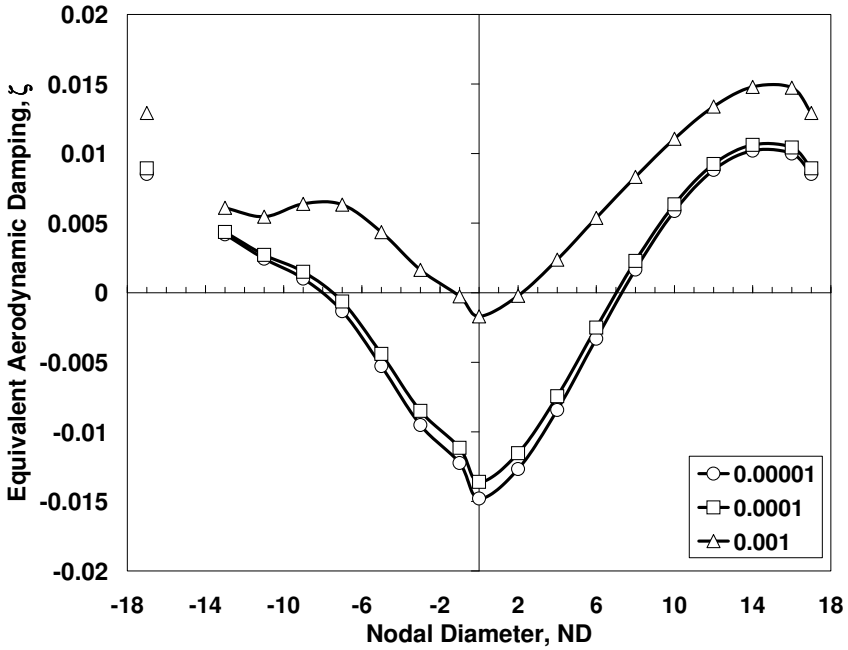

Figure 7.10: Equivalent aerodynamic damping as a function of nodal diameter (ND) for fixed blade frequency = 3500 Hz and critical modal amplitude of 0.0001.

is not locked into the blade frequency for ND = -16 at the critical modal amplitude of 0.0001. Therefore, it is assumed that the blade vibration amplitude for that case is small and not significant. In addition, two other assumed critical amplitudes are chosen for reference. As one would expect, if a higher critical modal amplitude is allowed, the blade becomes more stable at all nodal diameters. Conversely, a smaller amplitude becomes slightly more unstable.

In addition, the effect of assuming different fixed blade frequencies is investigated. In particular, blade frequencies of 3000, 3100, and 3500 Hz are chosen. Figure 7.11 shows the equivalent aerodynamic damping as a function of interblade phase angle for the three assumed blade frequencies. It is important to note that the least stable IBPA is different for each frequency and therefore, very sensitive to the assumed blade frequency.

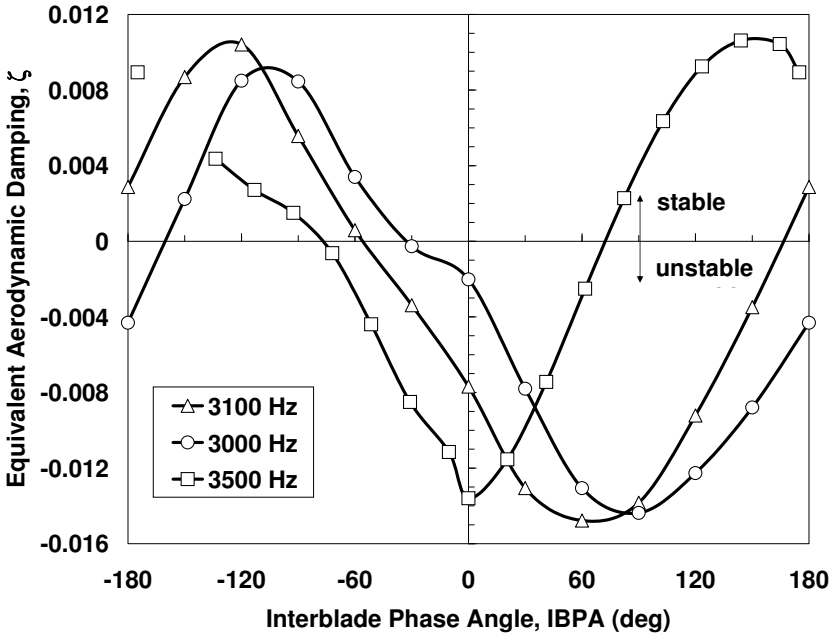

Figure 7.11: Equivalent aerodynamic damping as a function of interblade phase angle (IBPA) for three different fixed blade frequencies of 3000, 3100, and 3500 Hz at a critical modal amplitude of 0.0001.

7.2.2 Blade Re-design Frequency Changing Procedure

In order to determine a better blade design, the most unstable ND (0 deg) is chosen. According to the enforced motion method, one can then run a range of frequencies (including the blade frequency) and a range of modal amplitudes to determine those for which the fluid frequency is locked on to the blade frequency. For this case, lock-in is achieved for all frequencies and amplitudes investigated. Then, the equivalent aerodynamic damping is calculated using Equation 1.1 at the locked-in frequencies. It is known from time domain simulations that the dominant natural fluid frequency with no motion for an IBPA = 0 is 2850 Hz for a back pressure ratio of 1.020 (see Table 7.1). Using this fixed aerodynamic condition, the blade frequency was then varied from 2000 Hz to 4000 Hz and the modal amplitude was increased from 0.00005 to 0.005 to determine the LCO amplitude for each frequency. A positive damping

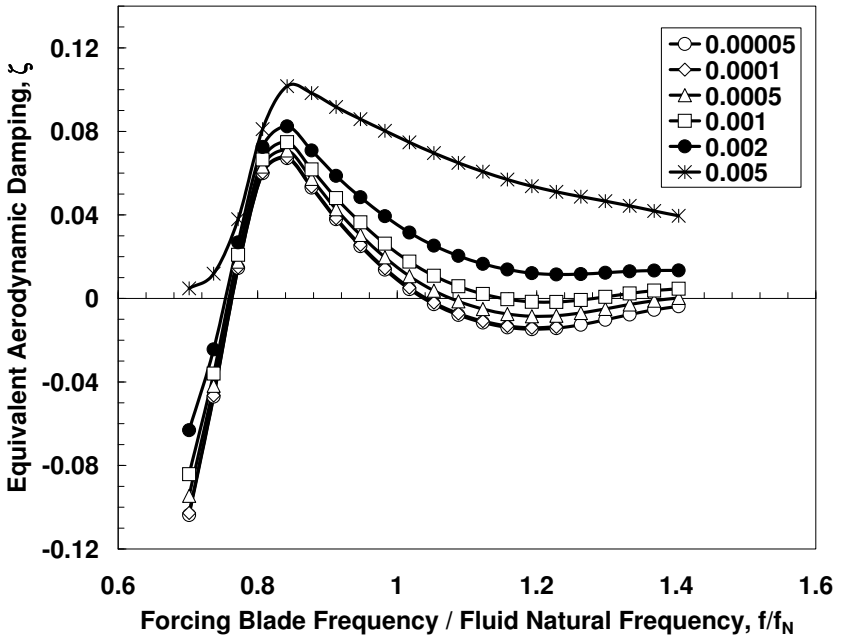

Figure 7.12: Equivalent aerodynamic damping as a function of frequency for IBPA = 0 deg.

indicates that the blade is stable at that frequency so NSV will not occur. Similarly, a negative damping indicates that the system is unstable and NSV will occur. The LCO amplitude is then determined as the amplitude for which the damping goes from positive to negative.

Hence, the aerodynamic damping was calculated for all frequencies and amplitudes within the lock-in region and the LCO amplitude was determined for each frequency (if becomes unstable). The results are shown in Figure 7.12 and as expected, the stability generally improved as the enforced motion amplitude is increased for all frequencies. Next, the equivalent aerodynamic damping was plotted as a function of the enforced modal oscillation amplitude as seen in Fig. 7.13. For the $f = 3500$ Hz case, the low amplitude region has been zoomed in Figure 7.14. As expected, the slope is approximately zero indicating the the damping is independent of amplitude in that region. Hence, this is the linear region. Stable LCO solutions are

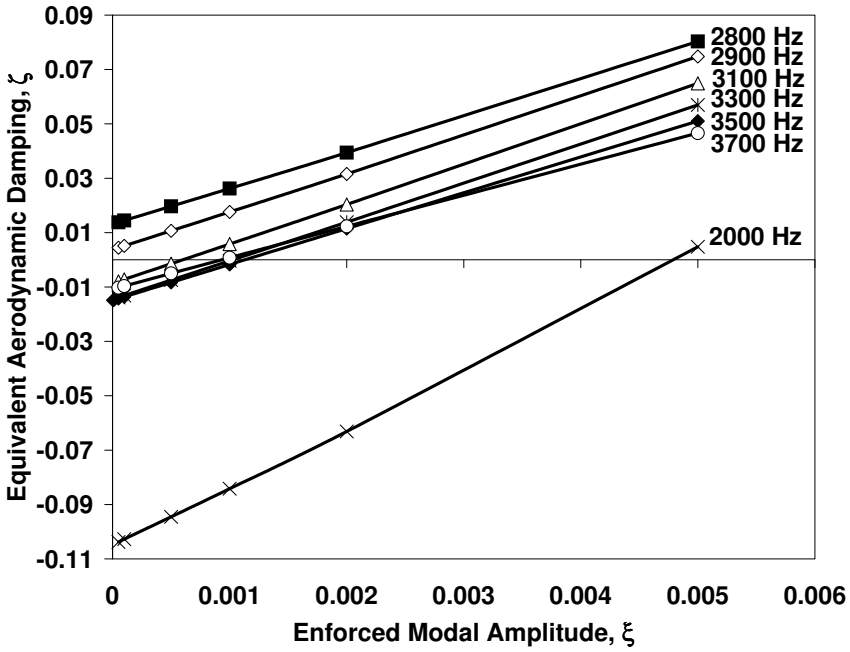

Figure 7.13: Equivalent aerodynamic damping as a function of modal oscillation amplitude for IBPA = 0 deg.

obtained for f = 2000, 2100, and 3000 - 4000 Hz as shown in Figure 7.15. An inverted parabolic trend is obtained for the LCO amplitude as a function of frequency with the maximum vibratory response occurring at a frequency of 3500 Hz. Similar to the 2-D cascade, the largest response is at a frequency other than the natural shedding frequency of 2850 Hz. In fact, Figure 7.15 indicates that the blade is stable at the natural shedding frequency. Using the currently available analysis techniques, an incorrect prediction of NSV would result since the maximum response is assumed to occur when the blade frequency matches the natural fluid frequency. Therefore, when re-designing blade, it will actually be advantageous to design the blade to have a 1T blade frequency that is near 3000 Hz or 4000 Hz to minimize the blade vibratory amplitude. These results further demonstrate the need to include blade motion in NSV design methods.

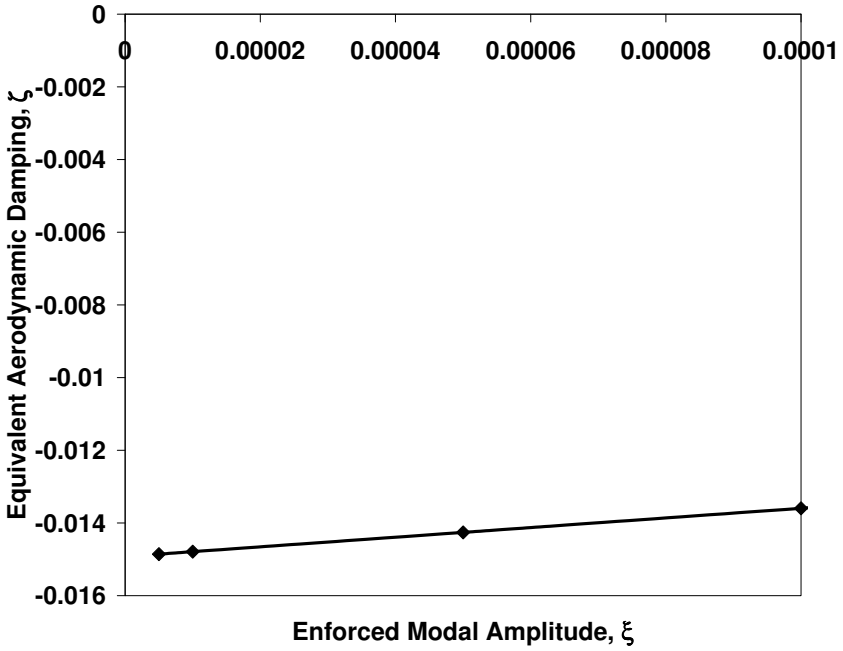

Figure 7.14: Equivalent aerodynamic damping as a function of modal oscillation amplitude in low amplitude region for IBPA = 0 deg at the blade frequency of 3500 Hz.

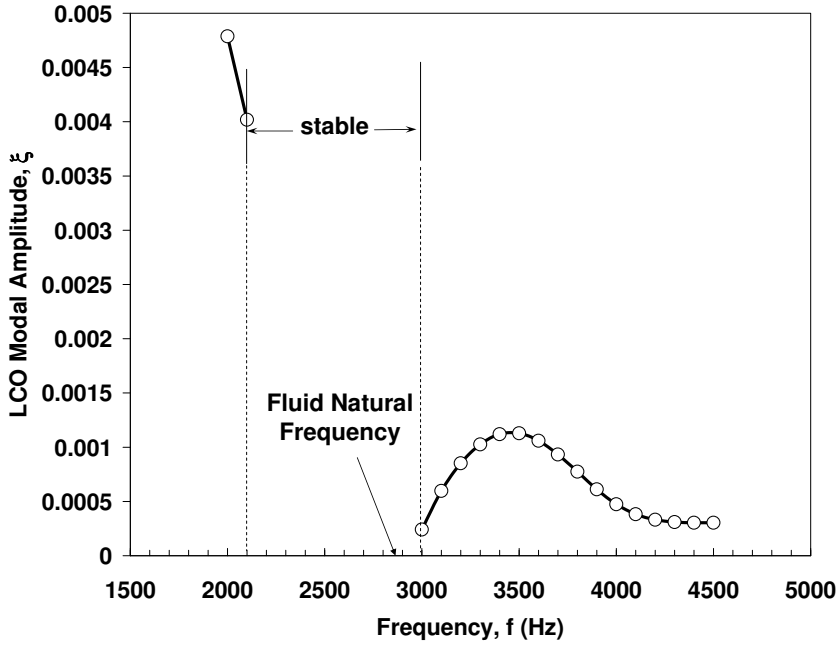

Figure 7.15: LCO amplitude as a function of frequency for IBPA = 0 deg.

7.3 Summary

Here, the enforced motion design method was demonstrated for a modern first stage compressor rotor blade that encountered NSV in rig testing. The first numerical investigation of a full 3-D cascade with blade motion is presented. First, the direct frequency search method was applied. Two main design parameters were varied - the tip clearance and the back pressure. Using the running tip clearance of 0.020 in., the fluid contained multiple irrational frequencies so the direct frequency search was no longer computationally efficient for NSV applications. Hence, it was determined that the enforced motion design method was a better alternative for an efficient design method. First, a tighter tip clearance (0.002 in. vs. 0.020 in.) was examined to demonstrate the HB method's ability to model highly non-linear NSV flows. Good agreement was achieved in frequency between the time domain and HB results but the HB method under predicted the first harmonic and over predicted the higher harmonics.

Next, the enforced motion method was applied using the running tip clearance of 0.020 in. for a fixed blade frequency of 3500 Hz and a 1T modal amplitude of 0.0001 over a range of nodal diameters. The time domain results for a zero degree interblade phase angle found that the dominant frequency of the instability without blade motion is 2850 Hz. By performing an IBPA sweep at the aforementioned conditions, it was found that the 1T mode was unstable over most of the range so NSV is predicted to occur and the design is deemed unacceptable. Furthermore, the results were achieved at a fraction of the time it takes to run a full 3-D time domain CFD simulation.

In addition, this method allows for a quick way to re-design the blade by changing frequency. At the least stable ND = 0, the LCO amplitude was calculated for

a range of frequencies and it was determined that the blade should be designed to have a 1T blade frequency that is near 3000 Hz or 4000 Hz to minimize the blade vibratory amplitude. It was discovered that the maximum blade response was not at the natural shedding frequency as is commonly assumed in current design analysis. Most significantly, the blade is stable at the natural shedding frequency. These preliminary results indicate that it is imperative to include blade motion in NSV design approaches to capture the maximum blade response. Furthermore, unlike the cylinder, the 3-D case never unlocked. Currently, lower frequencies and amplitudes are being investigated to see if the blade frequency will unlock from the fluid frequency. Further study will also be conducted on other 3-D test cases as well to determine the merits of the method to handle all types of flow instabilities and blade geometries. Ultimately, the authors hope that this method will become an efficient preliminary design tool for NSV.

Chapter 8

Conclusions

The primary goal of this research effort was to develop an efficient design method to avoid non-synchronous vibrations for routine use by industry. Since the underlying mechanisms of NSV are not well understood, predictive tools have yet to be developed so failures typically don't occur until the testing phase, which is costly and greatly increases production time. This dissertation presented a new approach to understand a complex flow phenomenon encountered in turbomachinery configurations. The purpose of the research effort was not to improve the CFD method itself but to use existing CFD techniques to establish a method for industry to design for NSV. By implementing novel techniques, the following research objectives were met:

- Developed and demonstrated a direct frequency search method utilizing a novel phase error technique and discussed its shortcomings for full 3-D blade compressor cascade analysis
- Demonstrated that the direct frequency search method is not a sufficient design method and it can incorrectly predict the maximum blade response
- Performed first in-depth study of a 3-D cascade that experienced NSV in rig testing with blade motion
- Implemented a unique enforced motion method in which lock-in is used to encourage the fluid natural frequency to jump to the blade natural frequency at a specified critical amplitude

- Applied both methods to a circular cylinder with extensive experimental data, a 2-D airfoil cascade section to compare with time domain results, and a 3-D HPC cascade with existing experimental and time domain data

- Conducted in-depth studies of generated unsteady forces and compared with available experimental and computational data

- Developed an efficient and systematic method that is easily adoptable to existing preliminary design practice because it is an extension of a linear flutter analysis which is typically already conducted for infinitesimal amplitude

Currently, the two main aeroelastic design considerations for turbomachinery blading are flutter and forced response. Both of these aeroelastic phenomena have been well-studied and efficient industry design methods are established. In addition, the design analysis only requires the use of linear CFD techniques. However, NSV occurs as a result of the complex interaction of an aerodynamic instability with blade vibrations. It is encountered at non-integral multiples of the shaft rotational frequencies, far from the classical flutter regime. NSV has been most commonly seen in the front stages of high pressure compressor (HPC) and the blades, vanes, and blisks of fans. It is a serious aeroelastic problem that has been observed by most engine companies and the unsteady loading can reach levels high enough to cause blade HCF failures. In this work, a detailed study of NSV was conducted and an efficient design method was developed.

Two design methods were presented in this dissertation and the merits of each were examined. The current industry analysis method, termed the direct frequency search method in this dissertation, is to search directly for the frequency of the instability using CFD analysis and then compare it with a fundamental blade mode frequency determined from a structural analysis code. A unique phase error method

is used to determine the fluid natural frequency in as few as two HB solution computations. This search technique utilizes the phase difference between successive iterations of an unsteady first harmonic quantity such as unsteady lift. The main disadvantage of this method is that the blades' motion is not considered and therefore, the maximum response is assumed to be when the blade natural frequency and fluid frequency are coincident. The results showed that this is a bad assumption.

An alternate approach, the enforced motion method, is also presented. Similar to a linear flutter analysis, the particular points on the design map to run the analysis must be chosen based on previous NSV experience. In this case, enforced blade motion is used to promote lock-in of the blade frequency to the fluid natural frequency at a specified critical amplitude. The nonlinear HB technique is applied for a specific mode shape at a chosen amplitude and frequency for a range of interblade phase angles (IBPAs). For the IBPAs that are locked-on, the unsteady modal forces for each harmonic are determined from the calculated Fourier coefficients. The mode is acceptable if the equivalent damping is greater than zero for all IBPAs.

Typically, to avoid NSV, the blade is changed aerodynamically. Here, a method for re-design is proposed by changing the blade frequency. To re-design the blade, one can then run a range of frequencies (including the blade frequency) and a range of modal amplitudes to determine those for which the fluid frequency is locked -on to the blade frequency. Then, the equivalent aerodynamic damping is calculated at the locked-in frequencies. A positive damping indicates that the blade is stable at that frequency so NSV will not occur. Similarly, a negative damping indicates that the system is unstable and NSV will occur. The LCO amplitude is then determined as the amplitude for which the damping goes from positive to negative. It is assumed that outside of the lock-in region is an off-resonant condition and therefore, low amplitude. Although the method will not directly calculate the NSV frequency and amplitude,

it will provide bounds on the NSV frequency and determine whether or not the LCO amplitude is less than or greater than a critical amplitude. Furthermore, the method can be extended to determine the precise LCO amplitude.

Both of these methods were applied for three test cases, namely a 2-D circular cylinder, a 2-D airfoil cascade tip section of a modern compressor, and a full 3-D high pressure compressor cascade that encountered NSV in rig testing. All of the computations were performed using a novel harmonic balance technique for nonlinear, unsteady flows. The harmonic balance technique has the ability to model large flow disturbances and strong linearities found in turbomachinery and takes one to two orders of magnitude less computational time than traditional time marching techniques. Based on the results, a final design method is proposed to industry.

8.1 Comparison of LCO Amplitudes for All Cases

In order to understand the overall behavior, a comparison between the three test cases was investigated. Figure 8.1 shows the LCO amplitudes for each frequency within the lock-in region, normalized by the maximum amplitude achieved for the circular cylinder, the 2-D airfoil cascade, and the full 3-D compressor cascade. For all cases, the maximum blade response is not at the natural shedding frequency as is assumed by the traditional "forced response" design approach. This has significant implications for NSV design analysis because it demonstrates the need to include blade motion.

8.2 Recommendations and Future Work

Therefore, an efficient, adaptable design method to screen for NSV has been developed and is recommended for industry use. It's advantages over existing design

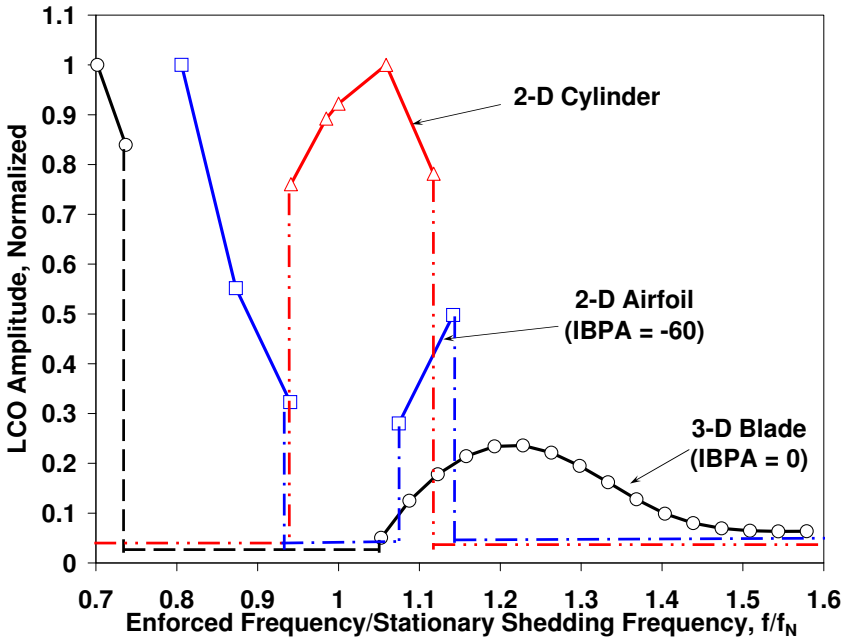

Figure 8.1: LCO amplitude as a function of the enforced frequency non-dimensionalized by the stationary shedding frequency for a particular aerodynamic condition, such as IBPA or Reynolds number for comparison.

approaches include:

- Use of a nonlinear frequency domain harmonic balance (HB) method which requires 1 - 2 magnitudes less computational time than traditional time-marching computational fluid dynamics (CFD) methods
- Inclusion of blade motion to capture most significant blade response by exploiting the lock-in phenomenon for a specific mode at a finite, critical amplitude
- Ease of implementation of proposed method into traditional design practice since a linear flutter analysis is already conducted at infinitesimal amplitude

All of the circular cylinder studies were conducted for flow in the laminar region. This analysis could be extended to consider flow at much higher Reynolds numbers, well into the turbulent regime. Another test case could include the simulation of a

tandem cylinder array. Tanida, et al. provides experimental data for the mean drag and fluctuating lift forces for two stationary cylinders in a tandem arrangement at Re = 80 [43]. In addition, they looked at the case where the downstream cylinder was oscillating transversely. This could also be an interesting case to model.

In addition, it would be beneficial to look for other 2-D cascade test cases with existing solutions and experimental data to compare with those results. In particular, a separated flow case and a shock-induced case would be of academic interest.

There are also plans to investigate other 3-D engine configurations that experienced NSV in rig testing. Since the instability under consideration in this study was primarily a coupled, suction side vortex unsteadiness and tip flow instability, it is advantageous to investigate other aerodynamic instability features such as rotating stall and acoustic instabilities. This will indicate the enforced motion design method's ability to handle all types of flow instabilities and blade geometries.

Finally, a tip clearance modeling study will be performed. Although the results did not agree well with the experimental data for the 3-D case (2850 Hz vs. 2600 Hz), it is hypothesized that this is due to the tip clearance modeling and not a limitation of the enforced motion method itself. This demonstrates that existing CFD methods are not currently good enough. Therefore, there is a strong need for further CFD improvement to achieve better agreement with test data.

The conducted research demonstrates that blade motion is required for NSV design. Ultimately, the authors hope that this enforced motion method will be integrated into industry design analysis and become an efficient preliminary design tool for NSV.

Bibliography

[1] K. C. Hall, J. P. Thomas, M. A. Spiker, and R. E. Kielb. Prediction of non-synchronous vibration using a harmonic balance technique. In *9th National Turbine Engine High Cycle Fatigue (HCF) Conference*, 2004.

[2] Robert E. Kielb, Kenneth C. Hall, Meredith A. Spiker, and Jeffrey P. Thomas. Non-synchronous vibration of turbomachinery airfoils. In *AFOSR Final Report*, 2006.

[3] R. Kielb, J. Barter, J. Thomas, and K. C. Hall. Blade excitation by aerodynamic instabilities - a compressor blade study. In *ASME Turbo Expo*, 2003.

[4] M. A. Spiker, R. E. Kielb, K. C. Hall, and J. P. Thomas. Efficient design method for non-synchronous vibrations using enforced motion. In *ASME Turbo Expo*, 2008.

[5] K. C. Hall, J. P. Thomas, and W. S. Clark. Computation of unsteady nonlinear flows in cascades using a harmonic balance technique. In *9th International Symposium on Unsteady Aerodynamics, Aeroacoustics and Aeroelasticity of Turbomachines (ISUAAAT)*, 2000.

[6] L. E. Snyder and D. W. Burns. Forced vibration and flutter design methodology. In *AGARD Manual on Aeroelasticity in Axial-Flow Turbomachines*, volume 2, chapter 22, pages 1–28. 1988.

[7] R. Mailach. Experimental investigation of rotating instabilities in a low speed research compressor. In *Third European conference on Turbomachinery - Fluid Dynamics and Thermodynamics*, 1999.

[8] R. Mailach, I. Lehmann, and K. Vogeler. Rotating instabilities in an axial compressor originating from the fluctuating blade tip vortex. In *ASME Turbo Expo*, 2000.

[9] R. Mailach, H. Sauer, and K. Vogeler. The periodical interaction of the tip clearance flow in the blade rows of axial compressors. In *ASME Turbo Expo*, 2001.

[10] J. Marz, X. Gui, and W. Neise. On the structure of rotating instabilities in axial flow machines. In *14th International Symposium on Airbreathing Engines*, 1999.

[11] J. Marz, C. Hah, and W. Neise. An experimental and numerical investigation into the mechanisms of rotating instability. In *ASME Turbo Expo*, 2001.

[12] M. Inoue, M. Kuroumaru, T. Tanino, and M. Furukawa. Propagation of multiple short length-scale stall cells in an axial compressor rotor. In *ASME Turbo Expo*, 1999.

[13] G. Lenglin and C. S. Tan. Characterization of wake- and tip-vortex induced unsteady blade response in multistage compressor environment. In *7th National Turbine Engine HCF Conference*, 2001.

[14] H. D. Vo. Role of tip clearance flow in the generation of non-synchronous vibrations. In *44th AIAA Aerospace Sciences Meeting and Exhibit*, Reno, NV, 2006.

[15] J. Thomassin and H. D. Vo. Blade tip clearance flow and compressor nsv: The jet core feedback theory as the coupling mechanism. In *ASME Turbo Expo*, 2007.

[16] A. J. Sanders. Nonsynchronous vibration (nsv) due to a flow-induced aerodynamic instability in a composite fan stator. *Journal of Turbomachinery*, 127:412–421, April 2005.

[17] T. R. Camp. A study of acoustic resonance in a low-speed multistage compressor. *Journal of Turbomachinery*, 121:36–43, 1999.

[18] J. P. Chen and W. R. Briley. A parallel flow solver for unsteady multiple blade row turbomachinery simulations. In *ASME Turbo Expo*, 2001.

[19] K. C. Hall, J. P. Thomas, and W. S. Clark. Computation of unsteady nonlinear flows in cascades using a harmonic balance technique. *AIAA Journal*, 40(5):879–886, 2002.

[20] J. P. Thomas, E. H. Dowell, and K. C. Hall. Nonlinear inviscid aerodynamic effects on transonic divergence, flutter, and limit cycle oscillations. *AIAA Journal*, 40(4):638–646, 2002.

[21] M. McMullen, A. Jameson, and J. Alonso. Application of a non-linear frequency domain solver to the euler and navier-stokes equations. In *40th AIAA Aerospace Sciences Meeting and Exhibit*, 2002.

[22] K. Ekici and K. C. Hall. Nonlinear frequency-domain analysis of unsteady flows in turbomachinery with multiple excitation frequencies. In *24th AIAA Applied*

Aerodynamics Conference, 2006.

[23] J.M. Verdon and J.R. Caspar. Subsonic flow past an oscillating cascade with finite mean flow deflection. *AIAA Journal*, 18, 1980.

[24] J.M. Verdon and J.R. Caspar. Development of a linear unsteady aerodynamic analysis for finite-deflection subsonic cacades. *AIAA Journal*, 20, 1982.

[25] Joseph M. Verdon and Joseph R. Caspar. A linearized unsteady aerodynamic analysis for transonic cascades. *Journal of Fluid Mechanics*, 149:403–429, 1984.

[26] K. C. Hall and E. F. Crawley. Calculation of unsteady flows in turbomachinery using the linearized euler equations. *AIAA Journal*, 27:777–787, 1989.

[27] Kenneth C. Hall and William S. Clark. Linearized euler predictions of unsteady aerodynamic loads in cascades. *AIAA Journal*, 31:540–550, 1993.

[28] W. Clark and K. C. Hall. A time-linearized navier-stokes analysis of stall flutter. *Journal of Turbomachinery*, 122:467–476, 2000.

[29] W. Ning and L. He. Computation of unsteady flows around oscillating blades using linear and nonlinear harmonic euler methods. *Journal of Turbomachinery*, 120:508–514.

[30] L. He and W. Ning. Efficient approach for analysis of unsteady viscous flows in turbomachines. *AIAA Journal*, 17:2005–2012.

[31] M. McMullen, A. Jameson, and J. Alonso. Acceleration of convergence to a periodic steady state in turbomachinery flows. In *39th AIAA Aerospace Sciences Meeting and Exhibit*, 2001.

[32] R. L. Davis, R. H. Ni, and J. E. Carter. Cascade viscous flow analysis using the navier-stokes equations. *Journal of Propulsion*, 3:406–414, 1987.

[33] Ron-Ho Ni. A multiple-grid scheme for solving the euler equations. *AIAA Journal*, 20:1565–1571, 1992.

[34] Raymond C. Maple. *Adaptive harmonic balance method for unsteady, nonlinear, one-dimensional periodic flows*. Phd thesis, Air Force Institute of Technology, 2002.

[35] P. Spalart and S. Allmaras. A one-equation turbulence model for aerodynamic flows. 1992.

[36] R. L. Davis, T. Shang, J. Buteau, and R. H. Ni. Prediction of three-dimensional unsteady flow in multistage turbomachinery using an implicit dual time-step approach. In *ASME, SAE, and ASEE 32nd Joint Propulsion Conference and Exhibit*, 1996.

[37] A. I. Sayma, M. Vahdati, L. Sbardella, and M. Imregun. Modeling of three-dimensional viscous compressible turbomachinery flows using unstructured hybrid grids. *AIAA Journal*, 38:945–954, 2000.

[38] Anatol Roshko. *On the development of turbulent wakes from vortex streets*. Phd thesis, California Institute of Technology, 1952.

[39] C. H. K. Williamson. Defining a universal and continuous strouhal-reynolds number relationship for the laminar vortex shedding of a circular cylinder. *Physics of Fluids*, 31(10).

[40] C. H. K. Williamson and R. Govardhan. Vortex-induced vibrations. *Annual Review of Fluid Mechanics*, 36:413–455, 2004.

[41] C. H. K. Williamson. Vortex dynamics in the cylinder wake. *Annual Review of Fluid Mechanics*, 28:447–526.

[42] T. Sarpkaya. A critical review of the intrinsic nature of vortex-induced vibrations. *Journal of Fluids and Structures*, 19:389–447, May 2004.

[43] Y. Tanida, A. Okajima, and Y. Watanabe. Stability of a circular cylinder oscillating in uniform flow or in a wake. *Journal of Fluids and Structures*, 61:769–784, 1973.

[44] C. Norberg. Flow around a circular cylinder: Aspects of fluctuating lift. *Journal of Fluids and Structures*, 15:459–469.

[45] C. Norberg. Fluctuating lift on a circular cylinder: Review and new measurements. *Journal of Fluids and Structures*, 17:57–96.

[46] Roger T. Keefe. Investigation of fluctuating forces on a cylinder in a subsonic stream, and of the associated sound field. *The Journal of the Acoustical Society of America*, 34:1711–1714, 1962.

[47] R. Henderson. Details of the drage curve near the onset of vortex shedding. *Physics of Fluids*, 7:2102–2104.

[48] G. Koopman. The vortex wakes of vibrating cylinders at low reynolds numbers. *Journal of Fluid Mechanics*, 28:501–512, 1962.

[49] Robert D. Blevins. *Flow-induced vibration*. Van Nostrand Reinhold, New York, 1990.

[50] P. Anagnostopoulos and P. W. Bearman. Response characteristics of vortex-excited cylinder at low reynolds numbers. *Journal of Fluids and Structures*, 6:39–50, 1992.

[51] P. Anagnostopoulos. *Flow-induced vibrations in engineering practice*. WIT Press, Boston, 2002.

[52] M. M. Zdravkovich. Different modes of vortex shedding: An overview. *Journal of Fluids and Structures*, 10:427–437, 1996.

[53] G. E. Karniadakis and G. S. Triantafyllou. Frequency selection and asymptotic states in laminar wakes. *Journal of Fluid Mechanics*, 199:441–469, 1989.

[54] B. S. V. Patnaik, P. A. A. Narayuna, and K. N. Seetharamu. Numerical simulation of laminar flow past a transversely vibrating circular cylinder. *Journal of Sound and Vibration*, 228:459–475, 1999.

[55] M. M. Zdravkovich. Modification of vortex shedding in the synchronization range. *Journal of Fluids Engineering*, 104:513–517, 1982.

[56] E. H. Dowell, K. C. Hall, J. P. Thomas, R. E. Kielb, M. A. Spiker, and C. M. Dengri. A new solution method for unsteady flows around oscillating bluff bodies. In *IUTAM Symposium on Fluid-Structure Interaction in Ocean Engineering*, 2007.

[57] M. A. Spiker, J. P. Thomas, R. E. Kielb, K. C. Hall, and E. H. Dowell. Modeling cylinder flow vortex shedding with enforced motion using a harmonic balance approach. In *47th AIAA/ASME/ASCE/AHS/ASC Structures, Structural Dynamics and Materials (SDM) Conference*, 2006.

[58] J. C. S. Lai and M. F. Platzer. Jet characteristics of a plunging airfoil. *AIAA Journal*, 37:1529–1537, 1999.

[59] Y. W. Jung and S. O. Park. Vortex-shedding characteristics in the wake of an oscillating airfoil at low reynolds number. *Journal of Fluids and Structures*, 20:451–464.

[60] A. B. Bauer. Vortex-shedding from thin flat plates parallel to the free stream. *Journal of the Aerospace Sciences*, 28:340–341, 1961.

[61] R. F. Huang and C. L. Lin. Vortex-shedding and shear-layer instability of wing at low-reynolds numbers. *AIAA Journal*, 33:1398–1403.

[62] Baoshan Zhu and Kyoji Kamemoto. Probability of self-oscillation induced by vortex shedding from a thin cambered blade. *Experimental Thermal and Fluid Science*, 29:129–135, 2004.

[63] Baoshan Zhu, Jun Lei, and Shuliang Cao. Numerical simulation of vortex shedding and lock-in characteristics for a thin cambered blade. *Journal of Fluids Engineering*, 129:1297–1305, 2007.

[64] J. P. Gostelow, M. F. Platzer, and W. E. Carscallen. On vortex formation in the wake flows of transonic turbine blades and oscillating airfoils. *Journal of Turbomachinery*, 128:528–535, 2006.

[65] John Young and Joseph C. S. Lai. Vortex lock-in phenomenon in the wake of a plunging airfoil. *AIAA Journal*, 45:485–490, 2007.

Biography

Meredith A. Spiker was born October 8, 1980 in Atlantic City, New Jersey, to Mary Anne and Richard Spiker. After graduating from Egg Harbor Township High School in Egg Harbor Township, New Jersey in 1999, she obtained a B.S. in mechanical engineering from the University of Virginia in 2003. She then received her M.S. from Duke University in 2005 and her thesis was entitled, Study of Cylinder Flow Vortex Shedding Using a Harmonic Balance Approach to Understand Non-synchronous Vibration in Turbine Blades. This dissertation fulfills the requirements of Ph.D. in mechanical engineering from Duke University, which she obtained in 2008 under the advisement of Dr. Robert E. Kielb. Her research interests include turbomachinery unsteady computational fluid dynamics (CFD); aeromechanics including non-synchronous vibrations (NSV), forced response, and flutter; aeroelasticity.